Numerical modelling of detached plasmas in the MAST Upgrade Super-X divertor

Omkar Myatra

PhD

University of York

Physics

April 2021

Abstract

This thesis covers some of the recent predictive modelling work carried out as part of preparations for MAST-U physics operations. The SOLPS-ITER code package has been used to numerically study the behaviour of detached plasmas in the MAST-U Super-X divertor configuration. One of the two topics addressed in this work concerns the role of the divertor magnetic geometry in the control of detached Super-X plasmas. The second topic concerns the comparison of strongly detached conditions achieved through the density ramp and extrinsic impurity radiation approaches, with a focus on the impact of ion-molecule ($D^+ - D_2$) elastic collisions on the detached Super-X divertor conditions.

The subject of detachment control has been addressed by comparing the evolution of detached divertor plasma solutions obtained from SOLPS-ITER to the predictions of an analytical model for detachment control, called herein the 'detachment location sensitivity' (DLS) model. Two sets of steady state SOLPS-ITER solutions ranging from detachment onset to strongly detached conditions are studied. One set of solutions is obtained by varying the D_2 fuelling rate and the other by varying the nitrogen (N) injection rate (or 'seeding' rate) at a fixed fuelling rate for the same (2.5MW) input power. The movement of various features of the plasma solutions (which correspond to the extent of detachment) through the divertor volume is tracked as a function of control parameters and qualitative similarities are observed between the two scans - both scans indicate that strong gradients in the magnetic field strength along the field line in the MAST-U Super-X divertor may be contributing to a reduction in the sensitivity of the detachment extent to the fuelling or seeding rate, in qualitative agreement with the predictions of the DLS model. This indicates that strong gradients in the magnetic field strength along the field line could potentially help passively stabilise the detachment extent and enhance detachment control in Super-X divertors. However, plasma-neutral pressure balance considerations indicate that tight baffling of neutrals may also be playing a role.

While the evolution of the detachment extent is qualitatively similar between the two scans, qualitative differences are observed in the comparison of strongly detached divertor conditions. Significant plasma recombination near the divertor plate is observed in the D_2 fuelling case whereas it is negligible in the N seeding case. The divertor plasma density profile in the fuelling case is strongly peaked near the target, qualitatively different from that in the seeding case in which the plasma density profile is mostly flat. Lower target temperatures are also achieved in the fuelling case. Qualitative features of the seeding case are recovered in the fuelling case by turning off $D^+ - D_2$ elastic collisions. Analysis suggests that the elastic collisions are an important divertor plasma energy and momentum sink in strongly detached conditions which enhance access to recombining conditions. Further analysis also suggests that additional momentum boundary conditions for the divertor targets may need to be included in SOLPS-ITER to study strongly detached impurity seeded scenarios, and that the set of plasma neutral-interactions included in the simulations presented here may not be sufficient to accurately model MAST-U Super-X impurity seeding discharges.

Contents

List of Tables

List of Figures

Acknowledgements

The work presented in this thesis has been possible because of the guidance, patience and support of a lot of people. I owe my deepest gratitude to them.

First and foremost, I would like to express my sincere thanks to my supervisors David Moulton, Bruce Lipschultz and Ben Dudson, who offered help and continuous support ever since the project started. I am utmost grateful to David for his patience and for entertaining my constant nagging and questions about SOLPS. Despite his many other commitments, he provided me with excellent guidance, insightful comments and motivated me in every step of the project. Whenever I felt unproductive, I would seek him out just for a general chat about divertor physics - so approachable. I would like to thank Bruce for his patience with me in general. His criticism forced me to make sure all possible details were closely examined, and allowed me to see that sometimes, interesting physics can be hiding behind minor details. His vast experience helped place this work in a wider context. I would also like to thank him for the time he put into reading and providing comments on our papers, and in effect helping me significantly improve my scientific writing skills. Ben is one of the nicest and smartest people I have ever met. He was easily able provide a direction during moments when it was difficult to come up with ideas. His comments always carried a lot weight and convincing him about anything always made me a whole lot more confident about my understanding of the thing. I would like to extend my gratitude to Kevin Verhaegh, Sarah Newton and Alex Fil, they were always enthusiastic about the work presented in this thesis and available to provide their perspective which made an important contribution to this work.

I thank all my friends for all the laughs and the bants, and the moral support. Thanks my bhai logs, Vish, Kafi, Vignesh and Arka for the suttas, nights out, epic adventures and sometimes accommodation. Thanks Tom for being one of the most chilled housemates and for the endless chats about SOL physics, xarray, climate change, Warhammer 40k projects, xarray and xarray. Huge thanks to Andrew J, Jack, Bhavin, Fabio, Simon, Lena, Charlie, Hasan, Siobhan, Sam G, Sam W, Michail, Rich, Peter and Matt for helping me hold on to my sanity on a daily basis. Special shout out to Daljeet, we connected on the widest range of topics, from Indian geopolitics to divertor impurity transport to Bloodywood. Thank you attendees and organisers of the annual

winter gathering in a big house with a hot tub for some of the best weekends. Mehar, Dhruv, Vidhi, Ruchi and Angie, you all are just special, thank you. Thanks my neighbours Rich and Jess, and little Lydia and Tara, for being the most welcome distraction during covid times. Victoria, you could learn from them.

Finally, and most importantly, I would like to thank my family, who regardless of the distance, and other things, were always encouraging and supporting me with their best wishes, memes, instagram reels, whatsapp forwards and regular video chats. Thank you for everything.

Declaration

I declare that: this thesis is a presentation of original work; I am the sole author; this work has not previously been presented for an award at this or any other university; all sources are acknowledged as references.

Parts of this thesis have been adapted from the following papers:

- O. Myatra et al. "The role of divertor magnetic geometry in detachment control in the MAST-U Super-X configuration" (soon to be submitted)
- O. Myatra et al. "Impact of ion-molecule elastic collisions on strongly detached MAST-U Super-X divertor conditions according to SOLPS-ITER" (soon to be submitted)

The work done during this project has either directly or indirectly contributed to the following papers:

- A Fil et al 2020 "Separating the roles of magnetic topology and neutral trapping in modifying the detachment threshold for TCV" Plasma Physics and Controlled Fusion **62** 035008
- C Bowman et al 2020 "Development and simulation of multi-diagnostic Bayesian analysis for 2D inference of divertor plasma characteristics" Plasma Physics and Controlled Fusion **62** 045014
- S F Smith et al 2020 "Simulations of edge localised mode instabilities in MAST-U Super-X tokamak plasmas" Nuclear Fusion **60** 066021
- K Verhaegh et al 2021 "A novel hydrogenic spectroscopic technique for inferring the role of plasma-molecule interaction on power and particle balance during detached conditions" Plasma Physis and Controlled Fusion **63** 035018
- K Verhaegh et al 2021 "A study of the influence of plasma-molecule interactions on particle balance during detachment" Nuclear Materials and Energy **26** 100922

Chapter 1

Introduction

1.1 Fusion Energy

Fusion, the process by which two light nuclei join together via a highly exothermic nuclear reaction, is seen as a candidate to generate clean power and a potential replacement for fossil fuels. Currently, the majority of the fusion community is aiming to create and sustain an environment that would encourage the following nuclear reaction:

$$ {}^{2}_{1}\mathrm{D} + {}^{3}_{1}\mathrm{T} \rightarrow {}^{4}_{2}\mathrm{He} + {}^{1}_{0}\mathrm{n} \tag{1.1} $$

which is believed to be the easiest thermonuclear fusion reaction to achieve [1]. A deuterium nucleus and a tritium nucleus fuse to give a 3.5 MeV α-particle and a 14.1 MeV neutron.

In a thermonuclear environment, the D-T fuel is in a plasma state. The basic idea is that the fusion born α's heat the rest of the fuel to sustain a thermonuclear environment, and the high energy neutrons fly through the plasma to be captured in (and to heat) a blanket. The blanket is connected to a heat exchanger to generate electricity as in conventional power plants.

A large amount of research has been focussed on two approaches - inertial confinement fusion (ICF) and magnetic confinement fusion (MCF). ICF involves using high power lasers to compress a pellet filled with D-T fuel to an extremely high density and using inertia to confine the fuel long enough for a thermonuclear burn wave to propagate through the compressed plasma [2]. The key idea behind MCF is to create a magnetic configuration that can confine the plasma while it is heated to extremely high temperatures. The most widely studied MCF device, and also the subject of this study, is the tokamak [3].

The time taken for the energy contained in a plasma to leak out is characterised by the 'energy confinement time' of the plasma, τ_E, defined as the total energy stored in the plasma divided by the rate at which energy is lost. It is the average time taken for energy to escape the plasma. The

energy confinement time is an ingredient in what is known as the Lawson criterion, which defines the conditions needed for a fusion reactor to reach 'ignition' [4]. The plasma is said to be 'ignited' when the energy from the fusion products is sufficient to maintain the required thermonuclear environment against all losses and without external power input [5].

The most important figure of merit for a tokamak reactor is the 'triple product', which is closely related to the Lawson criterion. It is the product of the plasma density n, temperature T and the energy confinement time. A commercial tokamak reactor operating a D-T plasma will need to achieve a minimum triple product [3]:

$$n\tau_E T \geq 3 \times 10^{21} \text{ m}^{-3}\text{s keV} \tag{1.2}$$

The world's largest tokamak is the Joint European Torus (JET), which has reached a triple product $> 10^{21}$ m^{-3}s keV [6]. JET will be succeeded as the world's largest tokamak by ITER (formerly known as the International Thermonuclear Experimental Reactor) which is currently under construction in Cadarche, France. It is expected to be the first tokamak to ever achieve this minimum triple product.

The D-T fusion reaction rate peaks at an optimum temperature [1] and in tokamaks, operation limits in density [7] have been identified. The goal of tokamak research has therefore been, in principle, to maximise τ_E.

1.2 The tokamak

Tokamaks are doughnut shaped devices that create a magnetic configuration that has two essential components: a toroidal field and a poloidal field. The toroidal field is produced by current carrying coils wound around the torus and the poloidal field is primarily generated by toroidal currents flowing within the plasma. The result is a helical magnetic field wound around the torus, illustrated in figure 1.

The size of a tokamak is specified by its major radius, R (the distance from the centre of the torus to the centre of the plasma), and its minor radius a (the distance from the centre of the plasma to the vessel wall). On JET, $R \approx 3$ m and $a \approx 1.2$ m, while on ITER $R \approx 6.2$ m and $a \approx 2$ m. Tokamaks can be broadly categorised into 'conventional' tokamaks and 'spherical' tokamaks based on their aspect ratio, A, which is the ratio of the major radius to the minor radius. Conventional tokamaks typically have an aspect ratio $A \gtrsim 2.5$ whereas spherical tokamaks usually have an aspect ratio $A \lesssim 2$. Spherical tokamaks have demonstrated improved plasma stability and energy confinement compared to conventional tokamaks [8–14], which gives them the potential to offer a route to smaller and cheaper fusion power plants [15–18].

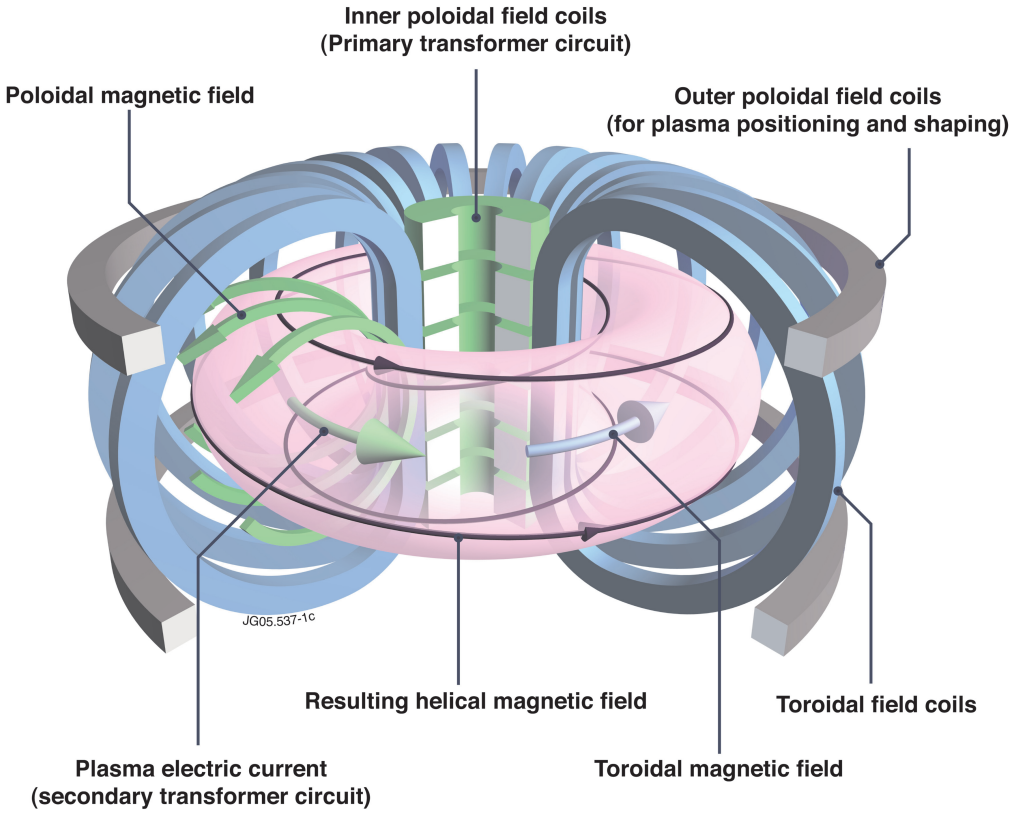

Figure 1: Schematic of the key components of a tokamak [19].

The magnetic field lines in a tokamak lie on a set of nested toroidal magnetic surfaces or 'flux surfaces'. These are surfaces which enclose a volume through which the poloidal magnetic flux is constant. Most modern tokamaks operate in what is known as the 'divertor configuration', which is created using an external conductor carrying a current in the same direction as the toroidal plasma current. A schematic of the divertor configuration is shown in figure 2. In this configuration, an X-point exists where the poloidal field is zero. The flux surface that passes through the X-point is called the separatrix, which separates the 'closed' and 'open' flux surfaces. It is also the last closed flux surface (LCFS), and it has legs called 'divertor legs'. All the open flux surfaces, along with the separatrix, are cut by solid surfaces called the divertor targets. The points on the divertor plates that are in contact with the separatrix are called the strike points. The plasma that is in the set of open flux surfaces is called the Scrape-off layer (SOL). In the region below the X-point, the separatrix separates the SOL plasma and the plasma in the 'private flux region' (PFR). The transport of heat and particles *along* the field lines is orders of magnitude faster than that *across* the field lines or flux surfaces. Thus, most of the plasma and the associated energy leaving the separatrix is quickly transported through the SOL to the divertor targets; and some of it is transported across the open surfaces through SOL turbulence and deposited onto the main chamber walls. The SOL is therefore the interface between the 'core' plasma and the internal solid surfaces of the tokamak.

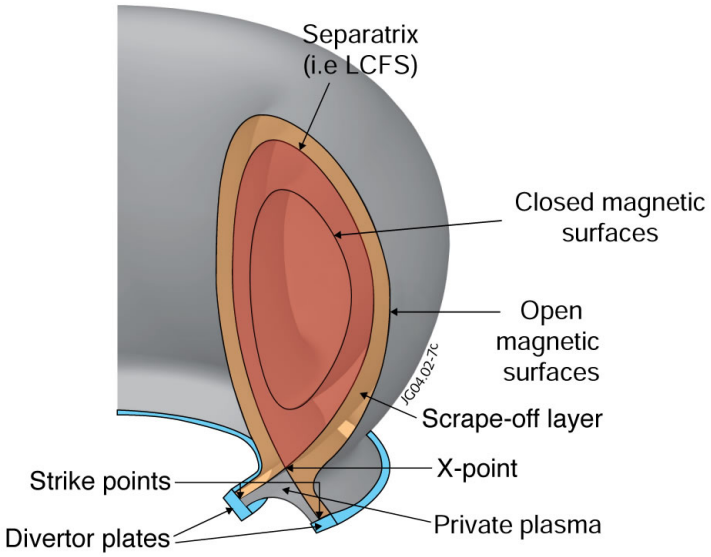

Figure 2: The poloidal divertor configuration [19].

τ_E is known to be limited by turbulence driven transport of energy across the closed flux surfaces in the core [20–22]. Two key modes of operation have been identified in tokamaks, the low-confinement mode (L-mode) and the high-confinement mode (H-mode) [23]. In H-mode, τ_E has been found to increase significantly through strong suppression of turbulence in the edge plasma [24, 25]. ITER (and probably future devices) will operate in H-mode to maximise the triple product.

1.3 The exhaust problem

Tokamaks are open thermodynamic systems. In a steady state situation, all the power generated through fusion reactions in the core that is used to maintain fusion conditions (i.e. the power from fusion born α's) will at some point cross the separatrix into the SOL, to be deposited onto the internal surface of the device. The more fusion energy a reactor produces, which is desirable, the larger the power flux that will need to be exhausted onto solid surfaces. It is obvious that solid surfaces will be able to receive only a finite amount of power before being damaged. The current technological feasibility for handling steady state heat loads is around 10 MW m^{-2} and around 20 MW m^{-2} of transient heat loads (of order a few seconds) for actively cooled surfaces [26, 27].

As mentioned earlier, most of the power entering the SOL is deposited onto the divertor plates. Further, the deposition across the divertor plates is not uniform and it tends to be strongly peaked near the strike points. The profile of the heat flux density incident across the divertor plates is correlated with the SOL plasma characteristics at the outboard midplane [28]. The plasma density, temperature and heat flux along the magnetic field gradually decay as we go from

the separatrix to further out in the SOL. Outboard midplane profiles of these quantities can be associated with a typical scale or decay length. A decay length, λ_f, of some quantity $f(r)$ is defined as $\lambda_f = f(r)/(df(r)/dr)$, where r is a coordinate that is perpendicular to the separatrix at the outboard midplane and increases as we go out into the SOL. The quantity of paramount importance is the *heat flux decay length*, λ_q, as it defines the region in the divertor over which most of the plasma energy is deposited [28].

Empirical studies have shown that λ_q in H-mode plasmas, surprisingly, is independent of machine size and only weakly depends on the power crossing the separatrix; and that it depends primarily on the poloidal magnetic field at the outboard midplane, reducing approximately linearly for increasing poloidal field magnitude [28–30]. Based on these studies, λ_q for ITER in H-mode operation is expected to be $\sim$1 mm. With about a 100 MW expected to flow from the core into the narrow SOL, this could result in up to $\sim$ 5 GW m^{-2} being transported along the field lines to the targets [31]. Geometry can be used to spread the power over a larger area; in ITER the magnetic field will meet the target at an angle $\alpha \sim 4^\circ$ to reduce the power flux incident on the target by a factor $\sin\alpha \sim 0.07$ [26, 32]. This is a significant reduction, but still about $\times$35 higher than the physical limit.

In devices beyond ITER, e.g. a demonstration power plant (DEMO), the power entering the SOL which will have to be exhausted will be significantly higher than 100MW [33, 34]. Finding an exhaust solution that is compatible with high core perfomance for economic energy production is therefore vital.

1.4 Divertor plasma detachment and MAST Upgrade

A phenomenon called 'divertor plasma detachment' has been shown to give large reductions in the plasma energy and particle flux reaching the target, and is seen as a potential solution to the exhaust problem [35–43]. A key feature of detachment is the drop in plasma pressure near the target through ion-neutral interactions [43–45]. In most tokamaks, this pressure loss typically occurs when the plasma temperature at the target is $\sim$ 5eV [36, 44], which is also the temperature at which ion-neutral interactions start playing an important role in the plasma dynamics for typical divertor densities [46].

In current experimental tokamaks, one of the approaches to access detachment is through so called 'density ramp' discharges [47–49]. In these discharges, the outboard midplane density is increased as a function of time, which lowers the plasma temperature near the divertor [50] and provides access to detachment. Erosion of plasma facing components through plasma-surface interactions typically results in the presence of 'intrinsic' impurities [39, 50, 51]. These impurities

further cool the plasma through radiative heat dissipation, aiding access to detachment. Another common approach to access detachment in current devices is introducing 'extrinsic' radiative impurities (e.g nitrogen, noble gases) in the divertor to cool the plasma, which can provide access to detachment at lower outboard midplane densities [48, 49, 52, 53]. In future high power devices, the density required to access detachment without impurities may be higher than operation limits in density [7, 54]. In devices like ITER and DEMO, radiative power dissipation through extrinsic impurities will be required to access detachment [38, 40].

Detached divertor operation in future high power devices is expected to be difficult due to a number of competing goals. Divertor power dissipation is optimised when operating at high outboard midplane densities and/or high divertor/SOL impurity levels. On the other hand, core performance and energy confinement in H-mode are optimised when operating at relatively low outboard midplane densities [55]. Further, intrinsic and extrinsic impurities can leak out of the divertor and enter the core [56–59]. While the impact of impurities on core energy confinement is rather complex - with improved confinement, degraded confinement, as well as no significant impact on confinement reported in a number of studies [38, 53, 60–69] - it is desirable, especially for future high power devices, to minimise the impurity levels in the core as this results in the dilution of the fusion fuel which lowers the core performance [41, 70]. Access to detachment at lower outboard midplane densities and SOL impurity levels, and better control of the detached plasma can help make detached divertor operation more compatible with high core performance [41].

Most current tokamaks operate in what is known as the 'conventional' divertor configuration. Although figure 2 is a general schematic/cartoon of the divertor configuration, it very closely resembles the conventional divertor configuration. The total magnetic field strength is roughly inversely proportional to the major radius. A number of theoretical and numerical studies predict that the detached regime can be accessed at lower impurity levels and outboard midplane densities by pulling the strike point away from the centre of the torus to large major radius where the total magnetic field strength is lower [71–78]. Further, a wider detached operation window is predicted for configurations which maximise 'total magnetic flux expansion' [76], which is the ratio of the total magnetic strength at the X-point to that near the strike point. It can be noted however that this is not always observed in experiments [79]; poor trapping of divertor neutrals and the strike point angle can negate the total flux expansion effect in practice [80].

In conventional divertor configurations, total flux expansion is not significantly higher than unity. An advanced divertor configuration known as the 'Super-X' [71] aims to maximise the total magnetic flux expansion. The upgraded Mega Ampere Spherical Tokamak (MAST-U) has been designed to optimize the Super-X configuration [75, 81, 82]. The MAST-U Super-X divertor

features the largest total flux expansion in existing tokamaks (×2.5-3 higher). Additionally, it offers a large amount of control over the magnetic topology in the divertor volume in order to test a wide range of divertor configurations, enabling comparisons of the Super-X to conventional as well as other advanced divertor configurations in the same tokamak. It also features tight baffling to maximise divertor neutral trapping. Examples of divertor configurations possible in MAST-U, including the conventional and Super-X, are shown in figure 3. MAST-U thus provides a test bed to study detachment physics including detachment control and threshold [83].

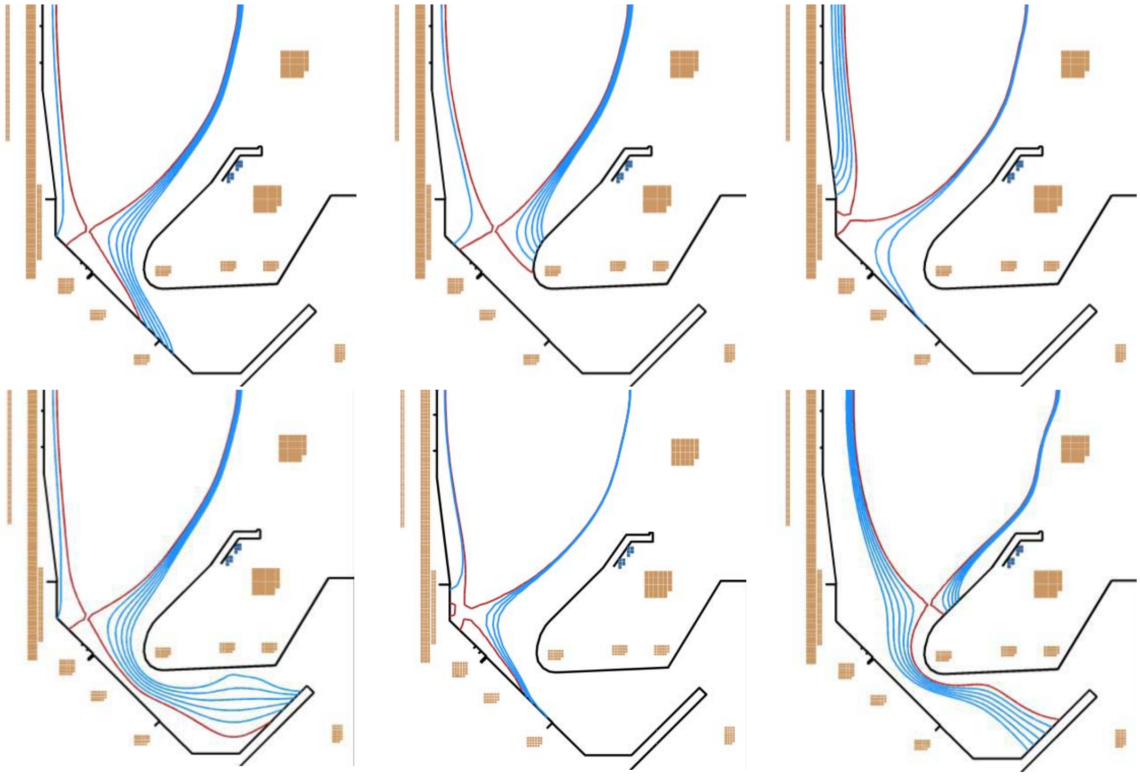

Figure 3: Top row left to right: conventional horizontal target, conventional vertical target, X-divertor. Bottow row left to right: Super-X, snowflake, inner leg Super-X [83].

1.5 Overview of thesis

One of the main aims of MAST-U is to assess the viability of the Super-X divertor as an exhaust solution for future high power tokamaks. In addition to providing access to divertor detachment at lower outboard midplane densities and SOL/divertor impurity levels, it is expected that this divertor magnetic geometry can potentially widen the window of detached divertor operation and enhance detachment control [76], making detached divertor operation more compatible with high core performance. The first part of the work presented in this thesis focuses on studying the features of the MAST-U Super-X geometry that help improve detachment control. The SOLPS-ITER code package [84, 85] has been used in concert with an analytic model for detachment control, the

detachment location sensitivity (DLS) model [76], to study the behaviour detached plasmas in the MAST-U Super-X divertor configuration. While future high power devices will require extrinsic impurity radiation to access detachment, this can be done via both extrinsic impurities or density ramps in MAST-U. In the second part of the work presented in this thesis, SOLPS-ITER is used to study strongly detached conditions achieved through the density ramp and extrinsic impurity radiation approaches, with a focus on the impact of ion-molecule ($D^+ - D_2$) elastic collisions on the detached Super-X divertor conditions.

In chapter 2, the basic SOL and divertor detachment physics relevant to this work is introduced and some issues associated with detached divertor operations in future high power devices are reviewed; followed by a brief description of the DLS model and a review of previous MAST-U SOLPS-ITER work. The specific aims of this study and the methodology are summarised in chapter 3, along with a brief description of the SOLPS-ITER code package and the simulation setup. The key observations are summarised in chapter 4. The role of the divertor magnetic geometry in detachment control is the subject of chapter 5 and differences in the strongly detached solutions are studied in chapter 6. Conclusions and future work are summarised in chapter 7.

Chapter 2

Scrape-off layer and divertor physics

The heating and erosion of edge structural components is governed by the power and particle flows reaching the solid surfaces, which enter the SOL from the main plasma and exit from it to the divertor targets [39, 50]. The SOL constitutes the interface between the astronomically hot fusion-producing plasma and the ordinary solid-matter world of the tokamak's solid structure. It is therefore essential to understand how this interface functions and how it responds to the interactions with these two very different states of matter (plasma-surface interactions, PSIs). Particle and power flows reaching the solid surfaces are related to the basic properties of the SOL plasma: the density and temperature. Knowing how important parameters like density and temperature vary spatially in the SOL, and understanding their connection to particle, momentum and power fluxes into and out of the SOL is a requirement.

This chapter covers the basic SOL and detachment physics relevant to the work presented in this thesis. Key features associated with plasma-surface interactions, and the density and temperature dependence of heat transport along the SOL are discussed first. This is followed by a brief review of a simple analytic model of the SOL called the '2-point' model, which provides some basic intuition for SOL behaviour preceding detachment. Key features of divertor detachment are discussed next, followed by a discussion of some of the issues relevant to detached divertor operation in high power devices. Finally, the DLS model and previous numerical modelling of MAST-U are reviewed at the end of this chapter.

2.1 Key concepts

2.1.1 Plasma-surface interactions

Recycling When electrons strike a solid surface, they are either backscattered/reflected or retained on the surface. The fraction of electrons reflected from a carbon surface is less than 0.1 over the electron temperature range $0.1 - 10$ keV [86]. Electrons incident on the surface can also

result in the emission of secondary electrons; however the energy of the secondary electrons is typically significantly lower than that of the incident electron [86] - for small contact angles between the magnetic field and the surface (typically the case in tokamaks), the secondary electrons are assumed to return to the surface within one gyration period. Thus, the surface is normally treated as a 'sink' for the free electrons in the SOL, and electron emission from the surface is assumed to be negligible [50].

When ions strike a solid surface, they are either backscattered/reflected while retaining most of their kinetic energy, or they are implanted near the surface and are subsequently thermally desorbed back into the plasma [87]. They may also be trapped in the solid for an extended period of time or even permanently. A very large fraction of ions which are reflected or thermally desorbed pick up electrons from the surface and return to the plasma as neutrals, irrespective of the charge state of the incident ion [88]. Thus, a solid surface acts as an effective sink for the SOL ions, as it does for electrons [50].

If a surface has not already been bombarded by the plasma, all the incident ions that are not backscattered are initially retained on the surface. This retention eventually saturates over a certain ion fluence. Once this retention has saturated, all the subsequent non-backscattered ions are promptly thermally desorbed as neutrals to be re-ionised [88]. This leads to a steady-state condition, termed 'recycling', whereby ion-electron pairs are lost to the surface roughly at the same rate as neutrals emitted from the surface re-enter the plasma and get re-ionised. The plasma essentially re-fuels itself, i.e. if external fuelling is turned off and there are no other sinks (e.g pumps), the plasma density will remain (mostly) constant [50] - thus, while the surface is a plasma sink (not a mass sink), it is also very closely related to the plasma source.

The Debye sheath In the first few μs after the plasma is initiated, i.e. just after ionisation of the fill gas in the vacuum vessel and before the recycling and ionisation have become established, the electrons, due to their small mass and high mobility, rush ahead of the ions and strike the solid surfaces, charging them up negatively [50]. From that time on, an electron-repelling potential difference exists between the plasma and the surface, slowing the loss rate of the electrons - while, at the same time, increasing the ion loss rate. Electrostatic potentials on surfaces contacting plasmas are almost entirely shielded out within a short distance. This thin region in front of the surface is called the Debye sheath and is a region of net positive space charge, existing in a dynamic equilibrium [50]. The shielding is not perfect, however, and a small electric field penetrates into the plasma. This is called the pre-sheath electric field and it acts on the ions in the SOL to help move them toward the target. It has been proved that ions and electrons enter the sheath at a speed equal to or greater than the local ion sound speed [89, 90].

Sputtering Interaction between the plasma (or even neutrals) and the plasma facing components can be accompanied by erosion of the surface through sputtering [50, 51], which results in the wall material entering the plasma. When energetic ions or neutrals strike a solid surface, sufficient momentum can be transferred to an atom in the solid lattice to eject it [91–93]. Such a removal through momentum transfer is known as 'physical' sputtering. If the surface is made of a material that is chemically reactive with hydrogen, this can lead to the formation of compounds that are loosely bound to the surface and can be easily thermally desorbed. This process is known as chemical sputtering [93, 94]. Most experimental tokamaks, including MAST-U, use a carbon first wall which undergoes both physical and chemical sputtering [51, 93, 94].

2.1.2 Simple and complex SOLs

The most important distinguishing property among SOLs is the way heat entering the SOL is transported to the targets. Heat transport can take place via conduction and convection. SOLs in which heat convection is the dominant heat transport mechanism are typically said to be in the 'sheath-limited' regime, whereas when heat conduction dominates over convection, the SOL is usually said to be in the 'conduction-limited' regime [50]. Figure 4 shows a comparison of the two SOLs in the different regimes 'straightened out' for ease of interpretation. $s_{\parallel}$ is the distance along the SOL. The shaded region on the left is the target ($s_{\parallel} = 0$) and the region where the heat enters the SOL, q_{in}, is the 'upstream' region ($s_{\parallel} = L$). Γ is the particle flux due to the SOL particle source. The distance along the field line between upstream and target is known as the connection length, L.

Since convection is the dominant heat transport mechanism, the temperature in sheath-limited SOLs, also called simple SOLs, is fairly uniform along the SOL. The plasma and neutral densities are not high enough for plasma-neutral interactions to become important [50]. Cross-field transport from the core plasma provides the only energy and particle source in the SOL, as illustrated in figure 4(a) where Γ_{in} is particle flux entering the SOL from the core. In addition, the divertor targets are the only energy and particle sinks.

Complex SOLs are characterised by a significant drop in temperature near the target. In simplified models of the complex SOL (section 2.2), is it assumed that there are no energy, momentum or particle sinks along the SOL in attached conditions. Low plasma flow along the SOL is assumed, which means that the reduction in temperature along the SOL implies a consistent increase in the plasma density near the target. Thus, the plasma density tends to be relatively high near the target resulting in a very short ionisation mean free path of the recycling neutrals. Most neutrals are ionised within the SOL, and in fact very close to the target in attached conditions [50]. Further, ionisation of recycled neutrals is the dominant particle source in the SOL and is significantly

higher than the upstream particle source, as illustrated in figure 4(b) - the most of the plasma flux arriving at the target is created very close to the target.

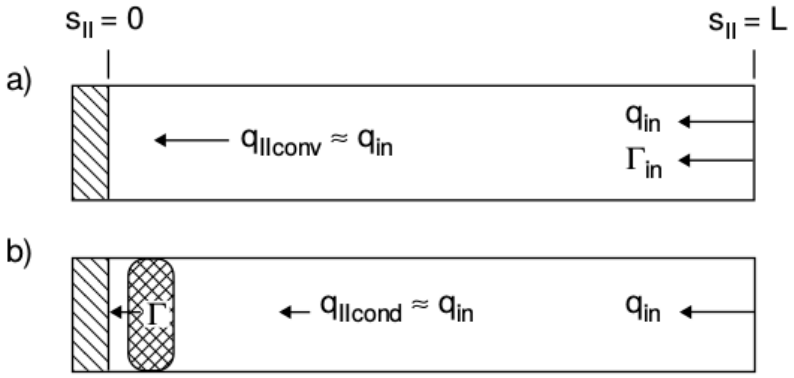

Figure 4: Schematic of (a) a sheath limited SOL and (b) a conduction limited SOL [50].

Existence of a temperature gradient depends on the SOL collisionality, $\nu^*_{\rm SOL}$, which is the ratio of the connection length (L) to the electron and ion self-collisionality lengths, $\lambda_{ee} \approx 10^{16} T_e^2/n_e$ and $\lambda_{ii} \approx 10^{16} T_i^2/n_i$ respectively [50]. A rough estimate of $\nu^*_{\rm SOL}$ can be obtained by assuming $T_e \sim T_i$ (not always true in reality) as follows [50]:

$$\nu^*_{\rm SOL} \equiv L/\lambda_{ee\ ii} \approx 10^{-16} \frac{n_u L}{T_u^2} \tag{2.1}$$

where n_u and T_u are the upstream density and temperature and $\lambda_{ee\ ii}$ is the electron/ion self-collisionality length. Analytical considerations [50] lead one to expect negligible temperature gradients for $\nu^*_{\rm SOL} \approx 10$ or lower and significant temperature gradients for $\nu^*_{\rm SOL} \approx 50$ or higher. This is picture is summarised in figure 5.

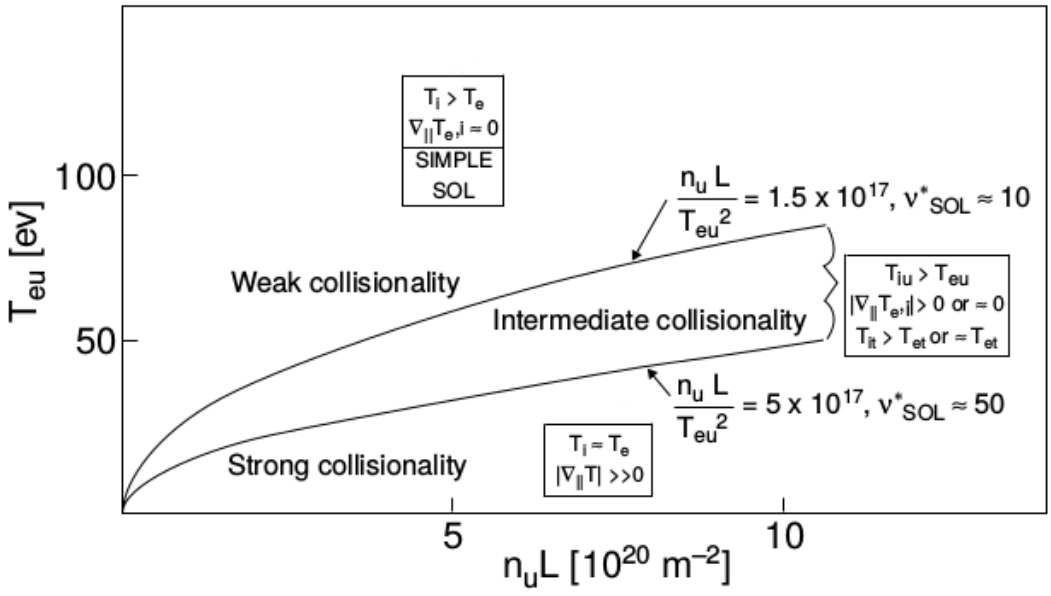

Figure 5: Different collisionality regimes based on equation 2.1 [50].

Now, low target temperature is a requirement for detachment and the required plasma performance corresponds to high upstream temperature. Hence, it is of interest to operate in the conduction-limited regime. In a tokamak discharge, the transition from the sheath-limited to the conduction limited regime can be understood as follows. One starts with a low edge plasma density and a low SOL collisionality. The energy and particles crossing the separatrix flow to the divertor along the magnetic field lines within the SOL. Arriving at the divertor targets, this plasma flux produces virtually the same (low) flux of neutrals leaving the target. Since neutrals are not magnetized, their trajectories are determined by the neutral-wall, neutral-plasma, and neutral-neutral interactions. For the low plasma flux and low plasma density in the divertor volume, the neutral density is also low. As a result, neutral dynamics in this case is largely determined by the neutral-wall interactions. The neutral density, N_d, in the divertor volume can be estimated as $N_d = \Gamma_d \tau_N / V_d$ where Γ_d is the plasma flux to the divertor targets, V_d is the divertor volume, and τ_N is the effective time of neutral escape from the divertor. For the case where τ_N is not too long, for low Γ_d, N_d is low. Therefore, the plasma flows along the magnetic field lines from upstream towards the divertor virtually freely and the ionization of the neutrals does not enhance the plasma flux to the target. This is the sheath-limited regime (also known as the 'low recycling' regime). As the edge plasma density (upstream density) increases, the SOL collisionality and the plasma flux entering the divertor also increase. The increase in SOL collisionality means that heat transport through conduction starts becoming important and a temperature gradient along the SOL starts to develop. With increasing plasma flux and the same τ_N, N_d increases. This coupled with the reducing divertor temperature, at some point the plasma-neutral interactions (ion-neutral collisions and neutral ionization by electron impact) in the divertor volume become important and, eventually, dominant ingredients in the divertor plasma dynamics. Neutral ionization in the divertor volume and the plasma sink to the divertor targets create a strong particle recirculation loop - the same particles spend a long time in the divertor, part of the time as ions and the rest as neutrals. As a result, τ_N becomes much larger than the rates of both the plasma fuelling and the neutral pumping from divertor. At the same time, the plasma flow upstream of the ionisation region becomes almost stagnated. This is the conduction limited regime (also known as the 'high-recycling' regime). In the low-recycling regime, the plasma flux to the target increases linearly with the upstream density and the transition to the high-recycling regime corresponds to a transition from the linear dependence to a quadratic dependence [50, 95]. Models used to study complex SOLs are described next.

2.2 The 2-point model

The 2-point model is the most basic analytical model for an attached, conduction limited SOL [50, 96]. It relates upstream plasma conditions to target conditions using pressure and power balance. No attempt is made to predict the temperature/density *between* these two points, hence 2-point model. The upstream point 'u' can be essentially anywhere in the SOL (although typically not below the X-point position), as shown in figure 6. The choice of the upstream location depends on what one is trying to achieve. For example, in simple analyses involving the basic 2-point model, u is usually taken to be anywhere between X-point and the outboard midplane. In more sophisticated analyses which look at the plasma energy, momentum and particle balance in the divertor, u is taken to be at the X-point. The target point 't' is (obviously) at the target.

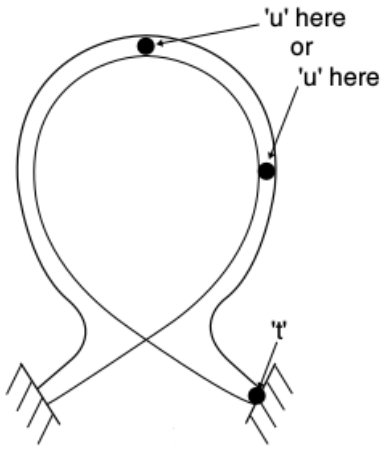

Figure 6: The 2 points 'u' (upstream) and 't' (target) in the 2-point model. 'u' can be taken to be anywhere from half-way between the targets to above the X-point [50].

The principal assumptions of the basic 2-point model are as follows. It is assumed that neutrals recycling from the targets are all ionised in a thin layer immediately in front of the target. Further, a neutral which resulted from an ion impacting the target while travelling along a particular magnetic field line is assumed to be re-ionised on that same field line, illustrated in figure 7. In steady state, the same particles recycle over and over, spending part of their time as ions and part of their time as neutrals. The only parallel plasma flow is in a very thin layer between the start of the ionisation region and the target. There is no flow throughout essentially all of the SOL, while in this very thin layer the flow velocity increases from zero - at the start of the ionisation zone - up to the sound speed (c_s) at the sheath entrance. There is no cross-field particle flow - either as neutrals or ions. The particle balance is purely one dimensional. There is no volume recombination, the target is the only particle sink [50].

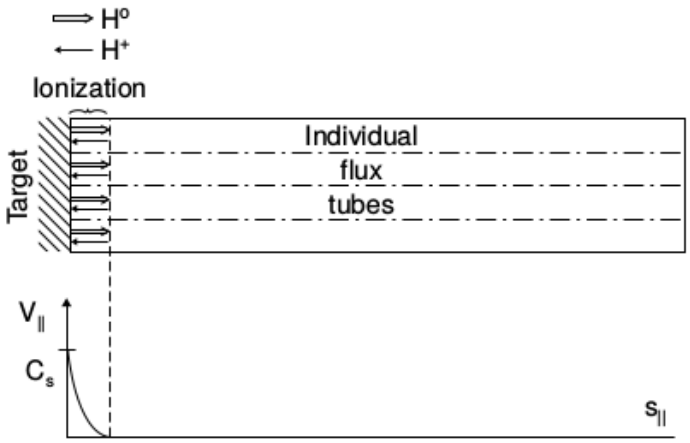

Figure 7: Simple picture of the 2-point model [50].

It is assumed that the plasma does not experience any friction or viscous effects between the thin ionization region and the target where the flow is non-zero. Thus, the total pressure throughout the entire length of the SOL is conserved. The electron temperature is assumed to be equal to the ion temperature ($T_e = T_i = T$ [eV]). Since the plasma flow velocity ($v_{||}$) is zero over almost the entire length of the SOL, parallel heat convection is absent and all the parallel power flux density, $q_{\|}$, is carried by conduction. In addition, all heat is assumed to be conducted by electrons, since the ion parallel heat conductivity, $\kappa_{0,i}(\approx 60)$, is much smaller than that for electrons, $\kappa_{0,e}(\approx 2000)$, due to their mass difference [97], so that $q_{\|} = -\kappa_{0,e}T^{5/2}(dT/ds_{\|})$ [50]. All the power enters entirely at the upstream end. Finally, it is assumed that there are no volumetric power sources or sinks in the flux tube. It can be noted that all of these assumptions are not sufficiently satisfied in reality. For example, typically $T_i > T_e$ in the SOL [50] and volumetric power loss due neutral ionisation and impurity radiation is always present. It useful to make these assumptions nonetheless, as this allows for a relatively simple model to be constructed which provides some basic intuition into the behaviour of an attached, conduction limited SOL.

The above assumptions result in [50]:

$$2n_t T_t = n_u T_u \tag{2.2}$$

$$T_u^{7/2} = T_t^{7/2} + \frac{7}{2} q_{\|} \frac{L}{\kappa_{0,e}} \tag{2.3}$$

Finally, the power deposited onto the target is given by the sheath theory [89, 90]. The ability to transmit energy through the sheath is characterized by the sheath heat transmission coefficient, γ (typically $\approx 6.5 - 7$), and the target heat flux can be expressed as

$$q_{\|} = q_t = \gamma n_t e T_t c_{st} \tag{2.4}$$

Equations 2.2, 2.3, and 2.4 (derived in [36, 50]) sum up the basic 2-point model with n_u and $q_\parallel$ as the specified control parameters and L, γ and $\kappa_{0,e}$ as the specified constants of the problem. These equations are used to obtain expressions for n_t, T_u and T_t in terms of n_u and $q_\parallel$:

$$T_u \simeq \left(\frac{7}{2}\frac{q_\parallel L}{\kappa_{0,e}}\right)^{2/7} \tag{2.5}$$

$$T_t = \frac{4q_\parallel^2 m_i}{2\gamma^2 e^3 n_u^2}\left(\frac{7}{2}\frac{q_\parallel L}{\kappa_{0e}}\right)^{-4/7} \tag{2.6}$$

$$n_t = \frac{n_u^3\gamma^2 e^3}{4m_i q_\parallel^2}\left(\frac{7}{2}\frac{q_\parallel L}{\kappa_{0e}}\right)^{6/7} \tag{2.7}$$

It should be noted that equations 2.5-2.7 are only valid when $T_t^{7/2} << T_u^{7/2}$, the reader is referred to [50] for more details. In addition, the above can be used to obtain an expression for the particle flux to the target, $\Gamma_t = n_t c_s = q_\parallel/\gamma e T_t$:

$$\Gamma_t = \frac{n_u^2\gamma e^2}{2q_\parallel m_i}\left(\frac{7}{2}\frac{q_\parallel L}{\kappa_{0e}}\right)^{4/7} \tag{2.8}$$

The basic 2-point model is a useful tool to gain some initial intuition into the SOL behaviour, for example T_t can be brought down and n_t can be increased by increasing n_u, however this increases Γ_t which is not desirable due to sputtering. Increasing L can also reduce T_t but the effect is weaker.

The basic model can be readily extended to include some important effects that have an impact on SOL parameters, i.e. power and momentum loss, and total magnetic flux expansion. The total magnetic flux expansion, f_R, is defined as:

$$f_R \equiv dA_{\parallel,t}/dA_{\parallel,u} = B_u/B_t \approx R_t/R_u \tag{2.9}$$

where $dA_\parallel$ is the elementary area normal to the total magnetic field B and R is the major radius where the major radius is a coordinate which measures the distance from the tokamak centre column, (not the major radius of the tokamak). The effect of f_R is as follows. When R and $A_\parallel$ vary along the flux tube, $q_\parallel$ is no longer constant along the flux tube since $q_\parallel \propto 1/A_\parallel$. The effect of power losses (e.g. due to radiation) along the SOL is simply lower q_t, so a power loss factor, f_{pow}, can simply be defined as the fraction of $q_{\parallel u}$ lost in the SOL. A momentum loss factor, f_{mom}, is similarly defined [50]. The combined effect on the 2-point model equations is as follows:

$$q_t = \frac{q_{\parallel u}(1 - f_{pow})}{f_R} \tag{2.10}$$

$$2n_tT_t = (1 - f_{mom})n_uT_u \tag{2.11}$$

The same procedure taken to obtain equations 2.5-2.7 can be followed to obtain expressions for target quantities (T_u is unchanged) with the effect of losses and f_R included. The result is the same expressions as in the basic 2-point model multiplied by loss factors such that [50, 73]:

$$T_t \propto \frac{(1 - f_{pow})^2}{(1 - f_{mom})^2 f_R^2} \tag{2.12}$$

$$n_t \propto \frac{(1 - f_{mom})^3 f_R^2}{(1 - f_{pow})^2} \tag{2.13}$$

$$\Gamma_t \propto \frac{(1 - f_{mom})^2 f_R}{(1 - f_{pow})} \tag{2.14}$$

Interpretation is less straight forward once the loss factors are included. For example, volumetric power loss strongly reduces T_t while, counter-intuitively, momentum loss strongly increases T_t. Usually, a large number of processes are at work in the divertor when the plasma and neutral densities are high. Each process is associated with varying degrees of heat and momentum dissipation. Whether the net result is a reduction or an increase in T_t is not immediately clear and depends on the details of the processes involved. Since the tendency for volumetric loss processes to become important strongly depends on T_t - generally increasing as T_t drops - the overall balance may be complicated. Similarly for the target density, since some volumetric processes, such as recombination, are strongly dependent on n as well as T, and since power and momentum losses influence n_t oppositely, the overall balance tends to be complex. The detailed energy, momentum and particle balance are typically the subject of detachment studies, and also a topic of this thesis. In the next section, some of the key features of divertor detachment are described.

2.3 The detached regime

As discussed earlier, the SOL transitions from the sheath limited regime to the conduction limited and high recycling regimes with increasing n_u. This is accompanied by increasing n_t and Γ_t. In the early 1980s, it was found that when the n_u is increased further, n_t saturates and starts to fall [98]. The significance of this startling n_t 'rollover' was not fully appreciated at the time, and the concept (and term) 'divertor detachment' was not invoked until the early 1990s - leading to the characterisation of a new regime, the detached regime. The detached divertor state had been observed in most tokamaks by the early 1990s [35] and it had the following key characteristics:

- Rollover of the target particle flux and target density
- Low target temperatures ($\lesssim$ 5eV) near the separatrix
- Substantial drop in pressure along the SOL

Figure 8 shows one of the earliest measurements of the target temperature (T_{ed} and T_{id}) and density (n_{ed}) as a function of the line-averaged the plasma density, $\bar{n}_e$ (which is generally correlated with the outboard midplane density) [98]. This figure encompasses all three divertor regimes. At the lowest $\bar{n}_e$, n_{ed} increases roughly linearly with $\bar{n}_e$, corresponding to the sheath-limited or low recycling regime. As $\bar{n}_e$ is increased further, the dependence of n_{ed} on $\bar{n}_e$ changes from linear to at least quadratic, indicating transition into the conduction limited or high recycling regime. As $\bar{n}_e$ is increased further still, n_{ed} saturates and then starts dropping, indicating transition into the detached regime. As with the target density, such a 'rollover' of the particle flux to the target is also typically observed - an important diagnostic marker for detachment.

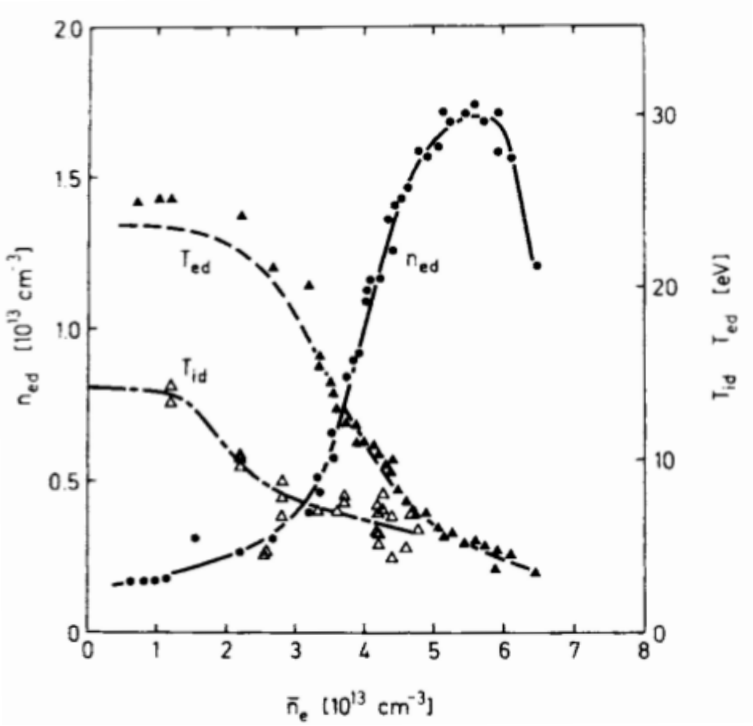

Figure 8: ASDEX, 1983 [98]. Divertor temperature (T_{id} and T_{ed}) and density (n_{ed}) measurements plotted as a function of measured line averaged main plasma density, $\bar{n}_e$(closely related to n_u).

The rollover of the particle flux to the target is accompanied by a significant reduction in plasma pressure along the SOL which typically occurs when the target plasma temperature drops below $\sim$ 5eV [44, 45, 99]. This can be seen in figure 9, in which ratio of the target plasma pressure to the upstream pressure is shown as a function of the target plasma temperature on several flux surfaces outside the separatrix for a range of Alcator C-Mod discharges from the mid 1990s [44]. There is

no significant pressure loss along the SOL while the temperature is above $\sim$ 5eV corresponding to the high-recycling regime. However as the temperature drops below $\sim$ 5eV to $\sim$ 1eV, the plasma pressure at the target drops by up to a factor $\times$100.

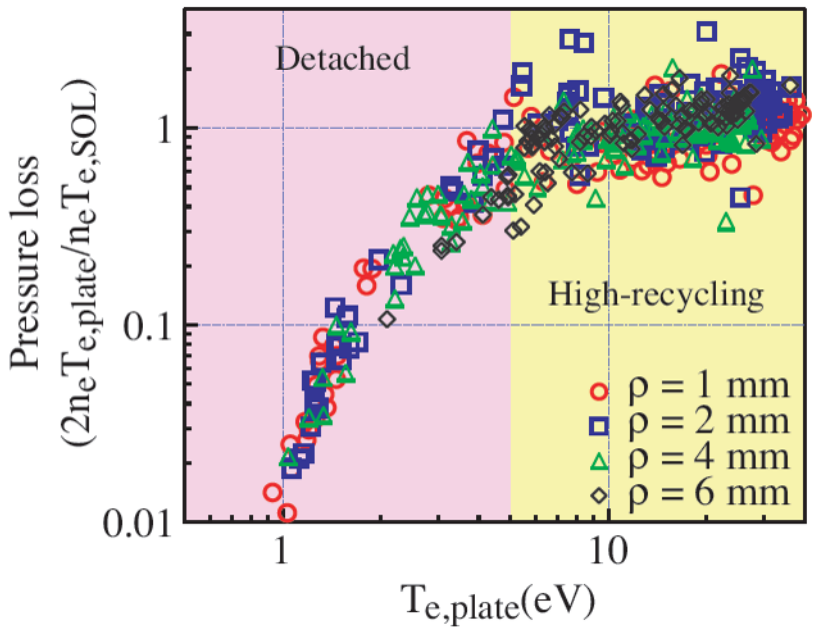

Figure 9: Ratio of the target plasma pressure to the upstream plasma pressure as a function of target plasma temperature for a range of Alcator C-Mod discharges from the 1990s [44]. Here ρ is the distance from the separatrix mapped to the outboard midplane.

Before detachment onset, the ionisation region is at the target as described in the 2-point model. Detachment is accompanied by the ionisation region moving away from the target and towards the X-point. This is primarily a result of the temperature along the SOL dropping lower and lower as one moves deeper into the detached regime. For a fixed density, as the plasma temperature drops below $\sim$10eV, the ionisation rate drops significantly. Plasma-neutral interactions like charge exchange and elastic collisions, which result in a transfer of momentum from the plasma to the neutrals, become important. As the temperature drops below $\sim$1eV, the plasma transitions from 'ionising' to 'recombining' [50]. This is illustrated in figure 10, which shows the reaction rates for ionisation, recombination and charge exchange in a deuterium plasma with different electron densities [46]. The ionisation rate is orders of magnitude higher than the recombination rate when $T_e > 10$eV and the plasma is called ionising. The neutral densities are generally low. The charge exchange rate is larger than the ionisation rate by about an order of magnitude when $T_e < 5$ eV, roughly when the plasma pressure begins to drop. Below 1eV, recombination finally dominates over ionisation. The electron density is reduced, the neutral density increased and the plasma is called recombining.

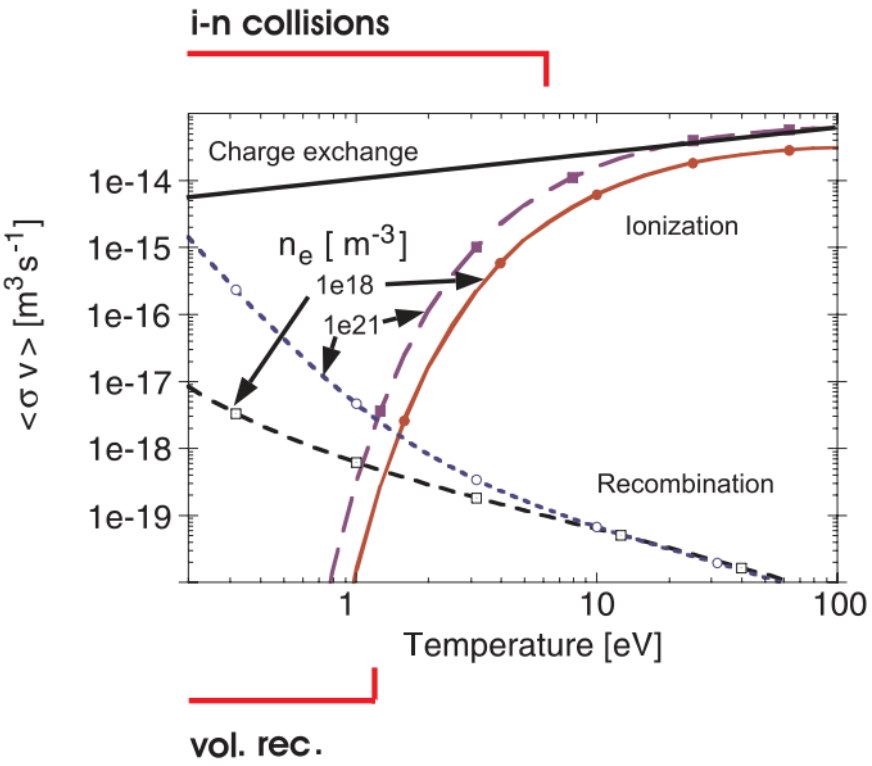

Figure 10: Rate coefficients of deuterium reactions assuming $T_e = T_i$ [46].

One can distinguish between power detachment, a reduction in heat load, and particle detachment, a reduction of Γ_t [45]. In present day devices power detachment can be achieved in the high-recycling regime due to the reduction of T_t via (impurity) radiation and ionisation energy losses. Higher P_{SOL} in ITER and DEMO implies higher recycling, hence higher n_t and Γ_t. For $T_t < 2$eV the potential energy flux on the surface due to surface recombination exceeds the thermal energy flux from the plasma incident on the target. Thus, a reduction in Γ_t or particle detachment becomes a prerequisite for power handling in high power devices like ITER and beyond [37].

The reduction in Γ_t can be understood by considering the power and particle balance in the divertor [100]. As mentioned earlier, the dominant divertor plasma source in the conduction limited regime (and beyond) is the ionisation of recycled neutrals. Once a neutral is ionised, it will either be transported back to the divertor surface or recombine within the divertor volume (it can also convert into a neutral through charge exchange but this does enter the particle balance as this also creates a corresponding ion). Here it is assumed that there is no cross-field transport, however this does not really change the basic result. Further, the particle flux entering the divertor is assumed to be negligible compared to the divertor ionisation flux. This simple particle balance gives:

$$\Gamma_{ion} = \Gamma_t + \Gamma_{rec} \tag{2.15}$$

The ionisation flux, Γ_{ion}, is the sum of the ion flux to the divertor wall and the ion flux that

recombines into neutrals before reaching the wall is Γ_{rec}. The divertor power balance is as follows. Of the power entering the divertor, Q_{div}, some of it usually lost to impurity radiation, Q_{imp}, some of it dissipated to hydrogenic excitation/ionisation, $Q_H = E_{ion}\Gamma_{ion}$ (where E_{ion} is the effective ionisation cost), and the rest reaches the wall, Q_t. Typically, during particle detachment onset (i.e. just before Γ_t starts to drop), Q_t is significantly smaller than Q_H and Q_{imp}, giving roughly the following power balance:

$$Q_{div} \approx Q_{imp} + Q_H = Q_{imp} + E_{ion}(\Gamma_t + \Gamma_{rec}) \tag{2.16}$$

Re-arranging for the particle flux to the target, we have:

$$\Gamma_t \approx \frac{Q_{div} - Q_{imp}}{E_{ion}} - \Gamma_{rec} \tag{2.17}$$

According to equation 2.17, for a given Q_{div}, a reduction in Γ_t can occur through an increase in Q_{imp}, E_{ion} and Γ_{rec}. More simply, an increase in Q_{imp} reduces the power available for ionisation of neutrals, leading to a corresponding drop in the divertor plasma source. An increase in E_{ion} means that more power is needed for each ionisation event, which translates to a reduction in the divertor plasma source for the same power available for ionisation. Γ_{rec}, obviously, takes out the ions before they make it the surface.

Finally, the reduction in Γ_t is always accompanied by a consistent drop in the plasma pressure at the target. This can be understood by recognising that Γ_t is essentially the product of the plasma density at the target and the speed at which the plasma is incident on the target, which is the local ion sound speed, c_s (section 2.1.1). So the plasma flux to the target is essentially:

$$\Gamma_t = n_t c_s = n_t \left(\frac{2eT_t}{m_i}\right)^{1/2} \propto \frac{n_t T_t}{T_t^{1/2}} \tag{2.18}$$

The product $n_t T_t$ is the plasma static pressure. According to equation 2.18, in the absence of pressure loss along the SOL (i.e. in attached conditions), Γ_t increases as T_t drops. To observe a reduction in Γ_t, a sufficient drop in the plasma pressure at the target is necessary. As mentioned earlier, the primary mechanism through which momentum is removed from the plasma is interactions like charge-exchange and elastic collisions with neutrals, which become important when $T \sim 5$eV. Hence, $T_t \lesssim 5$eV is typically observed to be a threshold for detachment.

While detached divertor operation is attractive from a power handling and exhaust perspective, it can also have undesirable effects on the core plasma performance. In the next section, some of the issues associated with detached divertor operation in power plant relevant scenarios are discussed.

2.4 Divertor detachment in a tokamak power plant

2.4.1 Heat dissipation through impurity radiation

Divertor detachment is of significant importance for practical tokamak reactor designs [33, 34, 38, 40, 101]. As mentioned previously, a target plasma temperature $T_t \sim 5$eV is required to access divertor detachment. In present day low power experimental devices, there are essentially two routes to divertor detachment. One is through 'density ramp' discharges, in which the upstream density is increased to bring T_t down to the detachment threshold; no impurities are injected although intrinsic impurities are typically present in the plasma due to erosion of plasma facing components (PFCs). The other is through 'impurity seeded' discharges, in which the upstream density is held roughly constant while impurities are added or 'seeded' in the divertor plasma with injection rate increasing with time so as to radiatively dissipate heat in the divertor and bring T_t down to the detachment threshold.

The presence of impurities basically provides access to detachment relevant temperatures at lower upstream densities. The density ramp approach for detachment studies has limited use, especially for H-modes. The maximum achievable n_u for a given P_{SOL} is set either by the H-mode density limit [54] or the Greenwald density limit [7]. At the higher heating powers relevant to a tokamak power plant, the maximum achievable n_u may not be high enough to reach sufficiently low T_t for detachment to occur. For future high power devices, radiative power removal by impurity seeding is very likely required in order to avoid divertor damage by excessive heat flux and to limit target plate erosion to acceptable values [38]. Impurity induced detachment therefore receives a large amount of attention.

Impurities can have a significant impact on both the edge/divertor plasma and the core plasma. In general, the presence of impurities in the core is undesirable because it leads to the dilution of the fusion fuel [70]. It is of interest to confine the impurities in the divertor region with minimal concentrations in the core [41]. This confinement of impurities in the divertor region is characterised by the impurity compression, C_Z, and impurity enrichment, η_z:

$$C_Z = \frac{n_{0,Z}^{div}}{n_Z^{core}} \qquad \eta_Z = \frac{C_Z}{C_D} \tag{2.19}$$

Here $n_{0,Z}^{div}$ is the divertor impurity neutral density, n_Z^{core} is the core impurity density and $C_D = 2n_{D_2}^{div}/\bar{n}_e^{core}$ is the deuterium compression. A number of factors have an impact on C_Z and η_Z, including the divertor geometry, plasma conditions (both core and SOL/divertor) and the impurity species [43, 58, 69, 102, 103]. Maximising C_Z and η_Z is desirable to minimise core contamination while maximising power exhaust in the divertor [56].

The amount of power radiated mainly depends on the impurity species, concentration and the electron temperature [104, 105]. The radiative loss power for an impurity species is obtained using rate coefficients for ionisation, recombination and line excitation. The total radiative cooling rate, L_Z, for an impurity is given by [104]:

$$L_Z = \frac{P_{rad}}{n_e n_Z} = \sum_a f_a \left(L_a^{line} + L_a^{rec} + L_a^{Br} \right) \tag{2.20}$$

Here P_{rad} is the total power radiated by an impurity of density n_Z, $f_a = n_a/n_Z$ is the fractional density of an impurity of ionisation state a and L_a^{line}, L_a^{rec} and L_a^{Br} are corresponding rates of line radiation, recombination radiation and bremsstrahlung respectively which are calculated using collisional-radiative models. These rates depend primarily on the electron temperature and, to a lesser extent, the electron density. More details on the underlying theory used in the calculations of these rates can be found in [105]. The data for these rates (based on [105]) are tabulated in the Atomic Data and Analysis Structure (ADAS) database [106]. Figure 11 shows the L_Z curves obtained from ADAS as a function of temperature for a number of impurities. In general, the cooling rate peaks over a certain temperature range and this range changes depending on the impurity. This temperature dependence means that different impurities radiate in different regions of the tokamak plasma.

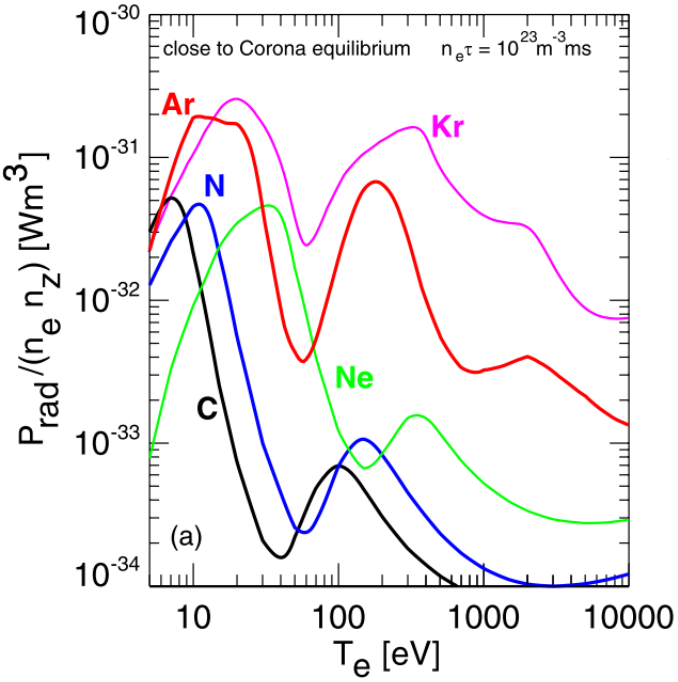

Figure 11: Radiative loss parameter for seed impurities from ADAS for $n_e = 10^{20}$ Wm^3, as the sum of line radiation, recombination-induced radiation and bremsstrahlung for carbon, nitrogen, neon, argon and krypton in coronal equilibrium [38].

The impact of different impurities on the core-divertor system has been the subject of a number

of studies [38, 53, 60–69, 107]. The general observation is that high-Z impurities like argon and krypton usually radiate close to the LCFS in the core whereas nitrogen radiates close to the divertor [38, 63, 66]. Nitrogen is an attractive option as its radiative losses are highest in the divertor relevant temperatures and significantly lower for core temperatures. However, there are concerns about tritium co-deposition through ammonia formation which needs to be understood [26]. Comparing the atomic data of the species considered, argon exhibits the highest radiative efficiency for the temperature range of the divertor. However, its high radiative losses in the core plasma may not permit high argon concentrations. The situation may change when a high enrichment of argon in the divertor is achieved [38]. The impact of different impurities on core energy confinement is less clear. In general, nitrogen has been found to improve confinement (particularly during detachment onset) on most tokamaks [53, 63, 66]. Neon and argon have been associated with varying degrees of confinement degradation in some cases, whereas high radiative power dissipation without significant loss in confinement has been achieved in others [63–66, 69]. In addition, a recent study has indicated improved energy confinement when using a mix of nitrogen and neon or nitrogen and argon as compared to just nitrogen [67]. Establishing the advantages and disadvantages of using a given impurity or a given combination of impurities for power handling remains an active area of research and is not the subject of this work.

Improved control of detachment can contribute to increased impurity compression/enrichment and better compatibility between detached divertor operation and high core performance. Some of the issues regarding detachment control are described in the next part of this discussion.

2.4.2 Detachment control

An idealised detached divertor plasma achieved through impurity seeding can be thought of as four different regions or 'fronts' stacked along the parallel direction as the plasma temperature decreases from upstream to the target, as shown in figure 12. Impurity line radiation normally makes the dominant contribution to power loss and drives most of the reduction in temperature between the X-point and the target. The region where recycled neutrals are ionised, also called the 'recycling region' (labelled as ionisation in figure 12), typically sits on the cold end of this 'radiation front'. The region where other neutral processes like charge exchange and elastic collisions dominate, which primarily remove momentum, usually sits on the cold side of the recycling region. Finally, if the temperature is low enough, a recombination front exists between the target and the charge exchange region. The location and extent of these regions is defined by the temperature distribution in the divertor and the dependence of the reaction rates for (impurity and hydrogenic) line emission, ionisation, charge-exchange, elastic collisions and recombination on the plasma parameters.

From a practical standpoint, it is more useful to think of the detached plasma as consisting of

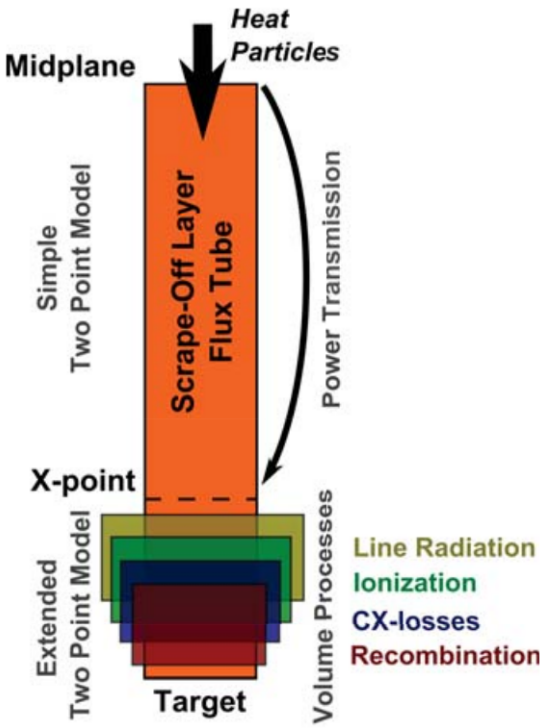

Figure 12: Schematic of a detached SOL, adapted from [108].

two separate regions: the region where most of the power loss occurs or the 'thermal front' and the 'detached region' which sits between the thermal front and the target. The detachment first starts at the divertor target, where the temperature is lowest. Following detachment onset, a roughly uniform low plasma pressure and temperature region expands away from the target towards the X-point. The upstream end of that cold region is called the 'detachment front' which is contiguous to the low temperature edge of the thermal front. The thermal front is a region of steep temperature gradients driven by power losses from the flux tube in which the temperature transitions between the hotter upstream region and either the target (when attached) or the detachment front after detachment. The detached region is dominated by neutral processes like charge exchange and elastic collisions.

In experiments, the detachment front is often observed to move all the way to the X-point [44, 64, 68, 109, 110]. The presence of a low temperature region at or near the X-point can lead to varying degrees of core energy confinement degradation; either directly by introducing a cold region next to, or inside the separatrix; or indirectly, through easier penetration of neutrals and impurities across the separatrix [56]. X-point radiation can occur without much loss of energy confinement [64, 68, 111]. However, that may be due to the large ratio of the power into the SOL compared to the threshold power needed to transition from L-mode to H-mode in those cases, P_{SOL}/P_{LH}. This may not be possible for ITER. The compression/enrichment of impurities and neutrals in the divertor has also been found to degrade during detachment, which can result in

core contamination and also raises concerns for pumping helium in a reactor when the divertor is fully-detached [56, 112]. It is therefore important to identify the optimal detachment front location and to find ways of holding it at that position - feedback control of the detachment front location is a requirement to hold the core-divertor system where needed.

There have been a number of successful detachment feedback control experiments using impurity seeding gases for control of outer divertor detachment in H-mode plasmas [113, 114]. However, the detachment front was only held either at the X-point or the target (on the verge of detachment) in these experiments. The ultimate goal is to determine if there is a core and divertor scenario that is compatible with a cost-effective, energy-producing, controllable reactor, and that allows control of detachment. This requires the ability to hold the detachment front anywhere between the X-point and the target - the detachment front location depends on the divertor magnetic topology and on the values of the following 'control' parameters: Outboard midplane density, n_u, the scrape-off layer impurity density fraction (concentration), $f_I = n_Z/n_e$ (where n_Z is the total impurity density including impurity ions and impurity neutrals), and power crossing the separatrix into the scrape-off layer, P_{SOL} [115, 116]. Holding the front at any location is thought to be difficult in current devices due to an extremely small 'detachment window'. The detachment window for a control parameter $C = n_u,\ f_I$ or P_{SOL} is defined as the range $C_\times - C_t$ where $C_\times$ and C_t are values of C when the front is at the X-point and target respectively. So a bigger detachment window corresponds to better control. An understanding of the dependence of the front location on control parameters is therefore crucial and is a subject of this study.

Issues regarding detachment control and detachment threshold have recently been addressed using an analytical model called, herein, the detachment location sensitivity (DLS) model which provides theoretical predictions of the detachment position dependence (as well as the detachment threshold) on the three control parameters (listed above) and the divertor magnetic topology [76]. The model predicts that increasing connection length and decreasing total magnetic field strength (increasing total flux expansion) from X-point to target increases the detachment window for all control variables. In particular, the sensitivity of the detachment location along the magnetic field to controls is predicted to be inversely proportional to the parallel gradient in the total magnetic field along the field line in the divertor. In other words, detachment location control is improved in regions of strong parallel B-field gradients. The low total flux expansion in the conventional divertor configuration is likely the reason for the narrow detachment window associated with this configuration.

Experimental and numerical studies of a variety of advanced divertor configurations have been carried out [40, 101] to assess their viability as a more suitable and controllable divertor solution for power handling in power plant relevant scenarios. In particular, various long-legged divertor

configurations like the ones shown in figure 13 (especially the Super-X [71]) have received a considerable amount of interest due to their potential for improved power exhaust without significant compromise on core performance. MAST Upgrade will incorporate the Super-X divertor (SXD) configuration which features localised regions of strong parallel B-field gradients.

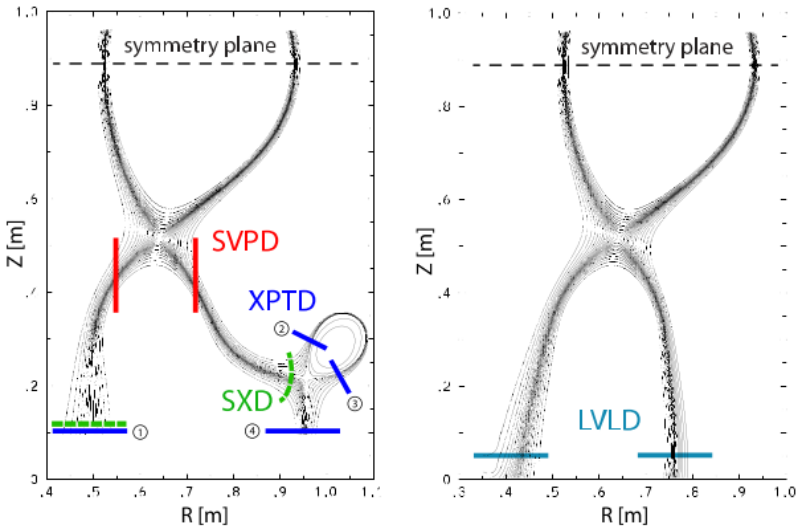

Figure 13: Some advanced divertor configurations [101]. Left: Standard Vertical Plate Divertor (SVPD), Super-X Divertor (SXD) and X-point Divertor (XPTD). Right: Long Vertical Leg Divertor (LVLD).

As mentioned earlier, comparison of the DLS model predictions of detachment location in the MAST-U Super-X geometry with corresponding SOLPS-ITER simulations is one of the topics of this study. In the rest of this chapter, the DLS model and previous numerical studies of MAST-U are briefly reviewed.

2.5 The detachment location sensitivity (DLS) model

In this section, the basic idea behind the DLS model, model assumptions, predictions and how the key expressions are obtained are briefly described. Detailed discussions and derivations can be found in [76].

This 1D treatment balances the divergence of parallel conduction with the net volumetric energy input $H = S - E$ where S is the source of energy (composed mostly of perpendicular heat fluxes), and E is the emissive energy loss by impurity radiation. The equation expressing this balance is:

$$\nabla \cdot \left(\frac{\boldsymbol{B}}{B} \kappa_{\parallel} \frac{\boldsymbol{B}}{B} \cdot \nabla T \right) = -H \tag{2.21}$$

where $\kappa_{\parallel}$ is the Spitzer parallel conductivity, $\kappa_{\parallel} = \kappa_0 T^{5/2}$. Equation 2.21 can be simplified by first

defining a parallel coordinate z and a scaled conductivity κ:

$$\mathrm{d}z = \frac{B_\times}{B}\mathrm{d}l = \frac{B_\times}{B_p}\mathrm{d}l_p \qquad \kappa \equiv \kappa_\parallel B_\times^2/B^2 \tag{2.22}$$

where l is the length along the field line, l_p is the poloidal length, B_p is the magnitude of the poloidal magnetic field, and $B_\times$ is the total field magnitude at the X-point. The parallel coordinate is defined such that $z = 0$ at the target and $z = L$ at the outboard midplane. Note that the length z is actually the volume of the flux tube contained between the divertor plate and the position of interest normalised by a reference area ($\propto 1/B_\times$). Using equations 2.22 and the fact that the magnetic field is divergenceless, $\nabla \cdot \mathbf{B} = 0$, equation 2.21 can be written as:

$$\frac{\mathrm{d}q}{\mathrm{d}z} = H = S - E \tag{2.23}$$

where

$$q = -\kappa\frac{\mathrm{d}T}{\mathrm{d}z} \tag{2.24}$$

The quantity q is a scaled form of parallel heat flux density: $q = q_\parallel B_\times/B$. Since the area of a flux tube varies inversely proportional to B, q can be identified as the total parallel heat flux (rather than heat flux density, $q_\parallel$) through a flux tube which has unit area where $B = B_\times$.

The goal is to predict the detachment front location between the X-point and target as a function of control parameters and to study the impact of the variation in B between the X-point and target on the detachment window. Therefore it is assumed that above the X-point, the emissive energy loss by radiation is negligible, $E \approx 0$; and the net volumetric energy input is primarily composed of perpendicular heat fluxes into the flux tube, $H \approx S$. On the other hand, emissive losses are assumed to overwhelm the local source between the X-point and the target, leading to $H \approx -E$ in this region. In other words, all of the power that enters the flux tube at the X-point position is assumed to be dissipated via impurity radiation.

The impurity radiation power density for a given impurity is represented as the product $E = n_e n_Z Q(T) = n_e^2 f_I Q(T)$ where ($f_I = n_Z/n_e$) is the impurity density fraction, n_Z and n_e are the impurity and electron densities, and Q is the radiative cooling rate for that impurity which depends on temperature (equivalent to L_Z in section 2.4.1). Typically for a detached plasma, in the temperature range between the X-point and target, Q peaks at a certain temperature and falls to small values at much higher or lower temperature.

Solution to the heat conduction equation 2.23 under these assumptions gives rise to a localised radiative region or the 'thermal front'. An example solution is displayed in figure 14. In the following, the subscripts c and h represent values of quantities at the cold and hot ends of the

thermal front and the subscript $\times$ represents values at the X-point position. On the cold side of the thermal front, there is a low temperature region with $T \sim T_c$ where (in principle) $H = 0$. The hot edge of the front is taken to be at temperature T_h where the emissive loss becomes negligible. Above temperature T_h the heat conduction and heat source S determine the temperature's spatial dependence.

The power dissipated in the thermal front, q_f, depends on the control parameters f_I and n_u, and the power passing through the flux tube at the X-point position, q_i, depends on the control parameter P_{SOL}. In steady state, the power dissipated through impurity radiation is equal to the power passing through the flux tube at the X-point position. The condition $q_i = q_f$ leads to expressions for the values of the control parameters for a given detachment front location.

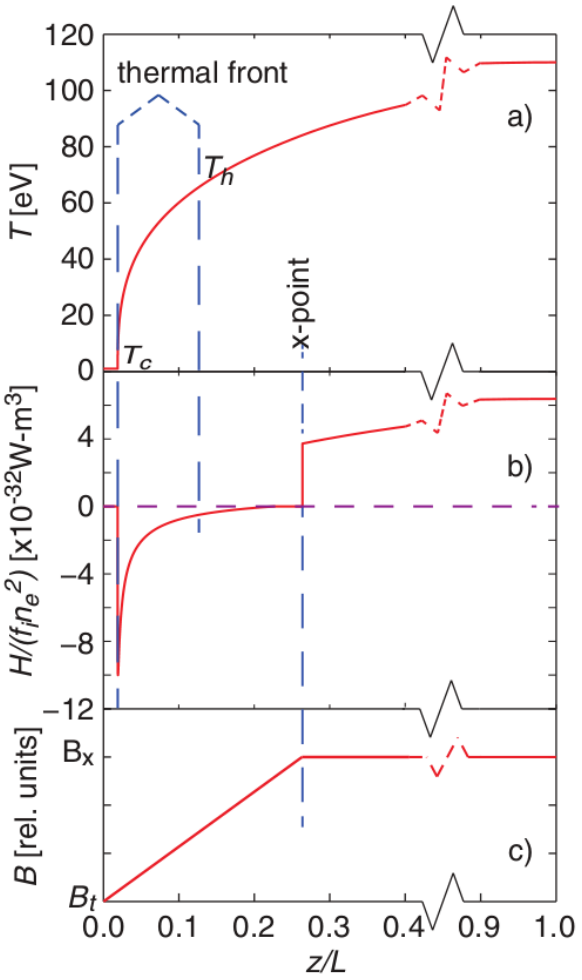

Figure 14: Profiles of (a) thermal front solution to the conduction equation; (b) the corresponding energy sources and sinks, H, normalized to $f_I n_e^2$ to enable the positive values of H at large z to be non-negligible in the figure; and (c) the magnetic field magnitude assumed in the calculations [76].

The heat flux entering the front is simply:

$$q_i = -\int_{z_h}^{L} H \mathrm{d}z \simeq -\int_{z_h}^{L} S \mathrm{d}z \tag{2.25}$$

because E is negligible at the hot end of the front in this model. For simplicity, S can be assumed to be constant above the X-point and negligible below the X-point:

$$S = \begin{cases} 0 & \text{for} \quad z < z_\times \\ S_0 & \text{for} \quad z \geq z_\times \end{cases} \tag{2.26}$$

which results in the following expression for q_i:

$$q_i = -\begin{cases} S_0(L - z_\times) & \text{for} \quad z_h < z_\times \\ S_0(L - z_h) & \text{for} \quad z_h \geq z_\times \end{cases} \tag{2.27}$$

For a characteristic exponential power scrape-off width λ_q, the parallel heat flux density near the separatrix required to exhaust that power is $q_\parallel = P_{SOL}/(\lambda_q 2\pi R B_p/B)$. q_i in this model can therefore be identified with this expression, giving

$$S_0(L - z_\times) = \frac{P_{SOL}}{\lambda_q 2\pi R B_p/B_\times} \tag{2.28}$$

Thus $S_0(L - z_\times) \propto P_{SOL}/\lambda_q$ when other geometrical parameters are constant, enabling one to express the detachment sensitivity dependence on P_{SOL}.

The expression for q_f is obtained by first multiplying equation 2.23 by equation 2.24, and integrating in $q(z)$ on the LHS and over $T(z)$ on the RHS, from the cold end of the front to the hot end. A number of important simplifying assumptions and explicit inclusion of the dependence on B lead to the following expression for q_f:

$$q_f = -\sqrt{2\kappa_0 f_I} n_u T_u \frac{B_\times}{B} \sqrt{\int_{T_c}^{T_h} T^{1/2} Q(T) \mathrm{d}T} \tag{2.29}$$

The most important simplifying assumption here is that the thermal front is sufficiently localised so that the plasma pressure, the impurity fraction and the magnetic field strength can be taken as uniform across the front. In other words, the detachment front and the thermal front are taken to be at roughly the same location. Further, it is assumed that any pressure loss due to plasma neutral interactions only occurs between the target and the cold end of the thermal front - in the same spirit as the two point model, the pressure across the thermal front is equal to the upstream/outboard midplane pressure.

The next step is to specify T_u for equation 2.29 such that it is consistent with q_i. This requires

a model for the variation in B. A simple model for the B variation is adopted:

$$\frac{B}{B_\times} = \begin{cases} B_t/B_\times + (1 - B_t/B_\times)z/z_\times & \text{for} \quad z < z_\times \\ 1 & \text{for} \quad z \geq z_\times \end{cases} \tag{2.30}$$

We can now substitute q_i, equation 2.27, into equation 2.24 and integrate between z_h and L for $z_h < z_\times$ to obtain:

$$[T^{7/2}]_z^L = \frac{7S_0(L - z_\times)}{2\kappa_0} \times \left[\frac{z_\times - z}{3}\left(1 + \left|\frac{B}{B_\times}\right| + \left|\frac{B}{B_\times}\right|^2\right) + \frac{L - z_\times}{2}\right] \tag{2.31}$$

At positions far enough from the upstream end ($z = L$), $(T/T_u)^{7/2}$ is small, so the lower limit (z_h) on the LHS can be omitted. For $z_h \leq z_\times$, one obtains the following expression for the upstream temperature:

$$T_u \simeq \left(\frac{7S_0(L - z_\times)}{2\kappa_0}\right)^{2/7} \times \left[\frac{z_\times - z_h}{3}\left(1 + \left|\frac{B}{B_\times}\right| + \left|\frac{B}{B_\times}\right|^2\right) + \frac{L - z_\times}{2}\right]^{2/7} \tag{2.32}$$

This expression for T_u can be substituted into equation 2.29 to get:

$$q_f = -U\sqrt{f_I}n_u\frac{B_\times}{B_h}[S_0(L - z_\times)]^{2/7} \times \left[\frac{z_\times - z_h}{3}\left(1 + \left|\frac{B}{B_\times}\right| + \left|\frac{B}{B_\times}\right|^2\right) + \frac{L - z_\times}{2}\right]^{2/7} \tag{2.33}$$

where the constant U is

$$U = 7^{2/7}(2\kappa_0)^{3/14}\sqrt{\int_{T_c}^{T_h} T^{1/2}Q(T)\mathrm{d}T} \tag{2.34}$$

Now, setting $q_i = q_f$ enables one to solve for any one of the control variables $C = [n_u, f_I, P_{SOL}]$ as a function of the front position z_h/L for $z_h \leq z_\times$. While the DLS model provides predictions for the absolute values of control parameters for a given z, the primary purpose of the model is to study the *relative* changes in the control parameters for some movement in z; and thus, the impact of total magnetic flux expansion on the detachment window. The ratio of the value of a control parameter when the front is at the X-point, $C_\times$, to that when the front is somewhere between the X-point and target, C_h, is given by:

$$\frac{C_\times}{C_h} = \left\{\frac{B_\times}{B_h}\left[\frac{2(z_\times - z_h)}{3(L - z_\times)}\left(1 + \left|\frac{B_h}{B_\times}\right| + \left|\frac{B_h}{B_\times}\right|^2\right) + 1\right]^{2/7}\right\}^\beta \tag{2.35}$$

The factor β is 1, 2 and $-7/5$ for n_u, f_I and P_{SOL} respectively. In particular, the ratio of the

values of each control variable for when the front is at the target and when it is at the X-point can be obtained simply by setting $z_h = 0$ and $B_h = B_t$ in equation 2.35.

The normalised detachment window for the control variables considered here are defined as:

$$\Delta\tilde{f}_I = (f_{I,\times} - f_{I,t})/f_{I,t} \tag{2.36}$$

$$\Delta\tilde{P}_{SOL} = (P_{SOL,t} - P_{SOL,\times})/P_{SOL,\times} \tag{2.37}$$

$$\Delta\tilde{n}_u = (n_{u,\times} - n_{u,t})/n_{u,t} \tag{2.38}$$

The DLS model predicts that total flux expansion significantly widens the detachment window for all control parameters. This is illustrated in figure 15 which shows $\Delta\tilde{C}/\Delta\tilde{C}|_{B_\times/B_t=1}$ for $B_\times/B_t$ increasing from 1.0 to 3.0, where $\Delta\tilde{C}|_{B_\times/B_t=1}$ is $\Delta\tilde{C}$ when $B_\times/B_t = 1$. It can be seen that total flux expansion, $B_\times/B_t$, has a significant impact on the detachment window. The detachment window in impurity seeding, $\Delta\tilde{f}_I$, has the strongest increase with increasing $B_\times/B_t$. The increase in the detachment window for P_{SOL} is of particular relevance for transients in core power loss (e.g. H-L energy confinement transitions or ELMs), which are ideally absorbed in the divertor plasma whilst keeping the divertor region detached and the detachment front in an optimal position.

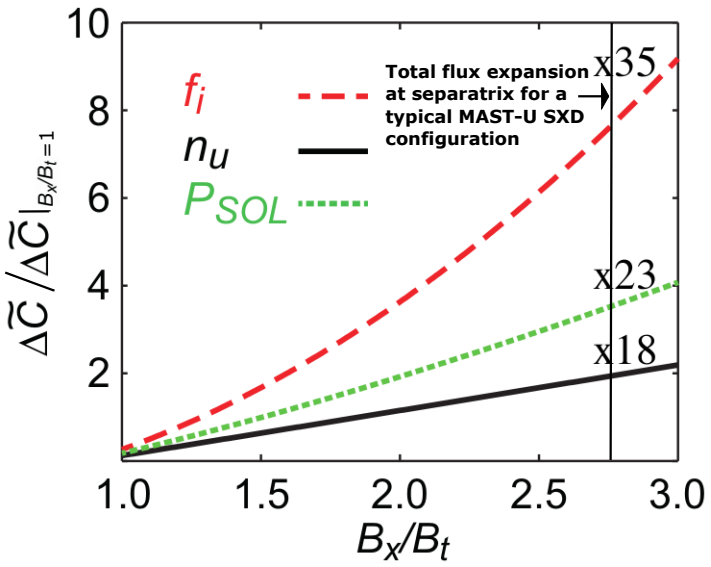

Figure 15: Relative change in the normalized detachment window, $\Delta\tilde{C}$, with changing $B_\times/B_t$ (the values of $\Delta\tilde{C}$ at $B_\times/B_t = 1$ are $\Delta\tilde{n}_u = 0.12$, $\Delta\tilde{f}_I = 0.26$ and $\Delta\tilde{P}_{SOL} = 0.18$) [76].

Total flux expansion is one of the key features of the MAST-U Super-X configuration. In the next (and final) section of this chapter, previous numerical studies of MAST-U are reviewed.

2.6 MAST Upgrade and the Super-X divertor

The Mega Ampere Spherical Tokamak (MAST) was one of the largest spherical tokamaks in the world and provided new perspectives on tokamak physics for ITER and beyond. It served as a platform for exploring the potential of the spherical tokamak as a compact and economic route to a fusion power plant. It has a major radius $R \approx 0.85$ and a minor radius $a \approx 0.65$, giving it an aspect ratio $A \approx 1.3$. The device has recently undergone a major upgrade and operations began in early 2021. MAST Upgrade (or MAST-U) has been designed to optimize the Super-X configuration [75, 81, 82]. The major role of Super-X is to reduce plasma temperatures and heat loads on targets via long connection length and larger target wetted area achieved by magnetic flux expansion (targets at large radius). Additionally, the design gains from improved divertor closure which helps to separate neutrals and impurities from the confined region and the upstream SOL, and which enables it to reach higher neutral pressures in the divertor volume.

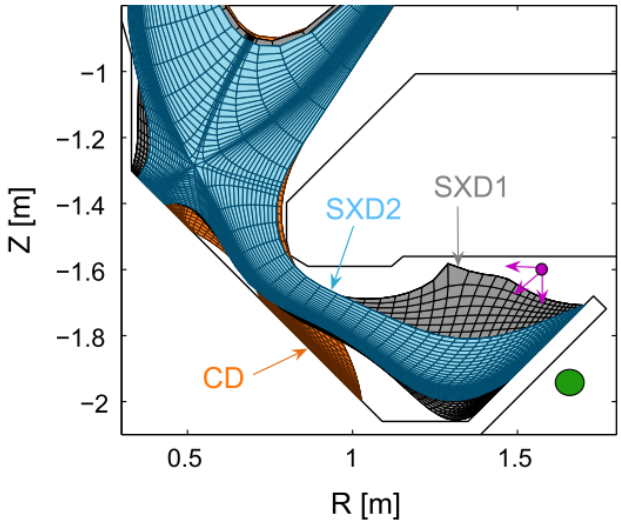

Figure 16: Possible configurations in MAST-U. Pump location in green and fuelling/seeding location in purple [75].

As part of the preparations for MAST-U operations, a number of numerical investigations have been carried out using SOLPS-ITER as well as earlier versions of the code. However, these studies primarily focused on comparing the performance of the conventional divertor (CD) and Super-X divertor configurations (SXD1 and SXD2) in MAST-U, shown in figure 16 [74, 75, 78, 117–119]. As mentioned earlier (section 1.5), in this work, the SOLPS-ITER code package is used to take a closer look at the Super-X configuration. Building primarily on the work presented in [78], we focus on the SXD1 configuration. In particular, we focus on the role of the magnetic geometry on detachment control and on comparing strongly detached conditions obtained through impurity radiation driven and upstream density driven approaches, as these aspects have not been the focus of previous work on MAST-U. Nevertheless, it useful to briefly review previous numerical studies

on detachment in MAST-U, the focus of the rest of this chapter. These studies generally indicate that the divertor performance is improved significantly in the Super-X configuration, primarily through a combination of increased total flux expansion and volumetric power loss, and improved neutral compression due to the tight baffling.

For example, in attached conditions in H-mode, the peak power load on the outer targets was found to be lower by a factor ~ 4.5 in the SXD configurations compared to the CD configuration for almost identical upstream/outboard midplane conditions. This was primarily a result of the increased total flux magnetic expansion in the Super-X configurations [117]. The reduction of the peak target power load in SXDs with respect to CD was found to depend on the collisionality regime and according to the numerical studies, this goes from a factor of ~ 4.5 (both SXDs and CD attached) to ~ 100 before detachment is even initiated in the CD configuration as the collisionality is increased [118]. In general, in the high recycling regime and/or around detachment onset, the power radiated by impurities like carbon and nitrogen in the SXD configuration is approximately twice as large as in the CD configuration; mainly due to the larger connection length in the SXD configuration [74, 75, 118, 119].

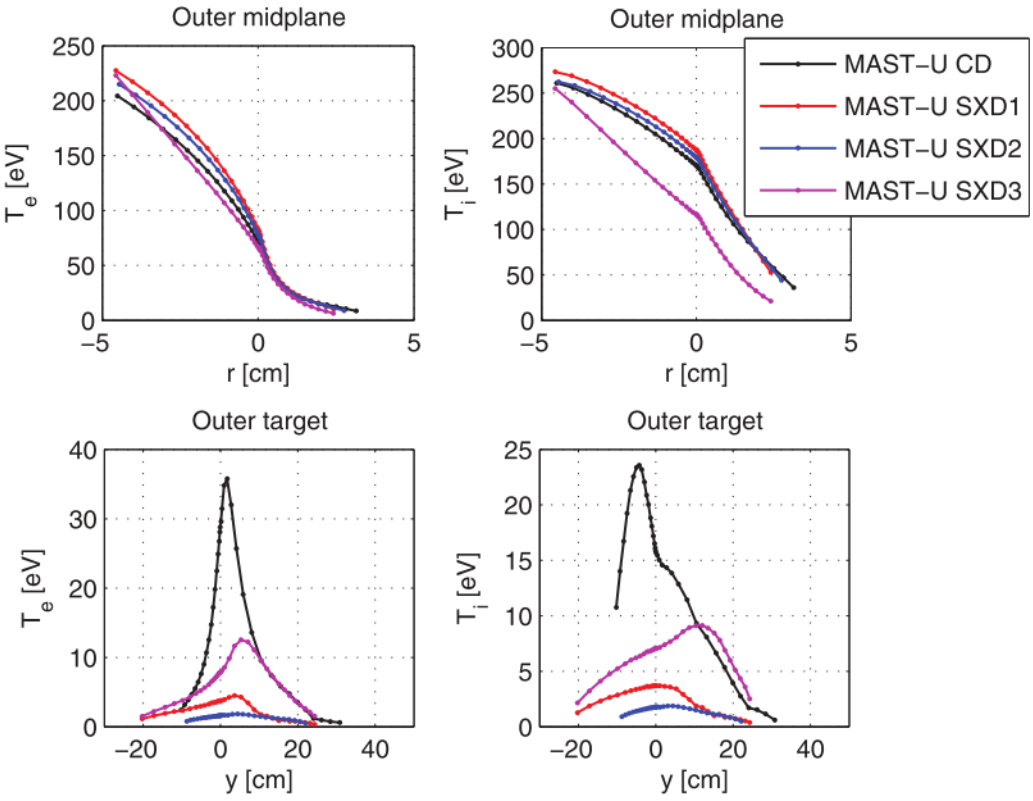

Figure 17: Radial profiles of T_e (left) and T_i (right) obtained from SOLPS-ITER simulations [75].

In very high recycling and/or detached conditions, volumetric power loss due to plasma-neutral interactions and radiation play a more important role than the magnetic topology [74, 118]. However, as mentioned earlier, an important effect of the increased total flux expansion in the Super-X

configuration is access to the detached regime at lower upstream densities and generally lower impurity levels. This is due to the strong impact of total flux expansion on target quantities in the low recycling regime [117]. For MAST-U, the Super-X configuration reduces the upstream density threshold for the transition to detachment by a factor of 3-4 in L-mode [75, 118] and a factor of 2.4 in H-mode [78]; and the impurity (nitrogen) seeding rate required to access detachment in H-mode is 7 times smaller than that for the conventional configuration [74].

The divertor closure with respect to neutrals is dramatically increased in MAST-U thanks to the separation of the upper SOL and divertor regions by a baffle. With the baffle in place, the ratio between the ionisation source outside the divertor and the total ionisation source was reduced by a factor of 10 in the SXDs compared to the CD. The flux of neutral species to the core was reduced by a factor of 4 for deuterium atoms and a factor of 12 for molecules [75]. The effect of the baffle can be clearly seen in figure 17 [75] which displays radial profiles of the electron and ion temperatures at the outboard midplane and outer target for CD, SXD1, SXD2 and SXD3, where SXD3 is essentially SXD1 with the baffle removed, for the same input power and core density. When the baffle is removed, the neutrals easily escape the divertor volume resulting in higher target temperatures and loss of detachment, demonstrating the important role of the baffle in detachment access.

2.7 Summary

Divertor plasma detachment, which is a complex multi-physics and covering all aspects of it is beyond the scope of this thesis, is widely seen as a potential solution to the tokamak exhaust problem. While divertor detachment can lead to a significant reduction in the heat loads incident on the divertor targets, it can also have a deleterious effect on the core plasma performance. Advanced divertor configurations have been proposed to make detachment more compatible with a high performance core plasma. The Super-X configuration has received a large amount of attention, which has been optimised and implemented in the MAST-U tokamak. Previous numerical investigations of the MAST-U Super-X divertor performance have primarily focused on the comparison with the conventional divertor configuration, which indicate that detached divertor operation is significantly more compatible high core performance in the Super-X configuration. However, there are a number of issues that need to be addressed to evaluate the viability of Super-X as an exhaust solution. In this work, we focus on the features of the MAST-U Super-X divertor that may enhance detachment control, and the aspects of detached divertor operation that are likely to be important in this configuration for future high power machines. The next chapter covers the specific aims of this work and methodology that is adopted.

Chapter 3

Aims and methodology

The goal of any exhaust solution is to keep the steady state and transient heat loads below material limits without significantly degrading the core performance. Impurity radiation driven divertor detachment, which can be reliably controlled, is very likely to be part of such a solution.

Although a number of experimental studies have focused on the issue of detachment control (as described earlier), few numerical studies specifically address this issue [101, 120]. Previous numerical studies concerning the MAST-U SOL and divertor physics have primarily focused on comparing the performance of the CD and SXD configurations, e.g. comparing target conditions when the upstream conditions are similar or comparing the distribution of volumetric losses when the target conditions are similar. The subject of detachment control in MAST-U has not yet been addressed. Numerical studies that focus on detachment control in MAST-U are therefore of interest, and one of the topics addressed in this work.

Strongly detached divertor conditions have been observed to vary significantly across devices and often depend on the approach taken to access detachment. In density ramp experiments, volume recombination of ions into atoms can account for a large fraction of the reduction in the total number of particles incident on the target per second, $\Gamma_{t,tot}$, (75%) as observed in Alcator C-Mod [47]. Or the role of volume recombination can be small for a density ramp detachment as in TCV (10-15% [48]); C-Mod is a much higher density and power density machine which may contribute to such differences. In contrast, experiments in which impurities are injected to achieve detachment, volume recombination typically has a much smaller role in bringing down $\Gamma_{t,tot}$: In C-Mod the reduction in $\Gamma_{t,tot}$ due to volume recombination drops from 75% during a density ramp to ≈10% with N-seeding to achieve detachment [52]. Similarly, the role of volume recombination in TCV drops from small (10-15%) during a density ramp to below measurable [48] for detached, N-seeded discharges. Strong volume recombination in the divertor is desirable as it reduces both surface recombination heat loads (which can be the dominant contribution to divertor heat loads in detached conditions, when the plasma temperature drops below $\sim$ 2eV), and sputtering of

PFC surfaces. Therefore, it is of interest to numerically explore how, in current machines, strongly detached divertor conditions achieved by ramping up the upstream density are different from those achieved by injecting extrinsic impurities; this may help gain insights relevant to detached divertor operation in high power devices. Such a comparison is the other topic addressed here.

This work builds primarily on the SOLPS-ITER simulations of MAST-U presented in [78], which focus on the mid-plane density detachment threshold in conventional and Super-X divertor configurations. In this work, the SOLPS-ITER code package is used to take a closer look at the MAST-U Super-X divertor configuration. Two parameter scans were initially performed at fixed input power to obtain a range of steady solutions which represent a transition from attached (high-recycling) to strongly detached conditions. In the first detachment scan, the main ion (D_2) fuelling rate is varied (with no extrinsic impurities) to obtain a scan in the outboard midplane density, n_u. The second detachment scan varies the divertor impurity fraction, f_I, by varying the seeding rate of nitrogen atoms (N) at a fixed fuelling rate.

The main aims of this work are as follows:

- To study how the divertor plasma characteristics change as a function of external controls from detachment onset through to stongly detached conditions and to investigate the role of parallel B-field gradients in detachment control, the core characteristic of the Super-X
- To carry out a detailed comparison of conditions when the divertor is detached due to a high upstream density to those when it is a result of significantly increased impurity radiation at a relatively low upstream density

Concerning detachment control, for each set of the steady state detached solutions obtained in this study, the movement of various detachment location markers is tracked as a function of main ion and impurity injections rates, and also the corresponding 'physics' control parameters; the results are compared with the predictions of the DLS model. In the DLS model, only a linear variation in the divertor B field is considered, unlike what occurs in MAST-U. To address this limitation in the current application of the model, the DLS model is generalised to obtain predictions for arbitrary B-field variation in the divertor, and applied to the MAST-U Super-X geometry. In both scans, a reduction in the sensitivity of the detachment location to controls (increasing n_u or f_I) is observed in a region of high parallel gradients in B, consistent with the DLS model predictions.

As for the comparison of strongly detached solutions obtained from the two scans, important qualitative differences are observed between the two cases. In particular, volume recombination is found to play a significant role in reducing $\Gamma_{t,tot}$ in strongly detached solutions obtained from the fuelling scan but was negligible in the nitrogen seeded scan, consistent with experimental

observations in other tokamaks. A detailed energy, momentum and particle balance analysis of the detached region was performed to understand the reason for these differences, and it was hypothesized that qualitative features of the nitrogen seeded detached divertor can be recovered in non-seeded case by turning off $D^+ - D_2$ elastic collisions. This hypothesis was confirmed by performing a third scan - the fuelling scan was repeated with $D^+ - D_2$ elastic collisions excluded.

Each of the two topics addressed in this work has an associated 'key' observation, summarised in chapter 4. The comparison of DLS model predictions with simulation results is the subject of chapter 5 and chapter 6 focuses on the impact of $D^+ - D_2$ elastic collisions on strongly detached conditions. In the rest of this chapter, the SOLPS-ITER code package and the simulation setup are described.

3.1 The SOLPS-ITER code package

The SOLPS-ITER code package (henceforth referred to as SOLPS) is a well established and widely used edge plasma simulation software [46, 85]. It consists of two key components which are coupled together: the B2.5 code which solves plasma fluid equations for multiple ion species [121, 122], and the EIRENE code which uses the Monte-Carlo method to model the transport of kinetic neutrals [123, 124]. The code has undergone several changes over the years. In this chapter, only the set of plasma fluid equations evolved by B2.5 in *this* study are briefly described along with a general description of EIRENE. More details can be found in [46, 85, 122, 123].

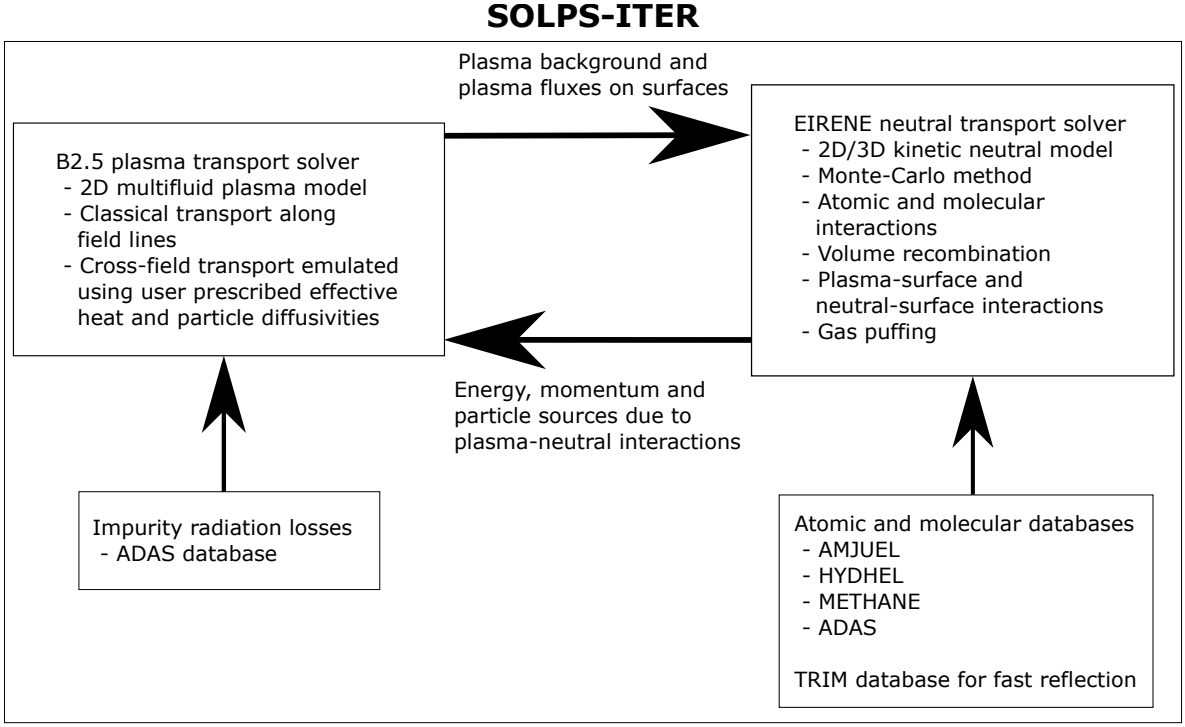

Figure 18: Information exchange between B2.5 and EIRENE

The basic interaction between B2.5 and EIRENE is described in figure 18. The fluid equations are solved by B2.5 to model plasma transport along magnetic field lines whereas turbulence driven cross-field transport is modelled as effective diffusion using user prescribed diffusivities for heat and particles. Each time EIRENE is called by B2.5, it is provided with the plasma background and the plasma fluxes on solid surfaces. EIRENE uses this information to evolve the trajectories of kinetic neutrals across its 2D or 3D simulation domain. Neutrals are generated from the surface using the plasma flux provided by B2.5, and recycling and sputtering coefficients specified by the user. Special 'pumping surfaces' can also be specified. Gas puffing can be modelled as point sources in the domain which emit neutrals at a specified rate. The plasma background provided by B2.5 is used to estimate the volumetric neutral source due to recombination, the plasma source due to neutral ionisation, as well as the energy and momentum exchange between the plasma and the neutrals. One of the main functions of EIRENE is to return a 2D map of the plasma energy, momentum and particle sources due to plasma-neutral interactions to B2.5 for a given plasma background. SOLPS makes use of several databases to model impurity radiation losses, the transport of neutrals through the plasma by accounting for interactions like charge-exchange and elastic collisions, and the generation of neutrals from surfaces due to plasma-surface interactions, covered in significant detail in [124].

The MAST-U B2.5-EIRENE grid used in this work is shown in figure 19(a). It corresponds to a Super-X divertor equilibrium similar to the ones used in previous MAST-U studies using SOLPS [78, 117]. The plasma fluid equations are solved on the $nx = 148$ (poloidal) $\times$ $ny = 34$ (radial) flux aligned quadrilateral B2.5 grid, shown in red. The triangular EIRENE grid is shown in black, which overlaps with all of the B2.5 grid and also extends all the way out to the wall. The B2.5 grid is internally mapped on to a rectangular computational grid as shown in figure 20. The physical domain is typically decomposed around the X-point in edge transport codes as shown in figure 19(b). Such a domain decomposition means that while the inner and outer core regions, and the inner and outer PFRs of the lower divertor, are connected in real space, they are separated on the rectangular computational grid. This is taken care of internally by applying appropriate boundary conditions on these segment boundaries which transfer fluxes across to the right segment.

Fluid equations are evolved in a 'toroidal-poloidal-radial' coordinate system, but variations in the toroidal (z) direction are not included (toroidal symmetry is assumed). The poloidal (x) coordinate surfaces are projections of the magnetic flux surfaces on the poloidal plane. The radial (y) coordinate is the direction perpendicular to the magnetic surfaces. Fluid equations in this orthogonal coordinate system are expressed using the metric coefficients h_x, h_y and h_z:

$$h_x = \frac{1}{|\nabla x|} \qquad h_y = \frac{1}{|\nabla y|} \qquad h_z = \frac{1}{|\nabla z|} = 2\pi R \tag{3.1}$$

These coefficients are used to define the derivatives in the code coordinates. The volume of a computational cell is given by the product of these metric coefficients: $\sqrt{g} = h_x h_y h_z$. Poloidal projections of vector quantities are obtained using the factor $b_x = B_x/|B|$.

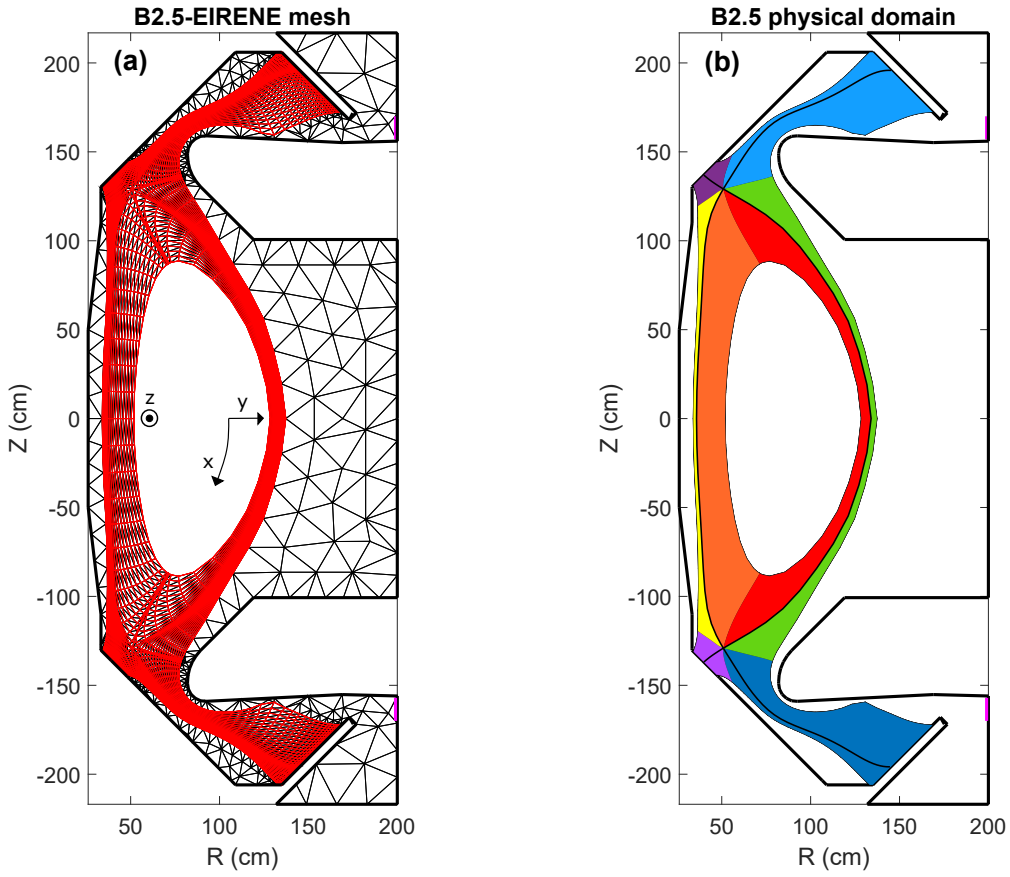

Figure 19: (a) B2.5 mesh (red), EIRENE mesh (black) and pumping surfaces (pink) (b) Decomposition of the physical B2.5 domain

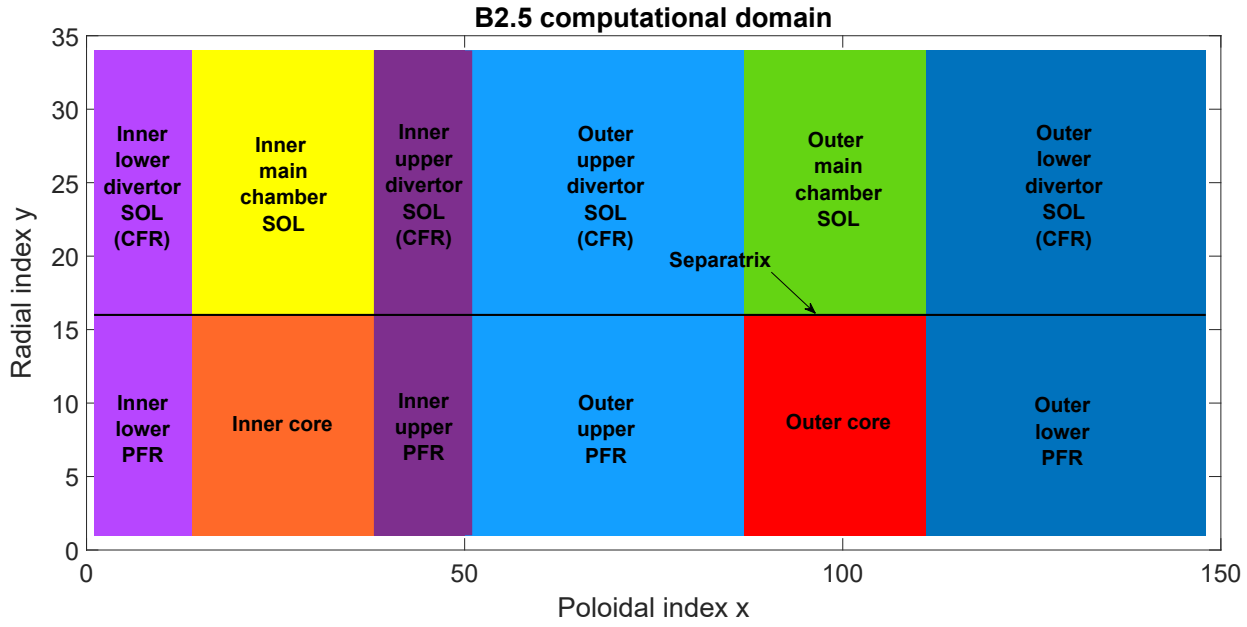

Figure 20: Decomposition of the B2.5 computational domain

3.1.1 The B2.5 multifluid plasma transport model

Edge/SOL plasma simulation codes typically evolve fluid equations that are based on the Braginskii equations which describe transport in a strongly magnetised ($\omega_{c,a}\tau_a >> 1$), collisional ($\lambda_{mfp,a} << L$) and fully ionised plasma for electrons and a single ion species [97]. Here $\omega_{c,a}$ is the gyrofrequency of a species a, τ_a is collision time, $\lambda_{mfp,a}$ is the mean free path and L is macroscopic length scale of the system. Extensions to the Braginskii equations to include multiple species have been provided by Balescu [125], and more recently by Zhdanov [126], both of which have been implemented in SOLPS and the user has the option to choose between these extensions. The general form of plasma fluid equations can be found in [97, 125–127], not reproduced in this thesis. Most previous SOLPS work concerning MAST and MAST-U has used the Balescu model (including the work which this thesis builds on, [78]), so in this work we stick to this option. In the following, implementation of the Balescu multifluid equations in B2.5 is described. For each ion species, the continuity equation 3.2 is solved for the density, the parallel momentum balance equation 3.6 is solved for the parallel velocity and the heat balance equation 3.11 is solved for the ion temperature - all ion species share the same ion temperature. There is also an option to solve the potential equation for the parallel current. However, as in [78] (and most previous MAST and MAST-U work), this option is not used in this work, i.e. the plasma flow is ambipolar. The electron density is obtained from the quasineutrality condition and the ambipolarity condition is used for the electron parallel velocity. The electron temperature is obtained by solving the electron heat balance equation 3.10.

Continuity equation

The ion continuity equation is solved for the particle density n_a for each ion species a:

$$\frac{\partial n_a}{\partial t} + \frac{1}{\sqrt{g}}\frac{\partial}{\partial x}\left(\frac{\sqrt{g}}{h_x}\Gamma_{a,x}\right) + \frac{\partial}{\partial y}\left(\frac{\sqrt{g}}{h_y}\Gamma_{a,y}\right) = S_a^n \tag{3.2}$$

The electron density is obtained from the quasi-neutrality condition: $n_e = \sum_a Z_a n_a$. The poloidal and radial particle fluxes, $\Gamma_{a,x}$ and $\Gamma_{a,y}$, are given by:

$$\Gamma_{a,x} = b_x v_{a,||} n_a \tag{3.3}$$

$$\Gamma_{a,y} = -D_{n,a}\frac{1}{h_y}\frac{\partial n_a}{\partial y} \tag{3.4}$$

The turbulence driven 'anomalous' transport of particles is emulated by prescribing the anomalous particle diffusivity, $D_{n,a}$. In H-mode modelling, the presence of the edge heat and particle transport barriers is accounted for by reducing the heat and particle diffusivities in a narrow region inside the separatrix to achieve the desired H-mode outboard midplane density and temperature profiles.

The particle source S_a^n is composed of sources/sinks of ion species a due to ionisation, $S_{a,I}^{n,B2.5}$, recombination, $S_{a,R}^{n,B2.5}$, and charge exchange, $S_{a,CX}^{n,B2.5}$, on the B2.5 side. In B2.5-EIRENE coupled simulations, the B2.5 particles sources are due to electron-ion and ion-ion interactions. Additional sources associated with the plasma-neutral interactions are introduced by EIRENE, $S_a^{n,Eir}$.

$$S_a^n = S_{a,I}^{n,B2.5} + S_{a,R}^{n,B2.5} + S_{a,CX}^{n,B2.5} + S_a^{n,Eir} \tag{3.5}$$

Parallel momentum balance equation

The parallel (ion) momentum balance equation is solved for the parallel velocity $v_{||,a}$ of an ion species a:

$$m_a \frac{\partial}{\partial t}(n_a v_{||,a}) + \frac{1}{h_z\sqrt{g}}\frac{\partial}{\partial x}\left(\frac{h_z\sqrt{g}}{h_x}\Gamma_{a,x}^m\right) + \frac{1}{h_z\sqrt{g}}\frac{\partial}{\partial y}\left(\frac{h_z\sqrt{g}}{h_y}\Gamma_{a,y}^m\right) = S_a^m \tag{3.6}$$

The poloidal and radial momentum fluxes, $\Gamma_{a,x}^m$ and $\Gamma_{a,y}^m$, are given by:

$$\Gamma_{a,x}^m = \begin{cases} m_a v_{a,||}\Gamma_{a,x} - \frac{4}{3}\eta_{a,x}^{CL}\frac{\partial v_{||,a}}{h_x \partial x}; & a \neq 1 \\ m_a v_{a,||}\Gamma_{a,x} + \frac{4}{3}\eta_{a,x}^{CL}\frac{\partial \ln h_z}{h_x \partial x}v_{a,||} - \frac{4}{3}\eta_{a,x}^{CL}\frac{\partial v_{a,||}}{h_x \partial x}; & a = 1 \end{cases} \tag{3.7}$$

$$\Gamma_{a,y}^m = m_a v_{a,||}\Gamma_{a,y} - \eta_{a,y}^{AN}\frac{\partial v_{||,a}}{h_y \partial y} \tag{3.8}$$

Here the radial viscosity $\eta_{a,y}^{AN} = m_a n_a D_{n,a}$ depends on the cross-field particle diffusivity and $\eta_{a,x}^{CL}$ is the poloidal projection of the Balescu parallel viscosity [125].

The momentum source S_a^m is composed of:

$$S_a^m = -\frac{b_x}{h_x}\frac{\partial n_a T_i}{\partial x} - \frac{b_x}{h_x}\frac{Z_a n_a}{n_e}\frac{\partial n_e T_e}{\partial x} - S_{a,||}^m + S_{a,CF}^m + S_{a,fr}^m + S_{a,therm}^m + S_{a,I}^{m,B2.5} + S_{a,R}^{m,B2.5} + S_{a,CX}^{m,B2.5} + S_{Eir}^m \tag{3.9}$$

The first two terms on the RHS of equation 3.9 are sources due the electron and ion static pressure gradients. The sources $S_{a,||}^m$ and $S_{a,CF}^m$ are due to parallel viscosity and the centrifugal force. The terms $S_{a,fr}^m$ and $S_{a,therm}^m$ represent sources due to friction of ion species a with all the other ion species [128], and due to the thermal force associated with the parallel temperature gradient [128]. Momentum sources due to ionisation, recombination and charge-exchange interactions between an ion species a with all other ions are given by $S_{a,I}^{m,B2.5}$, $S_{a,R}^{m,B2.5}$, and $S_{a,CX}^{m,B2.5}$. Additional sources due to plasma-neutral interactions, S_{Eir}^m, are given by EIRENE.

Electron and ion heat balance equations

The electron and ion heat balance equations are solved for the electron and ion temperatures T_e and T_i:

$$\frac{3}{2}\frac{\partial}{\partial t}(n_e T_e) + \frac{1}{\sqrt{g}}\frac{\partial}{\partial x}\left(\frac{\sqrt{g}}{h_x}\tilde{q}_{e,x}\right) + \frac{1}{\sqrt{g}}\frac{\partial}{\partial y}\left(\frac{\sqrt{g}}{h_y}\tilde{q}_{e,y}\right) = S_e^{heat} \tag{3.10}$$

$$\frac{3}{2}\frac{\partial}{\partial t}(n_i T_i) + \frac{1}{\sqrt{g}}\frac{\partial}{\partial x}\left(\frac{\sqrt{g}}{h_x}\tilde{q}_{ix}\right) + \frac{1}{\sqrt{g}}\frac{\partial}{\partial y}\left(\frac{\sqrt{g}}{h_y}\tilde{q}_{iy}\right) = S_i^{heat} \tag{3.11}$$

All ion species have the same temperature T_i in this model. The poloidal and radial electron heat fluxes, $\tilde{q}_{e,x}$ and $\tilde{q}_{e,y}$, and ion heat fluxes, $\tilde{q}_{i,x}$ and $\tilde{q}_{i,y}$, are given by:

$$\tilde{q}_{e,x} = \frac{3}{2}\left[\sum_a Z_a \Gamma_{a,x}\right] T_e - \kappa_{e,x}^{CL}\frac{1}{h_x}\frac{\partial T_e}{\partial x} \tag{3.12}$$

$$\tilde{q}_{e,y} = \frac{5}{2}\left[\sum_a Z_a \Gamma_{a,y}\right] T_e - \kappa_{e}^{AN}\frac{1}{h_y}\frac{\partial T_e}{\partial y} \tag{3.13}$$

$$\tilde{q}_{i,x} = \frac{3}{2}\left[\sum_a Z_a \Gamma_{a,x}\right] T_i - \kappa_{i,x}^{CL}\frac{1}{h_x}\frac{\partial T_i}{\partial x} \tag{3.14}$$

$$\tilde{q}_{i,y} = \frac{5}{2}\left[\sum_a Z_a \Gamma_{a,y}\right] T_i - \kappa_{i}^{AN}\frac{1}{h_y}\frac{\partial T_i}{\partial y} \tag{3.15}$$

The anomalous cross-field heat conductivities, $\kappa_e^{AN} = n_e \chi_e^{AN}$ and $\kappa_i^{AN} = \chi_i^{AN}\sum_a n_a$, depend on the user prescribed electron and ion heat diffusivities, χ_e^{AN} and χ_i^{AN}. Poloidal projections of the parallel electron and ion heat conductivities, $\kappa_{e,x}^{CL}$ and $\kappa_{i,x}^{CL}$, are based on Balescu [125].

The heat sources S_e^{heat} and S_i^{heat} are composed of:

$$S_e^{heat} = -\frac{n_e T_e}{\sqrt{g}}\frac{\partial}{\partial x}\left(\frac{\sqrt{g}}{h_x} b_x v_{e,||}\right) - Q_\Delta - Q_R + Q_e^{Eir} \tag{3.16}$$

$$S_i^{heat} = -\sum_a \frac{n_a T_i}{\sqrt{g}}\frac{\partial}{\partial x}\left(\frac{\sqrt{g}}{h_x} b_x v_{a,||}\right) + \sum_a \left(\frac{4}{3}\eta_{a,x}^{CL}\left(\frac{\partial v_{a,||}}{h_x \partial x}\right)^2 + \eta_a^{AN}\left(\frac{\partial v_{a,||}}{h_y \partial y}\right)^2\right) + Q_\Delta + Q_{F,ab} + Q_{iz}^{B2.5} + Q_{rec}^{B.25} + Q_i^{Eir} \tag{3.17}$$

The first terms on the RHS of equations 3.16 and 3.17 are the sources due to compressional effects. The heat exchange between electrons and ions through coulomb collisions is given by Q_Δ. The power lost through Bremsstrahlung, line radiation and ionisation of non-neutral species is given by Q_R with cooling rates obtained from ADAS. $Q_{F,ab}$ is the total heat source associated with the friction between species a and all other ion species. The sources $Q_{iz}^{B2.5}$ and $Q_{rec}^{B2.5}$ on the B2.5 side are due to ionisation of ions and recombination of ions to lower charge states (not neutralisation).

As usual, the sources due to interactions with neutrals and neutralisation of ions, Q_e^{Eir} and Q_i^{Eir}, are given by EIRENE.

Kinetic corrections to the B2.5 fluid model

In general, plasma fluid models assume that the electron and ion mean free paths, λ_{ee} and λ_{ii}, are significantly smaller than the length scale, L, of the system being considered. The B2.5 fluid equations are only used to model transport along the magnetic field and the corresponding transport coefficients are essentially a function of, and positively correlated with, the mean free path. In situations where the condition $\lambda_{ee},\ \lambda_{ii} << L$ is not met, the transport along the field lines can approach unphysically high values. The parallel fluxes in these situations are limited by employing kinetic corrections to the transport coefficients to extend the valid parameter range of the fluid approach. For example, the classical parallel electron heat conductivity, κ_e^{CL}, is modified as follows:

$$\tilde{\kappa}_e^{CL} = \frac{\kappa_e^{CL}}{1 + |q_{CL}/q_{fl}|} \tag{3.18}$$

$$q_{CL} = -\tilde{\kappa}_e^{CL} \partial_{||} T_e \tag{3.19}$$

$$q_{fl} = \alpha_{fl} n_e T_e^{3/2} / \sqrt{m_e} \tag{3.20}$$

The heat flux limit applied to this model, q_{fl}, is the equivalent convected electron heat flux density multiplied by the flux limiter coefficient, α_{fl}. Similar limits are applied, in [78] and therefore in this work, to the ion heat flux, momentum flux, the thermo-electric coefficient and friction force, summarised in table 1.

flux variable	el. heat	ion heat	viscosity	thermo-electric coefficient	friction force
limiter coefficient	0.3	1.0	0.5	0.5	0.5

Table 1: Flux limiter coefficients used in the simulations presented in this thesis.

Boundary conditions

Boundary conditions in the B2.5 code are implemented through boundary sources in additional small volume elements along the boundaries which are not part of the physical domain. A flux, Γ, through an area, A, towards the additional volume element at the boundary can be enforced by placing a sink $-S$ in this element, which would result in $\Gamma A = -S$ at the boundary. The sink $-S$ can be a function of the local plasma parameters, allowing the user to prescribe not only fluxes but also plasma parameters or mixed conditions at the boundaries. A large number of options are available to the user. There are 27 options for the continuity equation, each identified by the 'BCCON' number that is set in the input file; 17 'BCMOM' options for the parallel momentum

balance equation; and 22 'BCENE' and 27 'BCENI' options for the electron and ion energy equations respectively. Since this work builds on [78], the plasma boundary conditions chosen in these simulations are identical to those in [78]. These boundary conditions are as follows.

The total particle flux entering the computational domain through the core boundary is set to zero:

$$\frac{\sqrt{g}}{h_y}\Gamma_{a,y} = 0 \tag{3.21}$$

A radial decay length, $L_n = 0.03$m, is prescribed in these simulations for the density on the far SOL and PFR boundaries such that:

$$\frac{\sqrt{g}}{h_y}\Gamma_{a,y} = -\frac{\sqrt{g}}{h_y}\frac{1}{L_n}D_{n,a}n_a \tag{3.22}$$

On the divertor target boundaries, the particle flux entering the Debye sheath is set as follows:

$$\pm\frac{\sqrt{g}}{h_x}\Gamma_{a,x} = \pm 10^{20}\frac{\sqrt{g}}{h_x}\frac{\partial n_a}{\partial x} \tag{3.23}$$

This condition forces the density gradient at the target to be small for better numerical stability, the reader is referred to [127] for more details. The BCCON numbers for the different boundaries are summarised in table 2.

Boundary	BCCON
core	8
far SOL and PFR	9
divertor targets	3

Table 2: BCCON numbers for the B2.5 physical domain boundaries

The radial gradient of the parallel velocity is set to zero on the far SOL and PFR boundaries as well as the core boundary; parallel momentum, across these boundaries, shall not pass:

$$\frac{h_z\sqrt{g}}{h_y}\Gamma^m_{a,y} = 0 \tag{3.24}$$

A parallel velocity greater than the local sound speed of the species a (sheath condition), $v_{a,||} \geq c_{s,a}$, is imposed at the target boundaries for each species, where $c_{s,a}$ is given by:

$$c_{s,a} = \sqrt{\frac{e(Z_a T_e + T_i)}{m_a}} \tag{3.25}$$

The BCMOM numbers for the different boundaries are summarised in table 3.

Boundary	BCMOM
core	2
far SOL and PFR	2
divertor targets	3

Table 3: BCMOM numbers for the B2.5 physical domain boundaries

An energy flux associated with ions and electrons is imposed on the core boundary such that a total of 2.5MW enters the domain through the core in these simulations:

$$\frac{\sqrt{g}}{h_y}\tilde{q}_{e,y} = \frac{\sqrt{g}}{h_y}\tilde{q}_{i,y} = 1.25 \times 10^6 \text{ W} \tag{3.26}$$

A radial decay length for the ion and electron temperatures, $L_{T_i} = L_{T_e} = 0.03$m is prescribed on the far SOL and PFR boundaries in these simulations. The energy crossing the target boundaries is given by $Q_e = \delta_e \Gamma_e T_e$ for electrons and $Q_i = \delta_i T_i \sum_a \Gamma_a$ for ions where $\delta_e = 1.5$ and $\delta_i = 4$ are the specified sheath energy transmission coefficients. The BCENE and BCENI numbers for the different boundaries are summarised in table 4.

Boundary	BCENE	BCENI
core	8	8
far SOL and PFR	9	9
divertor targets	12	12

Table 4: BCENE and BCENI numbers for the B2.5 physical domain boundaries

3.1.2 The EIRENE neutral transport code

The EIRENE code is essentially a Monte-Carlo solver designed specifically to model the transport of kinetic neutrals in a plasma in realistic tokamak geometries, extensive details can be found in the EIRENE website [124]. As mentioned earlier, its main function is to provide the plasma energy, momentum and particle sources due to plasma-neutral interactions to B2.5.

There are three main types of neutral sources in EIRENE: point sources, surface sources and volume sources. Point sources are used to model gas puffing. They are points in the EIRENE simulation domain where a neutral flux is prescribed. Surface sources are due to the interaction of ions and neutrals with solid surfaces. This includes processes like recycling and sputtering. Volume sources are due to plasma-neutral interactions and volume recombination.

The interaction of ions and neutrals with solid surfaces is treated as follows. An ion or neutral incident on the wall can undergo one of three processes: fast reflection, thermal desorption or absorption. Absorption of an incident particle occurs through a user-defined probability for a given surface. This feature allows one to model 'wall pumping' and special surfaces can be defined to model turbo and/or cryopumps. The probability of a fast reflection event, and the velocity

and scattering angle of the reflected particle are sampled from the TRIM database [124]. Ions are neutralised in a fast reflection event and most of the incident kinetic energy is retained. In the case of thermal desorption, particles incident on the surface are released with a thermal energy corresponding to the surface temperature. Deuterium atoms and ions are desorbed as molecules, all other atoms and ions are desorbed as corresponding atoms. Plasma-surface interactions are also accompanied by physical and chemical sputtering of the wall material. Physical sputtering is treated in EIRENE using the modified Roth-Bohdansky formula for the sputtering yield [94]. Chemical sputtering is handled by prescribing a constant chemical sputtering yield.

Database and reaction code	Reaction	Reaction type
AMJUEL H.4,10 2.1.5	$D + e \rightarrow D^+ + 2e$	Ionisation
AMJUEL H.4,10 2.6A0	$C + e \rightarrow C^+ + 2e$	Ionisation
AMJUEL H.4,10 2.7A0	$N + e \rightarrow N^+ + 2e$	Ionisation
AMJUEL H.4 2.2.9	$D_2 + e \rightarrow D_2^+ + 2e$	Non-dissociative ionisation
AMJUEL H.4 2.2.5g	$D_2 + e \rightarrow 2D + e$	Dissociation
AMJUEL H.4 2.2.10	$D_2 + e \rightarrow D + D^+ + 2e$	Dissociative ionisation
AMJUEL H.4 2.2.11	$D_2^+ + e \rightarrow 2D^+ + 2e$	Dissociative ionisation
AMJUEL H.4 2.2.12	$D_2^+ + e \rightarrow D + D^+ + e$	Dissociative excitation
HYDHEL H.1,3 3.1.8	$D + D^+ \rightarrow D^+ + D$	Charge exchange
METHANE H.1,3 3.2	$D^+ + C \rightarrow C^+ + D$	Charge exchange
AMJUEL H.2 3.2.3	$D_2 + D^+ \rightarrow D + D_2^+$	Ion-conversion
AMJUEL H.0,1,3 0.3T	$D_2 + D^+ \rightarrow D_2 + D^+$	Elastic collision
AMJUEL H.4,8 2.2.14	$D_2^+ + e \rightarrow D + D$	Dissociative recombination
AMJUEL H.4,10 2.1.8	$D^+ + e \rightarrow D$	Radiative recombination
AMJUEL H.4,10 2.1.8	$D^+ + 2e \rightarrow D + e$	Three-body recombination

Table 5: EIRENE reactions

A large number of plasma-neutral interactions are active in detached divertor conditions which correspond to various volumetric neutral sources and sinks. EIRENE can handle a number of different plasma-neutral interactions through coupling to databases like AMJUEL, HYDHEL, METHANE and ADAS, see [106, 124] for more details. These databases contain the velocity averaged cross-sections for various reactions in the form of polynomial coefficients which are then interpolated for given plasma and neutral parameters. The EIRENE species handled in this work are D_2, D_2^+, D, C and N. The interactions between these species and the plasma background considered in this work are listed in table 5.

The basic functioning of EIRENE can be understood as follows. Each time EIRENE is called, it generates a set of neutrals called 'test particles', and tracks their movement through the plasma background which is provided by B2.5 as input. Test particles tracked by EIRENE are represented by a Markov chain which keeps track of their position, velocity and species type. The probability

that a test particle will undergo a certain type of neutral process, that it will travel a certain (straight line) distance before doing so, and that it will travel that distance at a certain velocity, is dictated by the cross section for that process, the background plasma provided by B2.5, and by the preceding process type. It can be noted here that the handling of D_2^+ is different from that of the other EIRENE species. This is an intermediate species in processes like molecule assisted ionisation (MAI) and molecule assisted recombination (MAR) which can make a non-negligible contribution to the divertor energy, momentum and particle balance in some cases [129, 130]. The creation rate of D_2^+ is very similar to its destruction rate [129]. Therefore, EIRENE does not evolve the trajectories of the molecular ions. Instead, as soon as a D_2^+ test particle is created, its position is kept fixed until it undergoes dissociation. In other words, the velocities of all molecular ions is zero in this model; the energy, momentum and particle balance associated with the creation and destruction of D_2^+ is stored in the EIRENE tallies.

Finally, the volume processes can be divided into electron-impact collisions and heavy particle collisions. Electron-impact processes include ionisation, dissociation and recombination whereas heavy particle collisions involve charge-exchange and elastic collisions. The collision rates of electron-impact processes depend on the electron temperature and density. They are assumed to be independent of the test particle velocity due to the relatively high electron thermal speed. Collision rates of heavy particle collisions depend on the ion temperature and the test particle velocity. Extensive details on how the energy and momentum exchange is calculated can be found in [131].

3.2 SOLPS-ITER simulations of the MAST-U Super-X geometry

As mentioned earlier, three parameter scans were performed for a fixed power entering the core boundary. Two of these were D_2 fuelling scans, in which D_2 molecules were injected from the inboard midplane, as shown in figure 21(a). In the first fuelling scan, all the neutral reactions listed in table 5 except nitrogen ionisation (AMJUEL H.4,10 2.7A0) are included. In the second fuelling scan, $D^+ - D_2$ elastic collisions (AMJUEL H.0,1,3 0.3T) were also excluded to test our hypothesis that this would lead to qualitative changes in the plasma solution. The fuelling rate is varied from $1 \times 10^{21} - 1.1 \times 10^{22}$ D_2 s^{-1} for the case with ion-molecule elastic collisions and from $1 \times 10^{21} - 8 \times 10^{21}$ D_2 s^{-1} for the case without. The third scan is the impurity seeding scan, for which an 'attached' case is chosen from the fuelling scan (which includes $D^+ - D_2$ elastic collisions, fuelling rate $= 2 \times 10^{21}$ D_2 s^{-1}) and nitrogen atoms (N) are injected into the divertor, close the entrance (up-down symmetric, as shown in figure 21(a)). The nitrogen seeding rate is varied from $5 \times 10^{19} - 1.1 \times 10^{21}$ N s^{-1}. All the neutral reactions listed in table 5 are included

in this scan. Intrinsic carbon is included as a sputtered impurity in all scans. As in [78], a 3% chemical sputtering yield is prescribed and the Roth-Bohdansky formula [94] is used to calculate the physical sputtering yield. As mentioned earlier, the plasma boundary conditions chosen in these simulations are identical to the ones presented in [78]. In all three scans, steady state solutions were not obtained when the gas injection rate was increased beyond the range shown here.

In all cases and for all plasma species, the cross-field heat diffusivity, $\chi_\perp = 10$ m^{2}s^{-2} and particle diffusivity, $D_\perp = 0.2$ m^{2}s^{-2} are used everywhere except in a small region inside the core where, to emulate H-mode temperature and density pedestals, we have used $\chi_\perp = 2$ m^{2}s^{-2} and $D_\perp = 0.02$ m^{2}s^{-2} (figure 21(c)). These diffusivities give radial SOL widths of $\lambda_q \approx 7.5$mm and $\lambda_{n_e} = \lambda_{T_e} \approx 16$mm, similar to values found in MAST H-mode experiments [132–134]. The radial resolution of our grid at the outboard mid-plane is such that we have 8 points between the separatrix and the first λ_q. The code was run with neutral-neutral collisions, impurity neutralisation and drifts turned off, and we do not solve for parallel currents in the SOL (no potential equation). The recycling coefficient is set to 1 in all simulations (no wall pumping).

Analysis presented in the work primarily concerns the regions highlighted in in figure 21(b), especially the SOL flux tubes or 'SOL rings' that deliver the peak heat and particle fluxes to the target when the fuelling rate $= 2 \times 10^{21}$ D_2 s^{-1} (the 'attached' case common to the fuelling and seeding scans).

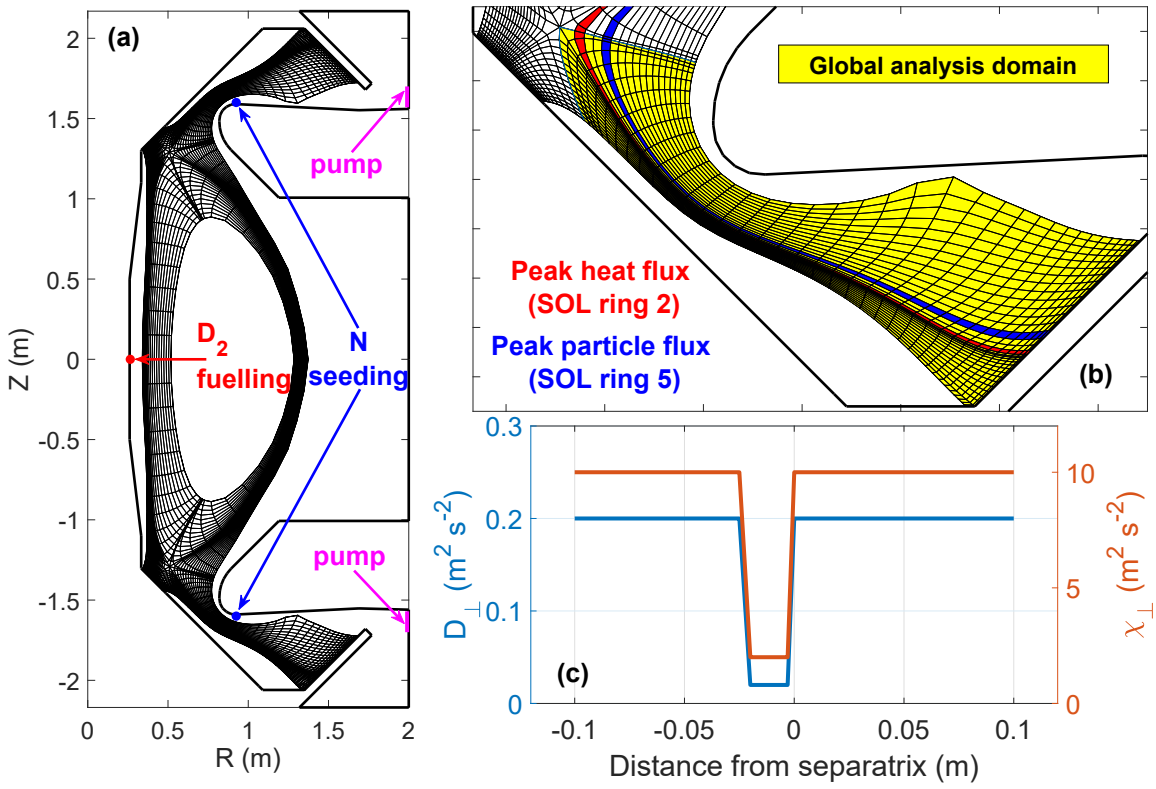

Figure 21: (a) Plasma domain (b) Global and flux tube analysis domains (c) Radial profiles of $\chi_\perp$ and $D_\perp$

As mentioned earlier, steady state solutions are obtained for each fuelling or seeding rate in each scan. Figure 22 shows the time variation of various quantities that are typically checked to evaluate whether a simulation has reached steady state - the time traces in this figure are from a nitrogen seeding case (N seeding rate $= 1.5 \times 10^{19}$ N s^{-1}). Colours are used to distinguish between each 48 hour (not CPU hours) SOLPS run using 48 cpu cores: this simulation, for example, was run for 48×8 hours (the colour of each time trace changes 7 times) on 48 cpu cores. It can be noted here that while EIRENE is MPI parallelised, B2.5 is a serial code. So using more than 48 cores did not significantly speed up these simulations because B2.5 was the bottleneck at the stage. Under these conditions, around 10,000-12,000 B2.5 time steps of size 10^{-5}s are taken in each 48 hour block.

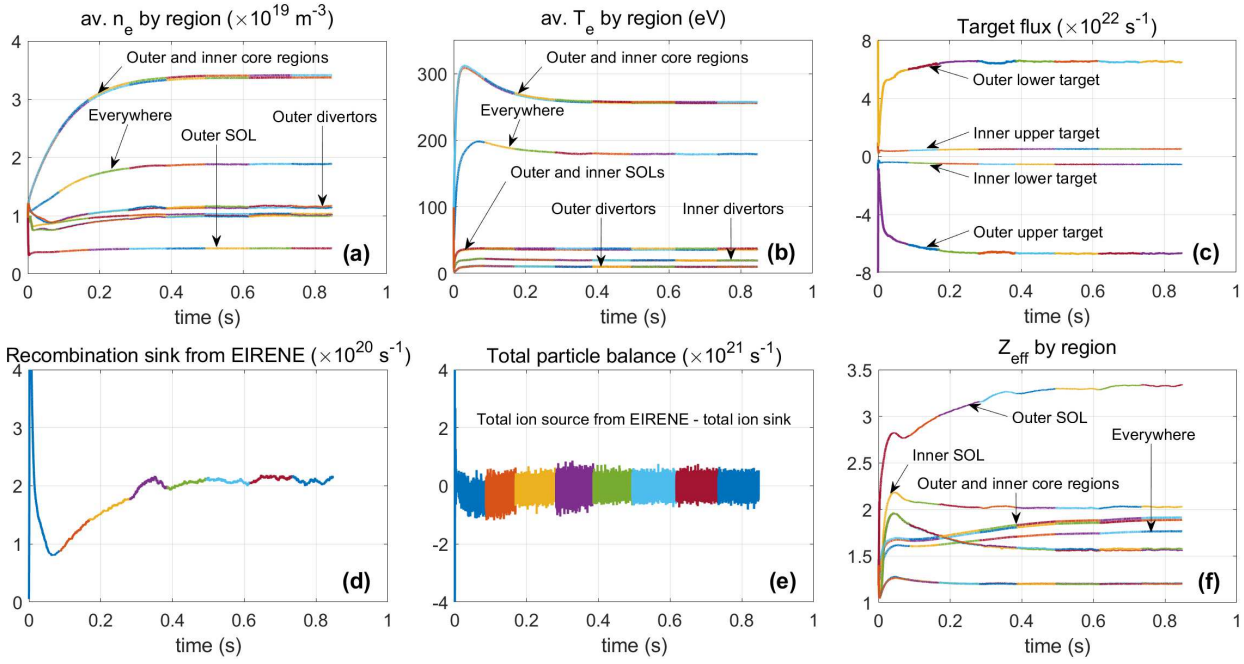

Figure 22: Time traces of various quantities that are typically checked to evaluate whether a simulation has reached steady-state

Figures 22(a) and 22(b) display the electron density (n_e) and temperature (T_e) averaged over various regions of the physical domain. The lack of time variation in these quantities is a reasonably good indication that major fluctuations in these fields have settled. However, the quantity that typically takes the longest to settle is the recombination sink from EIRENE, figure 22(d). Particle balance is therefore used to evaluate whether a simulation has reached steady state - simulations are assumed to have converged to a steady state solution when difference between the total ionisation source and the total volumetric recombination sink from EIRENE, figure 22(e), is on average zero for a few hundred milliseconds. The fluctuations in the time traces are basically the Monte-Carlo noise from EIRENE. Once a simulation has converged, it is run for another 1000 time steps and the output is averaged over this time period to exclude the Monte-Carlo noise from the analysis.

Chapter 4

Key observations

In this chapter, the basic observations like the evolution of the radial density and temperature profiles at the outboard midplane and target, and the corresponding profiles as a function of the parallel distance from the target are described first. This is followed by a description of the key observation associated with each of the two topics addressed in this thesis: (a) the slowing down of the detachment front in the region of high parallel gradients in the total magnetic field (b) the difference in recombination levels between the fuelling and seeding scans, and the impact of turning off ion-molecule elastic collisions in the fuelling scan. Parts of this chapter have been adapted from the following papers:

- O. Myatra et al. "The role of divertor magnetic geometry in detachment control in the MAST-U Super-X configuration" (soon to be submitted)
- O. Myatra et al. "Impact of ion-molecule elastic collisions on strongly detached MAST-U Super-X divertor conditions according to SOLPS-ITER" (soon to be submitted)

4.1 Introduction

We start our analyses by first making some basic observations of the profile evolution of key quantities. In this section, the evolution of the radial profiles of n_e and T_e, and the partile flux (Γ) and parallel heat flux ($q_{||}$) density are described. In all of the figures in section 4.1, the cyan trace represents the lowest gas injection rate, changing to magenta at the highest gas injection rate.

Figure 23 shows the evolution of the outboard midplane T_e and n_e profiles from each of the three scans for each fuelling or seeding rate. The n_e and T_e profiles behave as one would expect based on what is typically observed in experiments. In the fuelling scans, the density increases with increasing fuelling rate which is normally accompanied by a reduction in temperature. In the nitrogen seeding scan, the seeding rate at the start of the scan is more than an order of magnitude

lower than the fuelling rate at which the seeding scan is performed. The seeding rate is increased to about half this fuelling by the end of the scan. As result, there is little change in the outboard midplane n_e and T_e profiles, as one would expect.

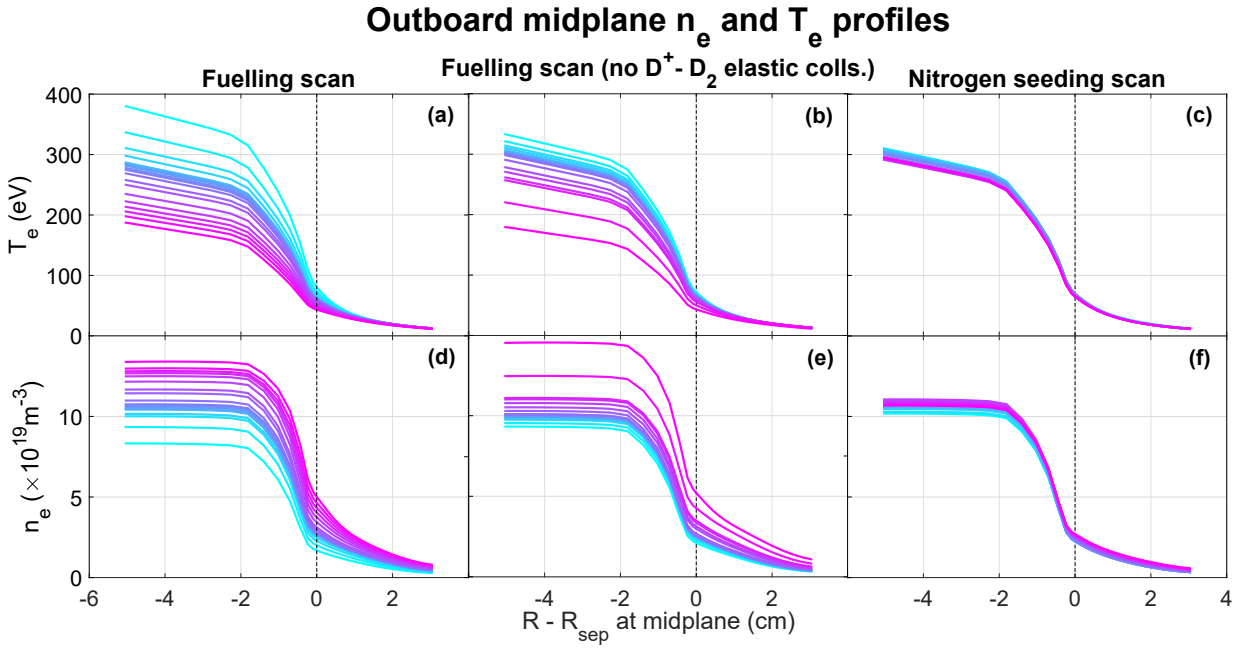

Figure 23: Outboard midplane n_e and T_e profiles

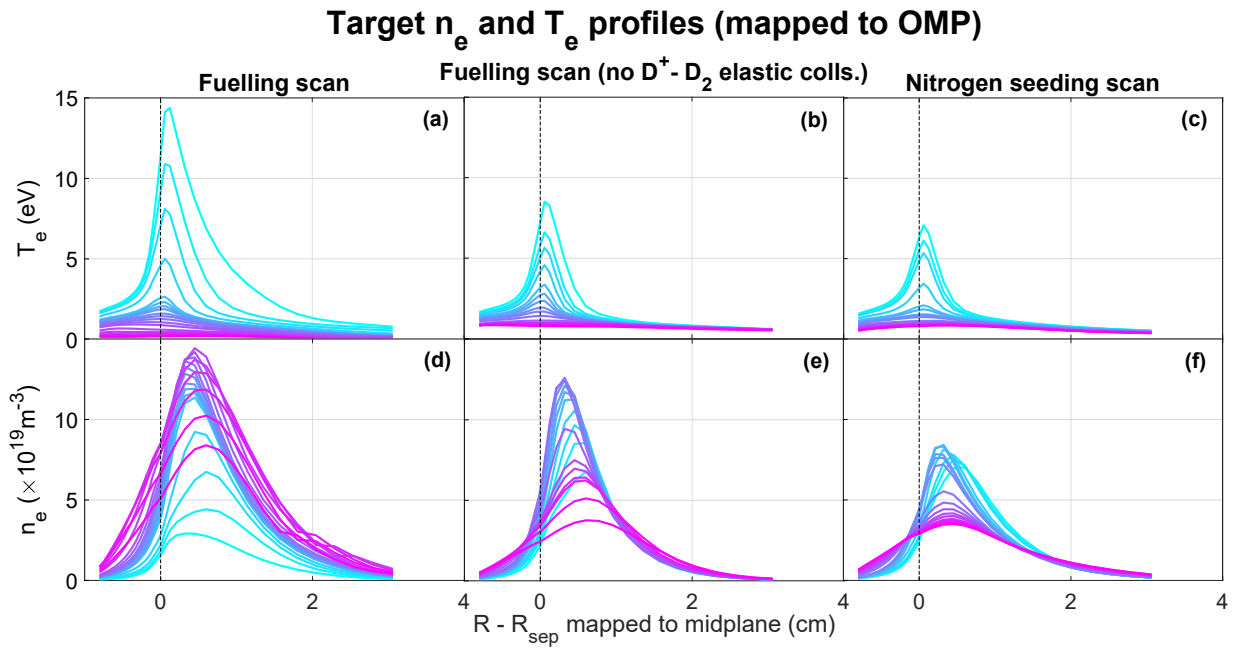

Figure 24: Target n_e and T_e profiles (lower outer target)

Figure 24 shows the T_e and n_e profile evolution at the outer lower target in each of the three scans for each fuelling or seeding rate. In general, the T_e profiles evolve as expected in all three scans: increasing upstream density leads to a reduction in the temperature at the target in the fuelling scans, and increasing nitrogen seeding rate would lead to increasing power losses in the

divertor and a reduction in temperature at the target. However, an important difference between figure 24(a), and figures 24(b) and 24(c) is that lower temperatures are achieved in figure 24(a). While this difference appears small, it leads to significant differences in volume recombination levels. The n_e profiles evolve as expected in the fuelling scans, increasing initially with increasing fuelling rate and then reducing ('rolling over') shortly after detachment. However, in the seeding scan, there is only a small initial increase in density, followed by a significant reduction.

Figure 24 shows profiles of the electron flux (which is equal to the ion flux since parallel currents are not included), Γ, and parallel heat flux, $q_{||}$, at the outer lower target in each of the three scans for each fuelling or seeding rate. The Γ profiles evolve as expected in the fuelling scans, increasing initially with increasing fuelling rate and then rolling over. In the seeding scan, there is not much of an increase in Γ, which mainly just drops through most of the scan. However, profiles at the end of the three scans scans are mostly similar, with the peak particle flux in figure 25(a) only being slightly lower than that in the other two scans. As in the case of the T_e profiles, the parallel heat flux generally evolves as expected: consistently dropping for increasing fuelling or seeding rate, but the $q_{||}$ at the end of the fuelling scan which includes $D^+ - D_2$ elastic collisions is lower compared to that in the other two scans.

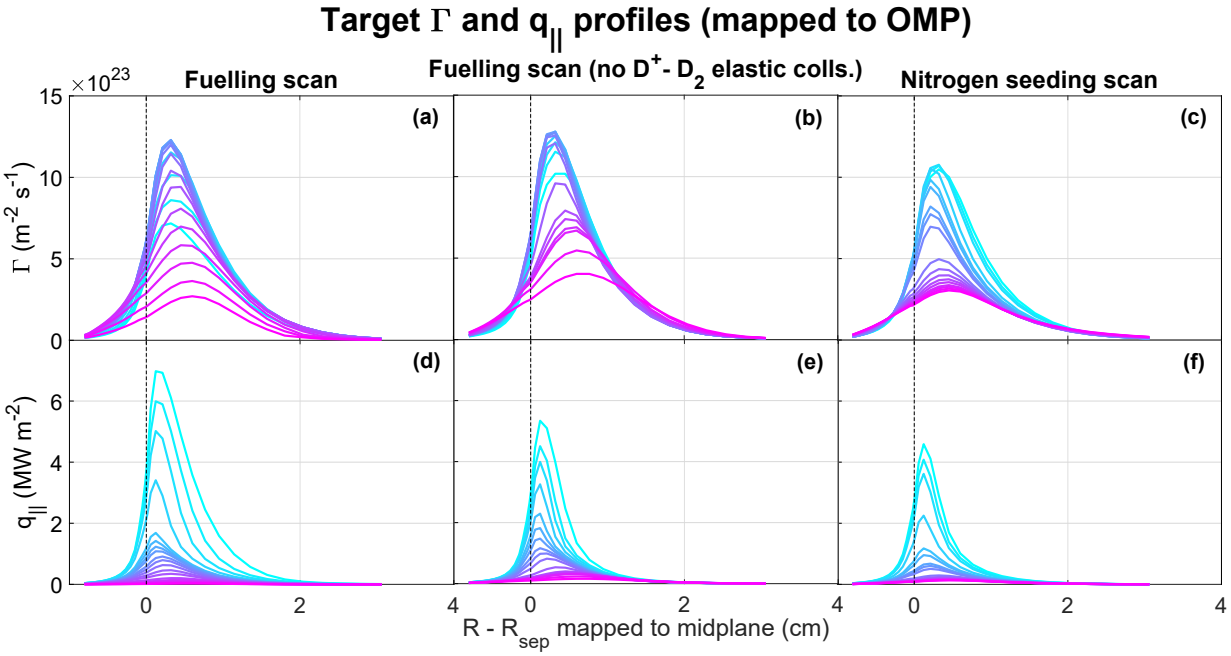

Figure 25: Particle flux (Γ) and parallel heat flux ($q_{||}$) on lower outer target

Figure 26 shows T_e and n_e profiles between the X-point and the outer lower target as a function of the parallel distance from the target in SOL ring 2, the red flux tube highlighted in figure 21(b). While the evolution of the T_e profiles is qualitatively similar in the three scans, there are qualitative differences between the evolution of the n_e profile in figure 26(d), and figures 26(e) and 26(f). In the seeding scan and the fuelling which does not include $D^+ - D_2$ elastic collisions, the n_e profiles

are initially peaked at the target, but they flatten out at high fuelling/seeding rates. In the fuelling scan which includes $D^+ - D_2$ elastic collisions, the n_e profiles remain peaked at the target.

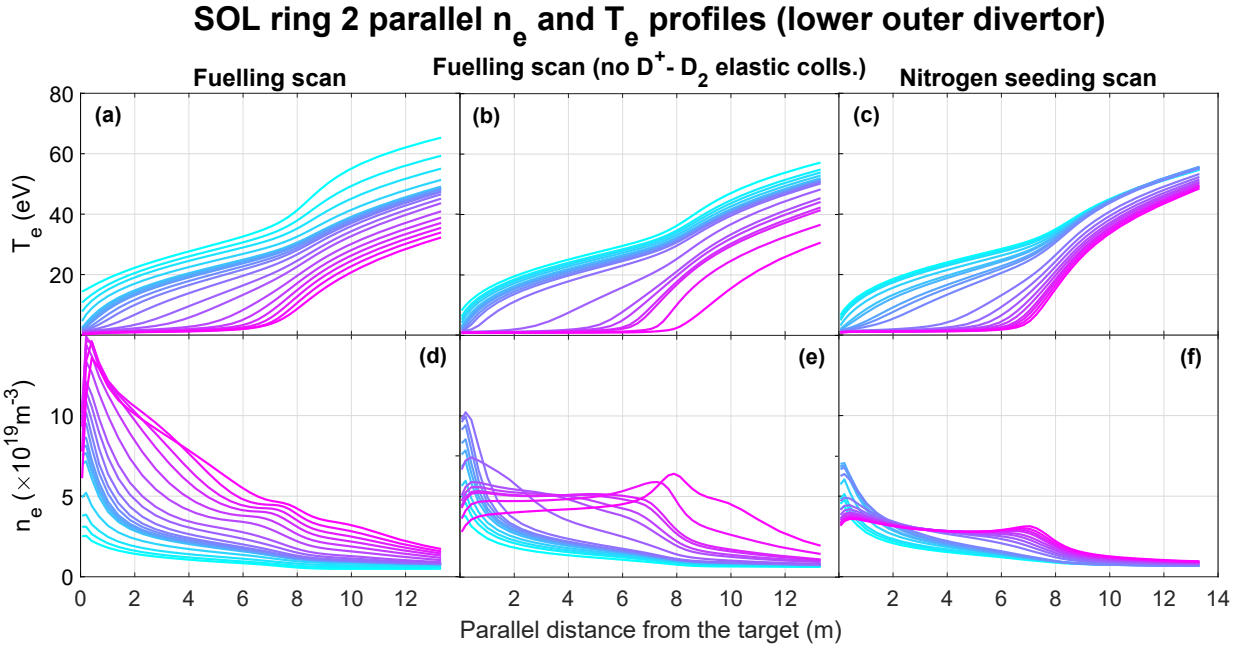

Figure 26: SOL ring 2 parallel profiles (lower X-point to outer target)

4.2 Drop in sensitivity of the detachment front location to controls in the region of high parallel magnetic field gradients

Detachment is typically accompanied by a variety of changes in the divertor plasma characteristics. In particular, there are plasma pressure losses due to volumetric momentum transfer from ions to neutrals at low ($T_e \leq 5$eV) temperatures [135]. Thus in experiments, a target electron temperature of ≈ 5eV is normally utilized as the threshold for detachment. We also use it as a marker to track the location of the front edge of the detached region. The $T_e = 5$eV point can be tracked directly using the SOLPS output.

Detachment also leads to movement of other measurable divertor characteristics. For example, various radiation profile peaks (hydrogenic, impurity or total) move towards the X-point as the extent of detachment from the target increases. Researchers have tracked the location of the point where the C-III radiation drops to $1/e$ or 50% of the maximum towards the target [79, 110, 136], using that location as a rough proxy of the detached region's front edge (detachment location or front). In this work, we have chosen to also track the locations of the peak power losses due to hydrogenic radiation (excitation plus ionization, P_H) and due to total impurity radiation (due to carbon in the fuelling scan, P_C; and both nitrogen and carbon in the seeding scan, P_{C+N}). In addition, we track the locations at which these power losses drop to 50% of their maximum

value along a flux tube on the target side of the peak. It should be noted here that in reality the detachment front can be a rather nebulous thing and therefore difficult to strictly define. This is the reason why we choose to follow several definitions to see if they behave similarly.

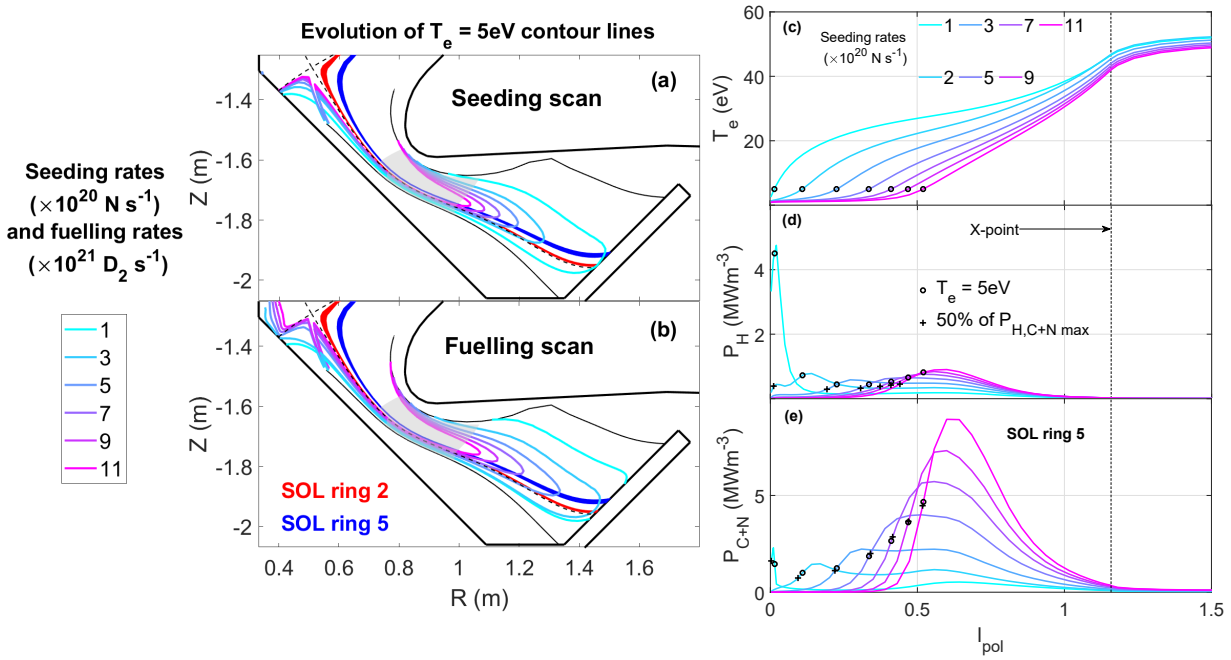

Figure 27: (a and b) Evolution of $T_e = 5$eV contour lines during seeding and fuelling scans. The region in which the parallel gradient in B is greater than 50% of the maximum in the divertor is shaded in grey; (c, d and e): Profiles of T_e, P_H and P_{C+N} are shown as a function of l_{pol} for the seeding scan to detachment. In addition, markers are added to denote the $T_e = 5$eV points (circles), as well as the location where P_H and P_{C+N} drop to 50% of maximum (crosses). Also highlighted are the model grid flux surfaces corresponding to the peak heat flux (red) and peak particle flux (blue) as shown in Fig. 21

In general, we find that the poloidal movement from target towards the X-point of the various markers tracked as a function of D_2 fuelling or N seeding rate slows down as their location approaches a region of high parallel gradient in B which is also near the baffle or divertor entrance. The evolution of the $T_e = 5$eV contours in the poloidal plane is shown in figures 27(a) and (b) for each detachment scan. The region in which the parallel gradient in B is greater than 50% of the maximum parallel gradient found across the *entire* divertor is shaded in grey. It can be seen that as the 5eV contour approaches the region of high parallel gradients in B, the poloidal movement in the 2D plane becomes smaller for the same increment in seeding or fuelling rate; the sensitivity of the $T_e = 5$ eV location to changes in the injection rate drops in both scans. It should be noted that the definition used here to outline the grey region only serves as a rough indicator of where in the poloidal plane the parallel gradient B is relatively strong ($\geq 50\%$ of the maximum), and to illustrate the reduction in sensitivity of the 5eV boundary to injection rates as it approaches this region. The difference between 'high' and 'low' parallel gradient in B is discussed in further detail in section 5.1.

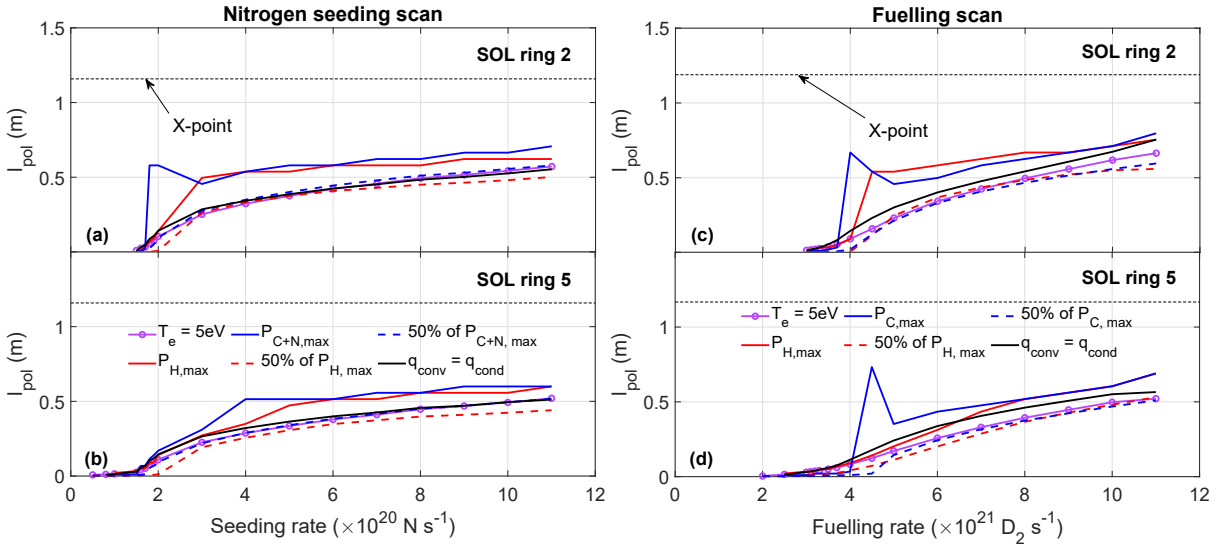

Figure 28: The movement of the detachment front in poloidal plane, l_{pol}, for nitrogen seeding scan (a and b) as well as the D2 fuelling scan of the upstream density (c and d): 6 different 'markers' corresponding to the detachment front location are shown. See Figure 27(c)-(e) for an illustration of the location of the various markers on the various profiles. The above results are shown for both the high heat flux flux tube (ring 2) and the high particle flux flux tube (ring 5).

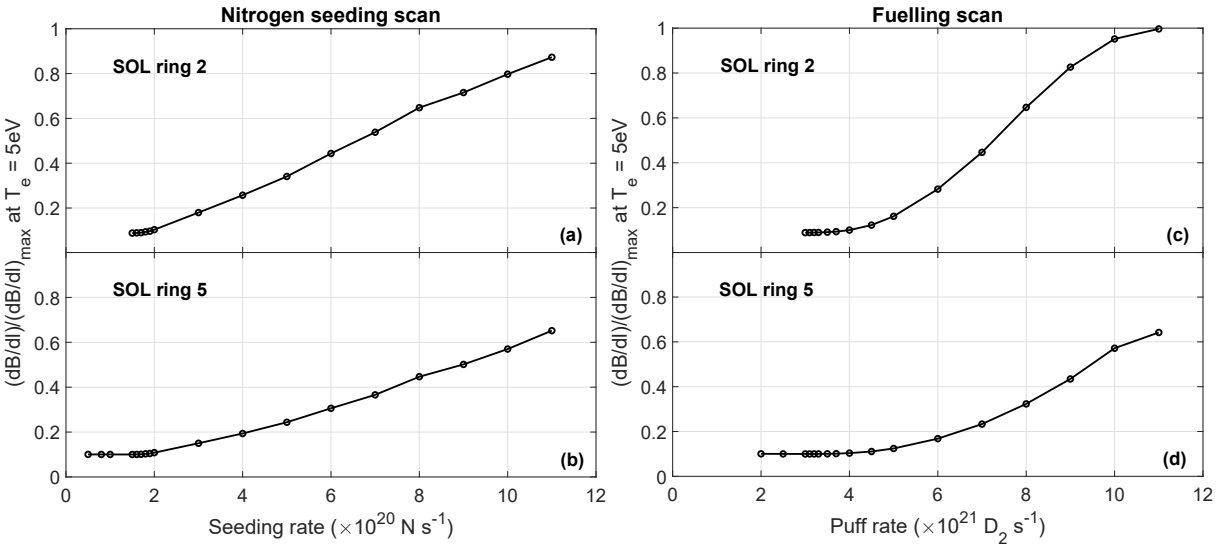

Figure 29: The parallel gradient in B, dB/dl, at the locations of the 5eV point in SOL rings 2 and 5 as a function of N seeding and D_2 fuelling rate (normalised to the maximum value of dB/dl in those flux tubes).

The general reduction in sensitivity of the various potential detachment location markers introduced above to the injection rates is shown more clearly in figure 28 which displays their l_{pol} location as a function of seeding and fuelling rate for the SOL rings 2 and 5. In general, the 5eV marker leaves the target shortly after the radiation peaks leave the near target region ($l_{pol} > 0$). The 5eV markers are only a short distance downstream in l_{pol} from the radiation peaks for most injection rates. In both scans, locations of the 50% of $P_{H,max}$ and $P_{C,max}/P_{C+N,max}$ points leave the target shortly after the 5eV point, but quickly 'catch up' and either coincide with the 5eV

point or are very close to it throughout most of the scan.

One of the changes in the divertor that is accompanied by the low temperatures is the significant reduction in the heat transported along the field by conduction. We find that the relative contribution of conduction to the parallel heat flux decreases in the detached region along a field line towards the target; in the Super-X case studied here, convection is the dominant heat transport mechanism in the detached region. Based on this, we also track the point where heat convection, q_{conv}, is equal to heat conduction, q_{cond}, shown in black in figure 28. It is interesting to see that this point also typically lies close to the $T_e = 5$eV and 50% points on the radiation profiles throughout both seeding and fuelling scans to detachment. This is similar to experimental observations in DIII-D where the parallel heat flux was transported by convection was found to start dominating as T_e dropped below ~10eV [137]. In the DLS model, only the region between the midplane and the detachment front is treated, and convection is assumed to be negligible as typically done in simple SOL models. Further studies are needed, but for computational studies which have access to significantly more information on the plasma parameters compared to experiment, this additional detachment front marker where $q_{conv} = q_{cond}$ could serve as a physics based boundary marking the start of the detached region.

The reader will note that the markers for the radiation peaks can abruptly move to larger l_{pol} for small changes in seeding or fuelling rates. This can be traced back to the profiles of radiation in figures 27(d) and (e): At low fuelling/seeding rates there can be two peaks in the profiles of P_{C+N} and P_H, one near the target, and the other upstream at $l_{pol} \approx 0.5 - 0.7$m, in the region of high parallel gradients in B. As the injection rate is increased, the peak near the target drops and the peak upstream grows and thus the location of the higher peak changes abruptly from near the target to further towards the X-point. The peak near the target drops because the temperature there is dropping and both impurity and hydrogenic sources of radiation drop at detachment temperatures ($T_e \leq 5$eV).

Based on the above discussions, the following markers are all useful for tracking the detachment front: the $T_e = 5$eV point, the 50% point on the P_H and impurity radiation profiles (on the target side of the peak) and the point where $q_{conv} = q_{cond}$. However, for simplicity, we consider the flux tube to be 'detached' when the 5eV marker leaves the target when studying the movement of the detachment front.

As mentioned earlier, the sensitivity of the 5eV boundary in figure 27 drops in a region of high parallel gradients in B. This is demonstrated in figure 29 which shows the parallel gradient in B, dB/dl, (where l is the parallel distance from the target) at each of the $T_e = 5$eV locations in SOL rings 2 and 5 shown in figure 28, normalised to the maximum value of dB/dl in those flux tubes, as a function of seeding/fuelling rate. The fact that the movement of the 5eV point in

l_{pol} slows down as it moves through increasing dB/dl can be seen when studying figures 28 and 29 together: in the seeding scan (ring 2), the 5eV point starts moving away from the target at a seeding rate $\approx 1.5 \times 10^{20}$ N s^{-1}, and reaches $l_{pol} \approx 0.25$m (fig. 28) as the seeding rate is increased to 3×10^{20} N s^{-1}. Across this distance, dB/dl (fig. 29) only increases from ≈10% of the maximum to ≈15-20%. However, to move the 5eV point another 0.25m upstream to $l_{pol} \approx 0.5$m 28), the seeding rate has to be increased from 3×10^{20} N s^{-1} to 11×10^{20} N s^{-1}; and across this distance, dB/dl (fig. 29) increases significantly from ≈15-20% of the maximum to ≈65-85%. A similar trend is also observed in the fuelling scan.

In summary, a reduction in the sensitivity of the plasma profiles to impurity seeding and main ion fuelling rates is observed as increasing power loss occurs in a region of high parallel gradients in the magnetic field (which translates into regions of high $q_{||}$). We return to this discussion in chapter 5, in which the movement of these points is studied as a function of 'physics' control parameters described in the DLS model in order to compare model predictions for MAST-U to the simulation results. In the next and final part of this chapter, we describe the key observations concerning the comparison of strongly detached solutions obtained in each scan.

4.3 Differences in recombination levels and the impact of turning off ion-molecule elastic collisions

As mentioned previously, an important quantity used in experimental detachment studies is the plasma flux incident on the divertor plate, the evolution of which is typically used to identify detached divertor conditions. The target flux rises in the high recycling regime, the rise rate slowing as the upstream density continues to increase. At some point, the target flux rolls over and then decreases for increasing upstream density – the most clear sign of detachment. We have also used this measure in analysis of the fuelling and seeding scans included in this study – in particular the study of the target flux drop after detachment. In this part of our discussion, we will describe the key observation regarding the processes involved in increasing or reducing the plasma flux reaching the divertor in each scan.

The general development of the simulated radially integrated electron flux to the outer lower divertor target, $\Gamma_{t,tot}$, from high-recycling through to their respective detached states is shown in figure 30 for the three scans - since SOL currents are not included in these simulations, the electron and ion fluxes to the target are equal. Each of the fuelling scans evidence a rise in the target flux before a drop. A reduction in $\Gamma_{t,tot}$ can be seen for fuelling rates greater than 3×10^{21} D_2 s^{-1} in figure 30(a) and greater than 2×10^{21} D_2 s^{-1} in figure 30(b). The seeding scan, figure 30(c), is carried out at fuelling rate 2×10^{21} D_2 s^{-1} (light blue diamond in figure 30(a)). In contrast

to the fuelling scans, only a reduction in $\Gamma_{t,tot}$ is observed in the seeding scan, similar to TCV experiments [48].

In order to properly understand which process or processes lead to the target current reduction, we have analyzed the various electron sources and sinks integrated over the entire region between the outer lower divertor entrance and the target (highlighted in yellow in figure 21(b)). Through particle balance, $\Gamma_{t,tot}$ is given by equation 4.1:

$$\Gamma_{t,tot} = \Gamma_{u,tot} + S_{iz,tot} + S_{rec,tot} + \Gamma_W \tag{4.1}$$

Here $S_{iz,tot}$ and $S_{rec,tot}$ are the volume integrated electron sources due to ionisation and recombination respectively (when sources are negative they correspond to sinks). Γ_W is the poloidally integrated electron flux lost from the computational domain due to cross flux surface transport (the sign convention used for sources is also adopted for fluxes: cross-field transport out of the domain is a negative flux) and $\Gamma_{u,tot}$ is the total upstream electron flux entering the domain along the flux surfaces. Contributions to $\Gamma_{t,tot}$ from the RHS terms of equation 4.1 are also shown in figure 30 for each scan. It can be seen be seen that $\Gamma_{u,tot}$ and Γ_W are negligible throughout each scan and that $S_{iz,tot}$ makes the dominant contrbution to $\Gamma_{t,tot}$.

The key difference between the various scans is the strong contribution from $S_{rec,tot}$ at high D_2 fuelling rates in the fuelling scan shown in figure 30(a), which is always negligible in figures 30(b) and 30(c). The focus of this work is to explain how ion-molecule elastic collisions provide access to strongly recombining conditions in the fuelling scan, and the reasons why we see recombination playing a negligible role in the seeding scan.

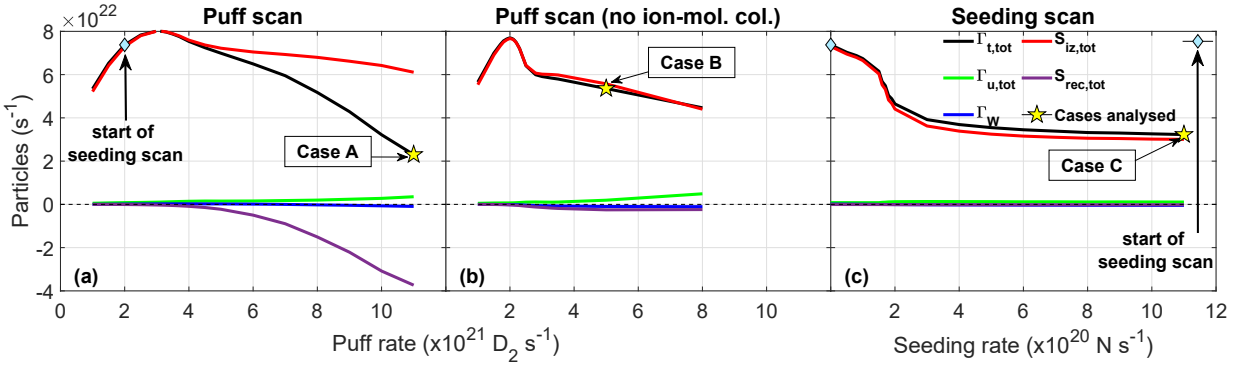

Figure 30: Global particle balance for the yellow region shown in figure 21(b) for each scan. The nitrogen seeding scan is carried out at a fixed fuelling rate 2×10^{21} D_2 s^{-1}, marked with diamonds. The cases marked with stars are chosen for further analysis to understand the reason for the differences in recombination levels.

At any given fuelling or seeding rate a varying fraction of the power flowing into the divertor region from upstream is dissipated between the X-point and the divertor target over a poloidally-localised region through a variety of processes. That region is sometimes called a 'thermal front'

as the temperature drops quickly through it due to the removal of power [138]. In our simulations, the cold end of the thermal front region stays at the target while $\Gamma_{t,tot}$ increases for increasing fuelling rate (attached plasma) and for seeding rates less than 1.5×10^{20} N s^{-1}. The roll-over in $\Gamma_{t,tot}$ in the fuelling cases and the sharp reduction in $\Gamma_{t,tot}$ in the seeding case occur as the thermal front (along with its cold end) moves away from the target and towards the X-point. Once the thermal front leaves the target, a low plasma pressure and temperature region exists between the target and the cold end of the thermal front - we call this region the 'detached' region. As a result of the low temperature, the dominant heat transport mechanism in this region is convection (as opposed to parallel conduction) in the cases we modelled.

While the 5eV point is treated as the start of the detached region (for convenience) in the study concerning detachment control, the region across which convection is the dominant heat transport mechanism is adopted as the detached region in this study where the detached solutions are compared in detail - the point in the thermal front where the conducted heat becomes equal to the convected heat is treated as the start of the detached region for this part. The reason for this discrepancy in the way the detached region is defined in the two parts of this thesis can be partially traced to how the work presented in this thesis evolved during its course, apologies for the confusion induced by this choice.

To understand the reason why recombination is significantly higher in figure 30(a), we take the case with the highest recombination, case A (highlighted with a yellow star in figure 30), and compare it with cases from the other two scans in which the extent of the detached region is similar, cases B and C. The region in the divertor where parallel heat convection is greater than conduction is shown in blue in figure 31 for the three cases chosen for further analysis. It can be seen that the extent of the detached region in the poloidal plane are similar across the three cases. We return to this discussion in chapter 6, in which we analyse these cases in further detail and explore the reasons for the observed differences between the two routes to detachment.

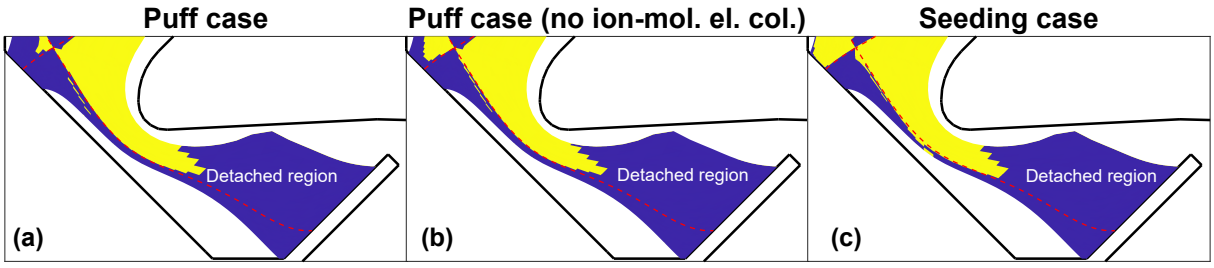

Figure 31: Extent of the outer lower detached region in the cases chosen for analysis (marked with stars in figure 30). Regions where parallel heat convection is greater than parallel conduction are marked blue and defined as the 'detached' region in this work. It can be seen that the extent of the detached region is similar amongst the cases chosen for analysis.

Chapter 5

The role of divertor magnetic geometry in detachment control

The key observation associated with this chapter is described in section 4.2. As a reminder, a number of different proxies or markers for the detachment location were identified in the simulations. The movement of these markers was tracked as a function of the D_2 fuelling and N seeding rates. In both the fuelling and seeding scans, the sensitivity of the location of these markers to the fuelling or seeding rates was observed to reduce as they approached a region high parallel gradients in the total magnetic field - already consistent with the DLS model predictions.

In this chapter, we compare the predictions of the DLS model for detachment location with simulation results. In the next section, modifications to the DLS model for application to the MAST-U Super-X geometry is described. The method of obtaining the 'physics' control variables of the DLS model from the SOLPS data is described in section 5.2. Model predictions and simulation results are compared in section 5.3. Possible reasons for discrepancies between the model predictions and simulation results are discussed in section 5.4.4, and conclusions are summarised in section 5.5. This chapter has been adapted from the following paper:

- O. Myatra et al. "The role of divertor magnetic geometry in detachment control in the MAST-U Super-X configuration" (soon to be submitted)

5.1 The modifications of the DLS model to apply to SOLPS data

Our modification of the DLS model for this study is mandated by the need to apply the model to a situation where the variation of B along a field line is not linear; certainly true for the Super-X divertor. We follow the development of the DLS model for application to a single flux tube: power balance is used to predict the thermal/detachment front location as a function of n_u which is taken

to be the electron density at the outboard midplane, the impurity fraction f_I which is assumed to be constant in the flux tube and P_{div} which is the power passing through the flux tube at the X-point position.

The front moves along a mathematically convenient parallel co-ordinate z defined such that $z = 0$ at the target and $z = L$ at the outboard midplane. The length z is actually the volume of the flux tube between the target and z normalised by a reference area $\propto (1/B_\times$, $B_\times$ is the magnetic field strength at the X-point) and it is related to the actual parallel distance from the target (l) and poloidal distance (l_{pol}) as:

$$dz = \frac{B_\times}{B} dl = \frac{B_\times}{B_{pol}} dl_{pol} \tag{5.1}$$

In other words, the element dz is essentially the actual elemental parallel distance dl scaled by the total flux expansion at that point in the divertor. As a result, the regions close to the target (where the total flux expansion is high) are elongated in z space compared to l space. This is illustrated in figures 32(a) and 32(b) which shows a comparison of z and l, and $B(z)$ and $B(l)$ for SOL ring 2.

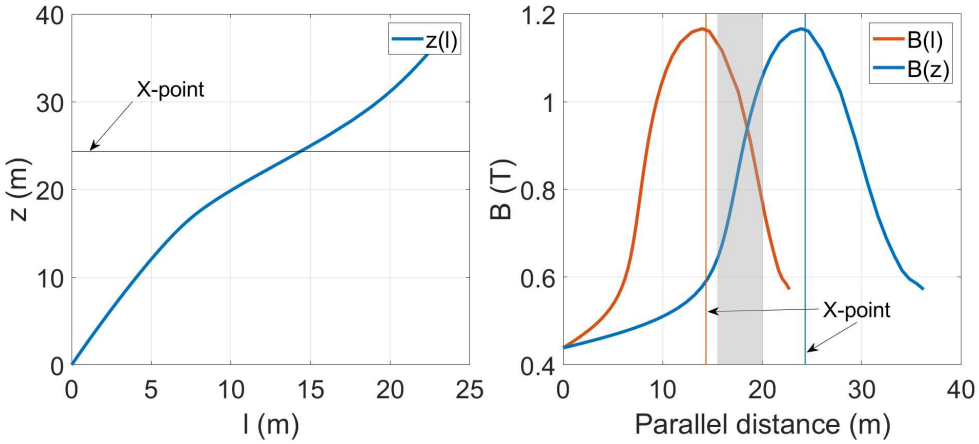

Figure 32: a) The parallel coordinate z as a function of the actual parallel distance from the target l, given for SOL ring 2. For this flux tube, B field between target and outboard midplane is shown in figure (b) as a function of both l and z.

It is useful at this stage to distinguish between the region of 'high' parallel gradients in B and the region of 'low' parallel gradients for a *flux tube*. Figure 32(b) shows the parallel profiles of B in z and l space. It can be seen that the space between the X-point and target can be roughly separated into two distinct regions, one in which the gradient is relatively low and one where it is relatively high, even though the transition between the low gradient region and the high gradient region is smooth. For simplicity, for the rest of this thesis, we define the region of 'high' gradients in a flux tube as the region where dB/dz is greater than 50% of the maximum between the X-point

and the target. This has been illustrated in figure 32(b) for $B(z)$ where this region is shaded in grey. Although this definition is arbitrary, it serves as a useful indicator of where in z space dB/dz is relatively high for when we compare the DLS model predictions with SOLPS results.

In the DLS model, the thermal front (within which the radiative power loss occurs) is assumed to be thin/small compared to $z_\times$ (the distance between the X-point and target in z); that assumption simplifies the calculation of the radiative loss as well as allowing the thermal front (and detachment location) to move a significant amount from $z = 0$ to $z = z_\times$.

The key difference between the DLS model and its application in this study is the treatment of the divertor magnetic field profile. The analytic DLS model assumes that B is a linear function of z. This simplifies the analytic calculations of both the radiation losses and the effect of detachment movement on the upstream temperature.

In the following we have generalized the DLS equations (in particular, equation 27 of [76]) to allow for any divertor magnetic field profile. The detachment front location z_f and the control parameters are related as follows:

$$\frac{n_u\sqrt{f_I}}{P_{div}^{5/7}} = \frac{1}{U}\frac{B(z_f)}{B_\times^{3/7}} \times \left[\int_{z_f}^{z_\times} B^2(z)dz + \int_{z_\times}^{L} \frac{B^2(z)(L-z)}{L-z_\times}dz\right]^{-2/7} \tag{5.2}$$

where U is assumed to be a constant related to the Lengyel integral [76, 138–143]:

$$U = 7^{2/7}(2\kappa_0)^{3/14}\sqrt{\int T^{1/2}Q(T)\mathrm{d}T} \tag{5.3}$$

where $Q(T)$ is the radiative loss parameter or 'cooling function' [144] and κ_0 is the electron heat conductivity coefficient.

There are other simplifications made in the analytic DLS model which make it difficult to properly compare DLS model predictions to SOLPS results. Two model assumptions which do not hold in the SOLPS case are a) all the power entering the divertor is dissipated through radiation due to a single impurity species; and b) that impurity has a *constant concentration* ($f_I = n_z/n_e$) in the flux tube. In SOLPS simulations, there are multiple radiating species (multiple impurities as well as hydrogen), and their concentrations are not constant along z. There are power loss mechanisms beyond radiation as well. To compare DLS model predictions with the MAST-U simulations presented here, we have utilized an 'effective power loss species concentration', f_{eff}, which is defined (see section 5.2) to account for power losses from multiple impurity species and also the main ion species; f_{eff} is used in place of the impurity concentration f_I. We note that while the gas injection rates are the only parameters varied in the simulations, all three control parameters of the model are affected. Because of this we use a 'lumped' physics control parameter,

C_l, which will include simultaneous change in n_u, f_{eff} and P_{div} as the gas injection rate changes:

$$C_l(z_f) \equiv \frac{n_u \sqrt{f_{eff}}}{P_{div}^{5/7}} \tag{5.4}$$

In our comparison of the DLS model to the SOLPS calculations of detachment location movement, we are interested in comparing the DLS predictions of the *relative* changes in the control parameters. This is consistent with studies of other models using the Lengyel formulation [139] where the prediction of the divertor detachment threshold in f_I was over-predicted by factors ≥ 4 [145, 146]. However, the relative trade-off between control variables in achieving detachment appeared to be accurate.

As described above, even though the scans to achieve detachment are achieved through just varying the fuelling or seeding rates, the other two control variables are affected and they vary as well. This is accounted for by the lumped control parameter introduced above. However, since we are interested in the relative changes in controls following detachment onset, we define a normalised lumped control parameter, $C_{l,norm}$, and take $C_l(z_f = 0)$ to be the value of C_l at the injection rate at which the 5eV point is on the verge of detaching from the target:

$$C_{l,norm}(z_f) \equiv \frac{C_l(z_f > 0)}{C_l(z_f = 0)} = \frac{B_f \times \left[\int_{z_f}^{z_\times} B^2(z)dz + \int_{z_\times}^{L} \frac{B^2(z)(L-z)}{L-z_\times} dz\right]^{-2/7}}{B_t \times \left[\int_{z_t}^{z_\times} B^2(z)dz + \int_{z_\times}^{L} \frac{B^2(z)(L-z)}{L-z_\times} dz\right]^{-2/7}} \tag{5.5}$$

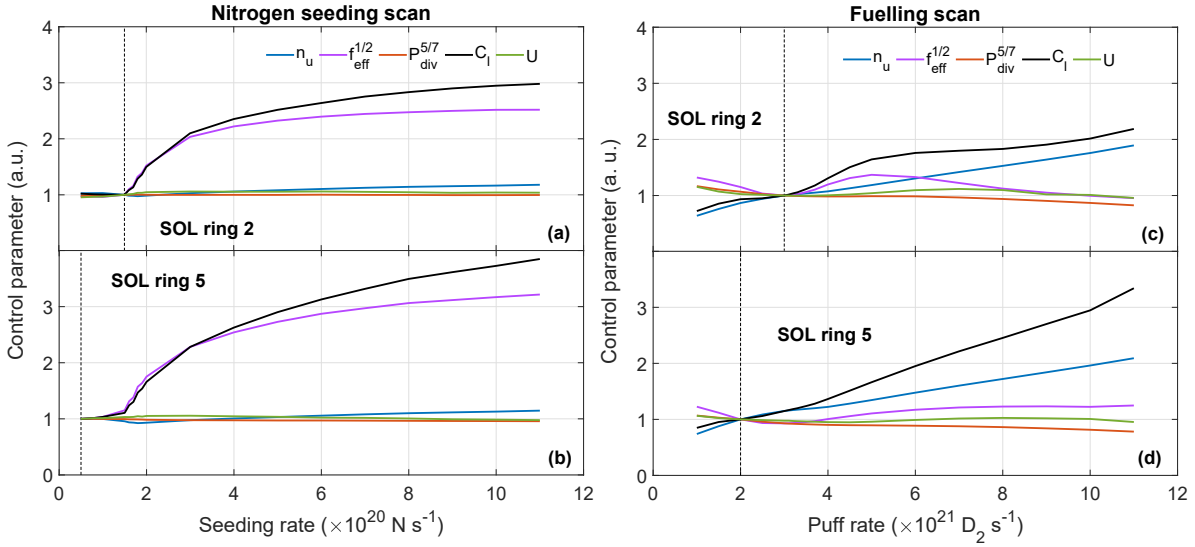

Figure 33: Variation in the lumped control parameter, $C_{l,norm}$ and its components (all normalised to their value when $T_e = 5$eV leaves the target) shown as a function of seeding and fuelling rates for different scans as well as the 2 analysis rings, shown in Fig. 21. The seeding/fuelling rates at which the 5eV point leaves the target are marked with vertical lines.

Changes in $C_{l,norm}$ and its components as a function of fuelling/seeding rate, relative to their

value when the 5eV point detaches, are shown in figure 33. In the seeding scan, changes in C_l are mainly driven by f_{eff} and there is little change in all other quantities. In the fuelling scan, while changes in C_l are driven primarily by n_u, changes in f_{eff} are also significant. The assumed 'constant' U is also shown, and indeed there is little change in this quantity in both scans. Exactly how f_{eff} and U are defined and calculated from the SOLPS output is described in further detail in section 5.2. That is followed by a comparison of the modified DLS model predictions for MAST-U to the simulation results.

5.2 Extracting SOLPS equivalents of DLS model variables

As mentioned earlier, given that the impurity and deuteron density fractions vary over the flux tube and the DLS model requires a constant fraction, we have developed f_{eff}, a constant along a flux tube. f_{eff} is defined to account for power losses from multiple species (impurity and hydrogenic), each with concentrations varying along the SOL. f_{eff} is defined using the same framework that the DLS analytical model uses to relate impurity levels and the corresponding power loss. To arrive at the expression for f_{eff} used in our analysis, we start from the DLS definition of a constant impurity (nitrogen) fraction in a flux tube, f_N (f_I is used in this thesis if the impurity is not specified), generalize that so as to be applicable to a varying impurity concentration and then finally, to include the effect of power losses from hydrogen and carbon.

The DLS model defined the nitrogen concentration (f_N) as:

$$f_N = \frac{\sum_{i=0}^{Z+} n_{N^i}}{n_e} = n_N/n_e \tag{5.6}$$

In the DLS model, a mathematical function which depends on the temperature, $Q(T)$, is defined (equation 3 in [76]) to relate f_N and the corresponding radiation power density, P_N. This function approximates the nitrogen radiation loss parameter [138]. The resulting radiative power loss density is then

$$n_e n_N Q(T) = n_e^2 f_N Q(T) = P_N \ [\mathrm{Wm}^{-3}] \tag{5.7}$$

However, to compare SOLPS results to the generalised analytical model, we calculate the radiative loss parameter for nitrogen, Q_N, directly from the SOLPS output:

$$Q_N = \frac{P_N}{n_e n_N} \neq \sum_{i=0}^{Z+} \frac{P_{N^i}}{n_e n_{N^i}} = \sum_{i=0}^{Z+} Q_{N^i} \tag{5.8}$$

Note that Q_N is not the sum of the cooling curves associated with each charge state, but more like an effective cooling curve for all the individual charge states of that species.

Now if the impurity fraction f_N were constant in the SOL, then equation 5.8 can be integrated over the flux tube to give:

$$f_N = \frac{\int_{flux\ tube} P_N dV}{\int_{flux\ tube} n_e^2 Q_N dV} \tag{5.9}$$

To account for the fact that f_N varies along the SOL in SOLPS, an 'effective' constant nitrogen fraction required to dissipate the power that is radiated in that flux tube can be defined as follows:

$$f_{eff,N} = \frac{\int_{flux\ tube} P_N dV}{\int_{flux\ tube} n_e \frac{P_N}{n_N} dV} \tag{5.10}$$

We note that using this construct to define the impurity concentration makes the actual comparison with experiment difficult. However, this definition allows us to compare model predictions with the SOLPS simulations. Having defined a logic that works for nitrogen, we turn our attention to allowing for additional species, e.g. carbon and/or deuterium. We determine an 'effective' constant radiating species fraction, f_{eff} in a similar fashion to that shown for nitrogen:

$$f_{eff} = \frac{\int_{flux\ tube} [P_H + P_C + P_N]\, dV}{\int_{flux\ tube} n_e^2 Q_{HCN} dV} \tag{5.11}$$

where

$$Q_{HCN} = \frac{P_C + P_N + P_H}{n_e(n_C + n_N + n_H)} \tag{5.12}$$

In fact, Q(T) defined as in equation 5.12 is used to calculate the constant U in the DLS model (equation 5.3). Quantities on the RHS of equation 5.12 are obtained directly from the code and the integral in equation 5.3 is from the target to outboard midplane. With these definitions, in the case where f_N, f_C and f_H are constant, we recover $f_{eff} = f_N + f_C + f_H$. Therefore, to account for losses from both the main ion species and multiple impurity species, the comparison is carried out by setting f_I in equation 5.2 to f_{eff}.

Another DLS model parameter, κ_0, must also be abstracted from the SOLPS output. κ_0 is related to a scaled form of parallel heat flux $q = q_{||} B_\times / B$ (where $q_{||}$ is the parallel heat flux density) as follows:

$$\kappa_0 = \frac{qB^2}{T_e^{5/2} B_\times^2 \frac{dT_e}{dz}} \tag{5.13}$$

Note that in our calculation of κ_0 from SOLPS output for use with the DLS model, equation 5.13, we only apply it to the part of the flux tube where the total parallel conducted heat is ten times larger than the total parallel convected heat. Then, the average of the resulting range of κ_0 values calculated is taken to be the value of κ_0 in equation (eq. 5.3) when calculating U. We find that κ_0 calculated from the SOLPS output and used to calculate U varies between $\sim 1120 - 2190$ in the fuelling scan and between $\sim 950 - 1240$ in the seeding scan. This variation in the conductivity is

because of the application of flux limiters to the classical parallel conducted heat flux. However, due to the weak dependency of U on κ_0, the variation in U across both scans is small.

5.3 Comparison of DLS model predictions of detachment location with SOLPS-ITER results

The DLS model prediction of $C_{l,norm}$ for a given z_f is obtained by evaluating the RHS of equation 5.5 for the range $z_f = 0$ to $z_f = z_\times$. This is displayed by the solid black curve in figure 34. The z_f and $C_{l,norm}$ pairs derived from SOLPS output at each modelling D_2 and N injection rate once the 5eV point leaves the target (LHS of equation 5.5) are also shown, thus providing the various detachment position markers in z as a function of $C_{l,norm}$ for comparison with the DLS model. The peak in the impurity radiation losses is not shown because it generally coincides with the peak in the hydrogenic losses for most injections rates (figure 28). Also plotted in figure 34 is the DLS model prediction assuming linear variation in B between the X-point and target (black dash-dot line). A comparison of the non-linear $B(z)$ profile from SOL ring 2 and the linear $B(z)$ profile assumed is shown in figure 35 (left y-axis).

We will first discuss the 'linear' and 'non-linear' DLS model predictions. Our application of the generalised ('non-linear') DLS model predicts for the four cases shown, that the detachment location should move quickly to the edge of the high dB/dz region (shaded in grey) and then strongly slow down as a function of increasing $C_{l,norm}$. The DLS model predictions assuming linear variation in B also point to a general reduction in sensitivity of z_f to $C_{l,norm}$ even though dB/dz is constant between the target and X-point. The DLS model predictions can be understood by studying equation 5.5, reproduced below:

$$C_{l,norm}(z_f) = \frac{B_f \times \left[\int_{z_f}^{z_\times} B^2(z)dz + \int_{z_\times}^{L} \frac{B^2(z)(L-z)}{L-z_\times}dz\right]^{-2/7}}{B_t \times \left[\int_{z_t}^{z_\times} B^2(z)dz + \int_{z_\times}^{L} \frac{B^2(z)(L-z)}{L-z_\times}dz\right]^{-2/7}} = \frac{B_f}{B_t} \times \left(\frac{B_{INT,f}}{B_{INT,t}}\right)^{-2/7} \tag{5.14}$$

According to the model, $C_{l,norm}$ is essentially a product of two ratios: the ratio of the magnitude of B at the front location to that at the target, and ratio of the integrals in the square brackets which we have called $B_{INT,t}$ for when the front is at the target and $B_{INT,f}$ for when the front is somewhere between the target and X-point (as shown in equation 5.14). The values of these ratios and $C_{l,norm}$ for the non-linear and linear cases are displayed as a function of z on the right y-axis of figures 35(a) and 35(b) respectively. It can be seen that the strong increase in $C_{l,norm}$ between 15m-20m in the non-linear case is mainly driven by the increase in B_f in that region. The ratio of the integrals does not play a significant role in this region. In the case where linear variation in B

is assumed, the reduction in sensitivity of z_f to $C_{l,norm}$ (even though dB/dz is constant between the target and X-point) is a result of the increase in $(B_{INT,f}/B_{INT,t})^{-2/7}$. However, the ratio B_f/B_t still makes the dominant contribution to $C_{l,norm}$. This comparison highlights the role of dB/dz in the DLS model.

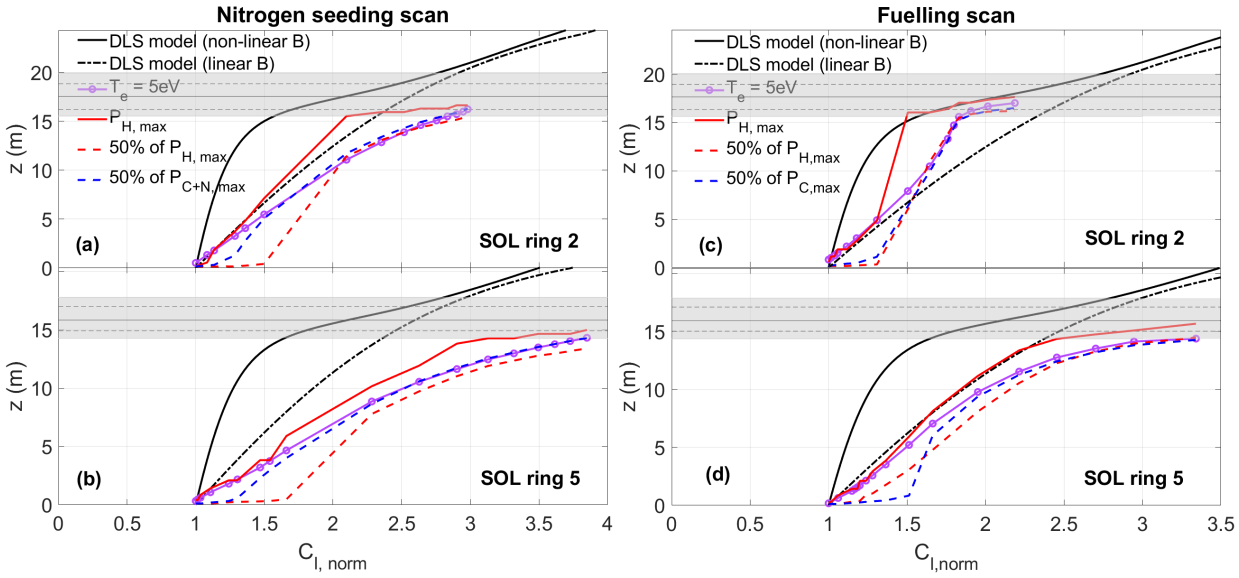

Figure 34: Predictions of the detachment front location, z_f, obtained from the generalised (solid black) and linear (dot-dash black) DLS models are shown as a function of $C_{l,norm}$. Three markers of the detachment location determined from SOLPS ($P_{H,max}$, 50% of $P_{H,max}$ and 50% of $P_{C+N,max}$ or 50% of $P_{C,max}$) are also shown. The region in which $dB/dz > 50\%$ of max dB/dz in that flux tube is shaded in grey.

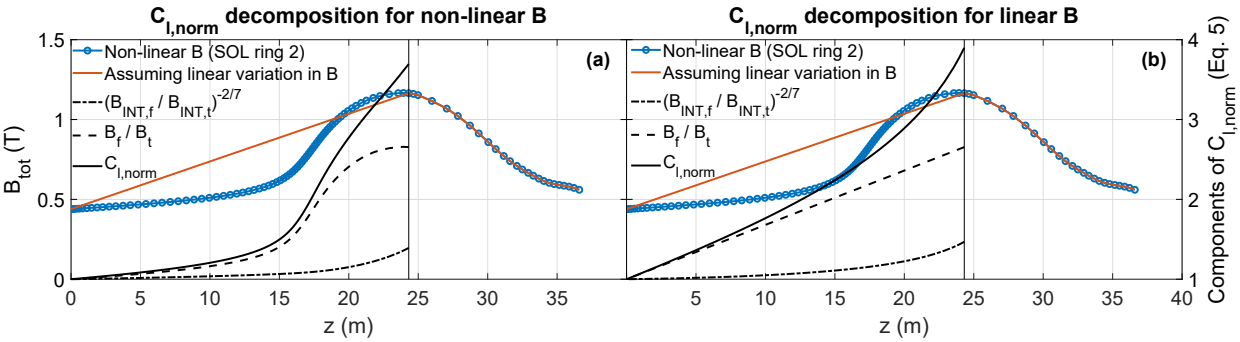

Figure 35: Components of $C_{l,norm}$ as a function of z obtained from the SOLPS geometry (a) and assuming linear variation in B_{tot} (b). The linear B_{tot} variation assumed and that from the SOLPS geometry are also shown for comparison.

We will now discuss the SOLPS results in the context of the DLS model. We find that the SOLPS simlulations also point to a general reduction in sensitivity of the location of the various markers to changes in $C_{l,norm}$ for all cases, but the movement between the target and the high dB/dz region is not as 'fast' as predicted by the generalised DLS model for any marker. Let us first consider the movement between the target and $z = 10$m. At first glance, the SOLPS results appear to agree more with the linear-B DLS model predictions rather than the predictions of the

generalised model. The fact that the linear DLS model predicts a relatively 'slow' movement in this region is a consequence of our choice of the linear $B(z)$ profile that we assume. Since the ratio B_f/B_t increases more strongly along z in the linear $B(z)$ profile compared to the non-linear $B(z)$ profile in this region, the linear DLS model predicts a stronger increase in $C_{l,norm}$ for increasing z. Therefore, it is likely that the apparent agreement with the linear DLS model is a coincidence, and that the SOLPS markers do not move as 'fast' as predicted by the generalised DLS model because of the additional physics in the SOLPS model. Let us now consider the region beyond $z = 10$m. In all cases, the movement of the $P_{H,max}$ marker (also the $P_{C,max}$ and $P_{C+N,max}$ markers, not shown) slows down significantly at the edge of the high dB/dz region, in qualitative agreement with the generalised DLS model. In D_2 fuelling scan, the movement of the $T_e = 5$eV location as well as of the markers corresponding to 50% of $P_{H,max}$ and $P_{C+N,max}$ also slows significantly at the edge of the high dB/dz region in both SOL rings. However, this is not clearly observed in the N seeding scan: only the $P_{H,max}$ marker slows down significantly at the edge of the high dB/dz region in both SOL rings, but this does not appear as significant for the markers in the N seeding scan.

We note that the 5eV point and the 50% points tracked in SOLPS (which we refer to as the detachment front location) also represent the cold end of the *thermal front* which sits between the detachment front and the X-point. Therefore, it is likely that most of the *thermal front* is actually in the high dB/dz region in both the flux tubes by the end of both scans.

It is interesting to note the relative position of the various SOLPS markers: markers corresponding to 50% of $P_{H,max}$ and $P_{C+N,max}$ lag behind the $T_e \approx 5$eV location when the detachment front is near the target, and all three markers become closer to the $P_{H,max}$ marker towards the end of the scan. Since the $P_{H,max}$ marker is almost always upstream of these three markers, this loosely points to a variation in the width of the thermal front through the both the scans. More generally, it highlights an important difference between the SOLPS results and the DLS model assumptions: the SOLPS results indicate that the thermal front likely has a finite width in these simulations which can vary significantly as it moves upstream, whereas the DLS model assumes that the thermal front width is small enough that the hot and cold ends of the thermal front are effectively at the same location.

A more direct comparison of the SOLPS and DLS model predictions for the sensitivity of the front location z_f to $C_{l,norm}$ can be carried out by taking the gradient $dz_f/dC_{l,norm}$ of all the traces in figure 34 and seeing how this changes along the field line. Such a comparison is displayed in figure 36 on the left y-axis. Also shown in figure 36 are the profiles of the magnitude of the total magnetic field B_{tot} and its gradient in z normalised to the maximum gradient in B_{tot} between X-point and target in the flux tube, $(dB/dz)/(dB/dz)_{max}$. As expected from figure 34, the DLS model predicts a significant reduction $dz_f/dC_{l,norm}$ in all cases as the region of high parallel

gradient in the field is approached. Since the SOLPS data is relatively sparse, $dz_f/dC_{l,norm}$ traces of the SOLPS markers is rather noisy, especially between $z = 0 - 5$m. However, SOLPS does seem to qualitatively agree with the trend predicted by the DLS model - there does appear to be a general reduction in sensitivity. Further, it is interesting to see that both the DLS predictions and SOLPS results appear to approach roughly the same value of $dz_f/dC_{l,norm}$ between $z = 10 - 15$m. It is noted that SOLPS results from SOL ring 2 of the fuelling, however, do not qualitatively agree with DLS predictions between $z = 5 - 10$m (ignoring the noise between $z = 0 - 5$m).

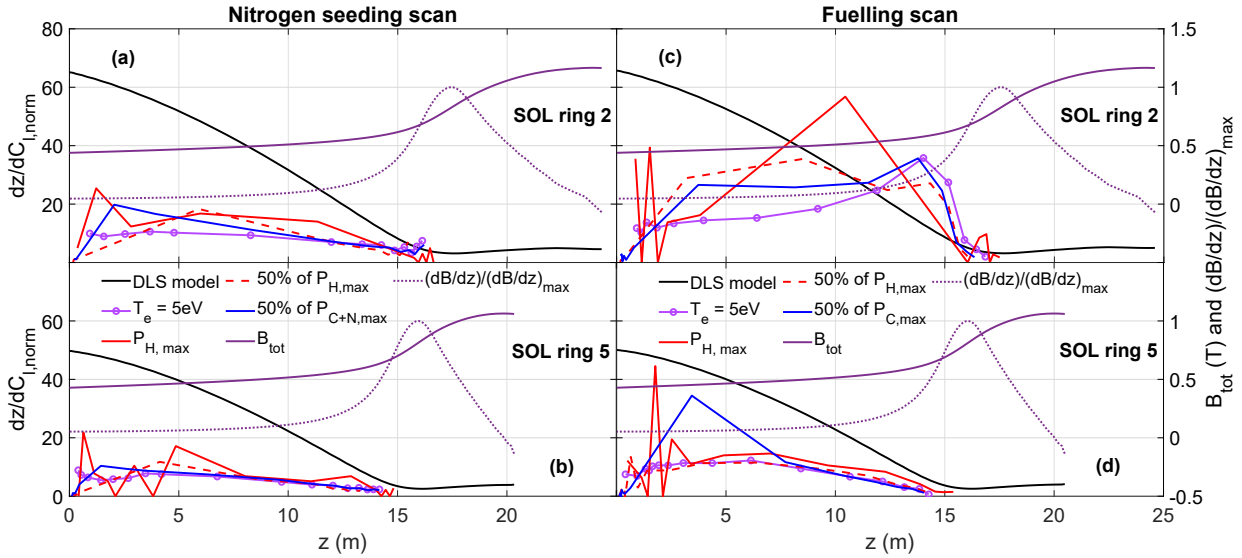

Figure 36: $dz/dC_{l,norm}$ obtained from the generalised DLS model and from the SOLPS output shown as a function of z. B_{tot} and dB/dz profiles in each flux tube also shown for reference.

To summarise, the analytical DLS model qualitatively captures an important trend observed in both the SOLPS scans, i.e. the reduction in the sensitivity of the detachment front location to controls as the front moves through a region of increasing parallel gradient in the total magnetic field. Potential reasons for the lack of a quantitative agreement and differences between the physics included in the DLS model and SOLPS will be discussed in the next section.

5.4 Discussion

In section 5.3 we have described the qualitative agreement between the DLS model and SOLPS simulations. As described in [76], the physics underlying the DLS model is related to the reduction in the parallel heat flux density through impurity radiation, that is accompanied by the reduction in $q_{||}$ due to the reduction of B along the field line. In other words, a larger parallel heat flux density must be dissipated as the thermal front moves upstream, requiring a bigger change in the control parameters to move the front up the flux tube in regions where the B field is increasing in the direction of movement. This is could be a reason why we see a qualitative agreement between

the DLS model and simulation results since this physics would also be captured in SOLPS.

Such a slowing down of the detachment front has also been postulated [147] for X-divertor configurations which have strong poloidal flaring of the field in the divertor. We note that the analysis in [147] attributes the slowing down of the detachment front location to the reduction in the neutral interaction area due to poloidal flux expansion, whereas the DLS model points to an increase in $q_{||}$ (moving upstream) due to total flux expansion. In an X-divertor scenario, if the poloidal field in the divertor volume is comparable to the toroidal field, it can be argued that both effects fundamentally point to the same physics: a significant increase in the poloidal field between the target and some distance upstream into the divertor volume would correspond to a significant increase in the total magnetic field, so a higher $q_{||}$ must be dissipated by any given energy loss mechanism; by impurities in the case of the DLS model and by neutrals as in the qualitative analysis in [147]. Further work is required to assess this potential connection.

Based on the simplifying assumptions of the DLS model, we do not expect quantitative agreement with the simulations presented here given the additional physics accounted for in SOLPS (e.g. more kinds of power losses, impurity concentration varying, pressure loss). In this work, the emphasis is that the DLS model can potentially tell us *where* and *why* we can expect a reduction in the thermal front location sensitivity to controls. With this in mind, in the following we will discuss some of the differences between the DLS model assumptions and the SOLPS simulations, and possible reasons why a quantitative agreement with SOLPS simulations is not observed. In addition, movement of the detachment front in the poloidal plane (as opposed to z) and the potential role the baffle could play on the front location sensitivity is also discussed.

5.4.1 Differences between energy loss mechanisms included in the DLS model and SOLPS-ITER simulations

As discussed in section 2.5, the DLS model, for simplicity and ease of obtaining an analytic solution, ignores power loss mechanisms other than radiation from a single impurity that has a fixed concentration along the flux tube. This is also true of other analytic models that rely on the Lengyel formulation [76, 138–143]. In SOLPS, multiple processes that remove power from a flux tube are present. The total power dissipated between X-point and target, P_{loss}, is given by equation 5.15:

$$P_{loss} = P_{C,tot} + P_{N,tot} + P_{H,tot} + P_{rad.\ trans.} + P_{other} \tag{5.15}$$

The variations of each of the terms in equation 5.15 are shown as a function of injection rate in figure 37 for both the N_2-seeding and D_2-fuelling scans. As expected for the fuelling scan, the hydrogenic power losses (deuterium excitation and ionisation, $P_{H,tot}$) are significant and higher

than losses due to carbon impurity radiation ($P_{C,tot}$) which only accounts for 10-15% of the losses in both flux tubes. In the seeding scan, while total radiation due to carbon and nitrogen impurities ($P_{C,tot} + P_{N,tot}$) is the dominant power sink over much of the scan, hydrogenic losses dominate over impurity radiation at low seeding rates. This makes sense as the seeding scan is started with a case from the fuelling scan that is at the edge of detaching.

Radiative and hydrogenic power losses together do not account for much more than half of the flux tube losses for ring 2 in both detachment scans. Power losses due to radial transport ($P_{rad.\ trans.}$) make a significant contribution, particularly for flux surfaces near the separatrix, ring 2. All other power losses (P_{other}), e.g. due to viscous and compressional effects, only make a small contribution to P_{net}.

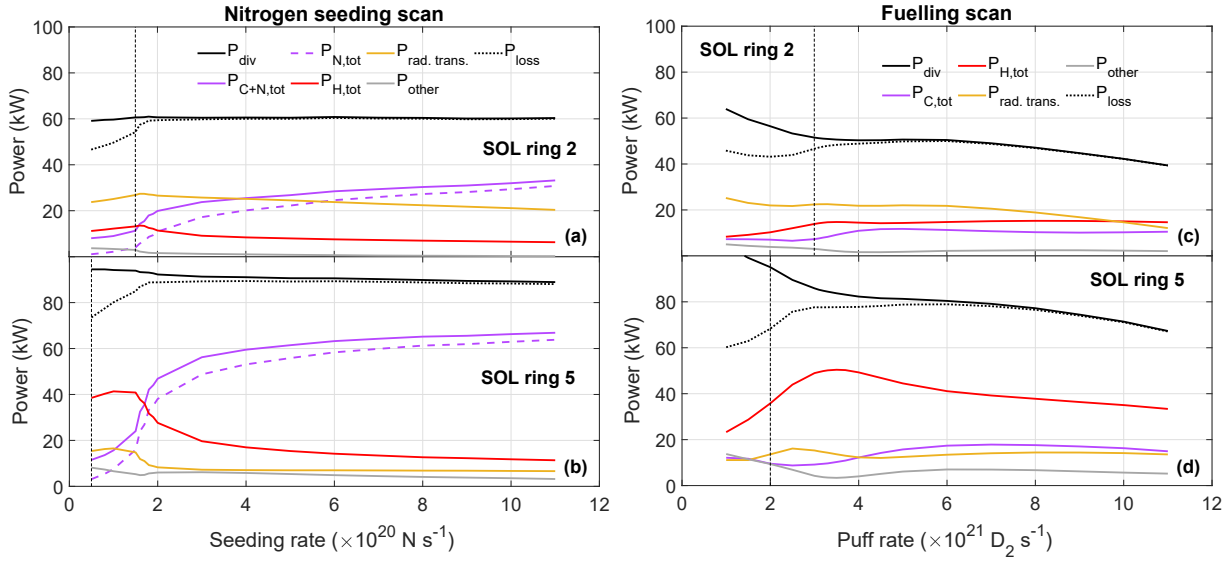

Figure 37: Description of contributors to power balance as a function of (a)-(b) nitrogen seeding rate; and (c)-(d) D2 fuelling rate. Shown are the total power source entering the flux tubes at the 'X-point' position, P_{div}; the total power dissipated between X-point and target, P_{loss}; and the components of P_{loss} (RHS of equation 5.15). The injection rate at which the 5eV point leaves the target is marked with a vertical dashed line.

5.4.2 Relationship between dB/dz and movement in l_{pol}

Because of the nature of the DLS model our primary focus up till now was on the movement of the detachment location in z. However, as a practical matter for detachment control and divertor physics studies, we are interested in the detachment location in l_{pol}, in the poloidal cross-section of the divertor, because: a) diagnostic measurements of the detachment location and radiation profiles are made in the poloidal plane; (b) the radiation profile in poloidal space plays a central role in determining heat loads on the divertor PFCs and therefore a useful input for divertor design and/or optimisation; c) the location of the detachment and thermal front with respect to the core plasma (X-point) will be useful in studying the impact of the extent of detachment on the core

plasma (impurity levels, confinement, etc.); and d) it is much easier to visualize what is happening in the 2D poloidal cross-section.

To review the detachment front movement in the poloidal cross-section we map the model predictions shown in figure 34 from z to l_{pol} using equation 5.1. The movement of the various markers in l_{pol} as a function of $C_{l,norm}$ is compared with the corresponding model prediction in figure 38. As seen previously for z space, a reduction in sensitivity of the l_{pol} location of $P_{H,max}$ (and also $P_{C+N,max}$ or $P_{C,max}$, not shown) to changes in $C_{l,norm}$ is observed in the region of high dB/dz in both scans; that again indicates that the movement of the *thermal front region*, which is ahead of the detachment front, has indeed slowed down as a function of increasing $C_{l,norm}$. In the seeding scan, there are differences in the movement of 5eV and 50% of $P_{H,max}$ points in l_{pol} space between figures 28 and 38. Our initial observation (figure 28) showed that at or before the high dB/dz region, these points clearly slowed down *as a function of the seeding rate*. We note that this is not observed for these points at or before the high dB/dz region *as a function of* $C_{l,norm}$. This difference could be partly due to variation in the thermal front width. Another likely reason is the fact that as the seeding rate is increased in equal steps, the steps in $C_{l,norm}$, dominated by f_{eff}, become smaller - this can be seen figure 33.

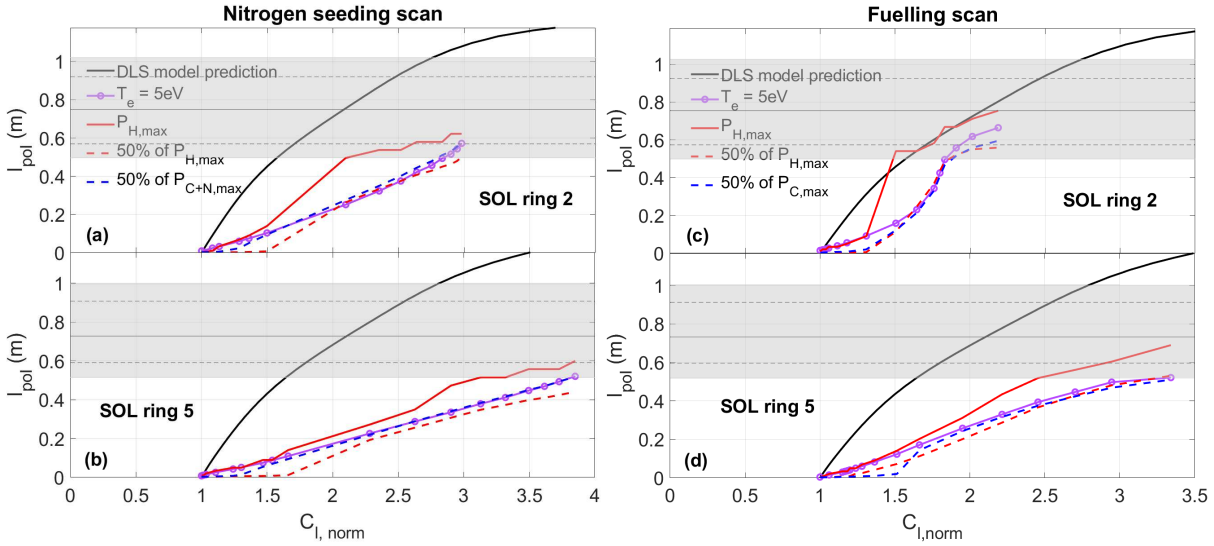

Figure 38: Detachment front location (multiple markers) in l_{pol} as a function of $C_{l,norm}$ as predicted by the DLS model and SOLPS. The region where $dB/dz > 50\%$ of the maximum dB/dz is shaded in grey.

We find that while the region of high dB/dz occupies only 15%-20% of the space between X-point and target in z, it occupies ≈40% of this space in l_{pol} for the Super-X geometry considered here. As a result, the significant reduction in detachment location sensitivity predicted by the model in z space translates to a mild reduction in detachment location sensitivity in l_{pol} in this geometry. To understand why this is the case, we must first understand how the region of dB/dz arises in this divertor geometry. Figure 39(a) shows the total field, B_{tot}, and the toroidal and

poloidal components, B_{tor} and B_{pol}, between X-point and target as a function of the major radius R for SOL ring 2. It can be seen that B_{tor} is the dominant component: the B_{tot} profile mostly lies on top of the B_{tor} profile. Since $B_{tor} \propto 1/R$, parallel gradients in B_{tot} would exist when the R coordinate of the field line increases going from X-point to the target. The 'faster' the R coordinate of the field line increases moving along the field line, higher the parallel gradient in B_{tot}. What 'moves' the field line to larger R going from the X-point to the target is the poloidal component, B_{pol}. The larger the poloidal component, the 'faster' the increase in the R coordinate moving along the field line; and the larger the parallel gradient in B_{tot} (as long as the B_{tor} dominates). This can be seen in figure 39(a) which also displays dB_{tot}/dz as a function of R: the parallel gradient basically increases and decreases as B_{pol} increases and decreases, with the maximum in both coinciding at the same R. For the Super-X geometry considered here, a 'faster' change in R as a function of the parallel distance z, driven by B_{pol}, translates to a larger change in l_{pol} for a given change in z. This is visualised in figure 39(b) which displays the z coordinate of the 'field line' in SOL ring 2 as a function of the l_{pol} coordinate. The regions of high parallel gradient in B_{tot} are also highlighted (pink) for both z and l_{pol}. Basically, a significant chunk of l_{pol} is covered in the relatively small z range which corresponds to the region of high parallel gradient in B_{tot}. This is why the region of high dB/dz occupies only 15%-20% of the space between X-point and target in z, while occupying ≈40% of the space in l_{pol} for the Super-X geometry considered here.

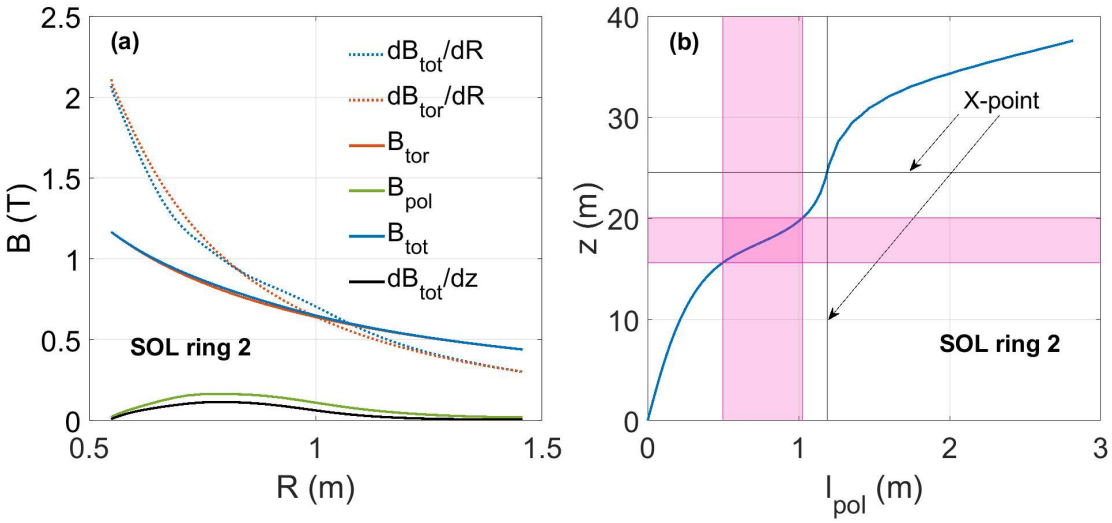

Figure 39: (a) Profiles of B_{tot} and its components between X-point and target, as well as of dB_{tot}/dz, dB_{tot}/dR and dB_{tor}/dR, all as a function of major radius. (b) Relationship between z and l_{pol}, and the space occupied by the region of high parallel gradients in the B-field in both coordinates.

It is interesting to note the dramatic difference between dB_{tot}/dz and dB_{tot}/dR (or dB_{tor}/dR), also displayed in figure 39(a). At first glance, this suggests that to maximise the parallel gradient in B_{tot}, one must pull the outer leg straight out in R as much as possible. In reality, however, this can only be done by significantly increasing B_{pol}, which would take us away from a $B_{tor} \propto 1/R$

dominated divertor in which the position of the maximum in B_{pol} would determine the position of the maximum dB_{tot}/dz. Further, it appears that the returns of a high B_{pol} to move the field out faster in R diminish at larger R. In addition, dB_{tot}/dR is the highest close to the X-point, where B_{pol} is naturally going to be low. These competing effects point to a potentially important insight: in reality, there is limited flexibility when it comes to changing or optimising the *location* of the high dB_{tot}/dz region in the poloidal plane in this geometry. However, it does seem that there is scope for the magnetic geometry used in this work to be optimised significantly by increasing the peak in B_{pol} in its present location in R, effectively increasing the maximum in dB_{tot}/dz without significantly changing the poloidal coverage of the region of high parallel gradients as defined in this work, which is likely to be of interest for improved control of the detachment/thermal front. Future work could focus on the scope of such an optimisation of the Super-X geometry used in this work.

5.4.3 Variation in the thermal front width

While most of our work has been focussed on the detachment front, the thermal front is of great importance to the DLS model, which assumes that the thermal front is short compared to the length of the flux tube in the divertor. A short length means that the distance between the hot (z_h) and the cold end of the thermal front (at z_c) is small compared to distance (in z) between the target and X-point; this allows for thermal front (and detachment front) movement within the divertor - the goal of the model. z_c corresponds to the detachment front location and to the 50% point on the divertor side of the radiation profile. Without a clear idea of how to determine the forward edge of the thermal front, z_h, we have chosen the point where the radiation falls to 50% of the maximum on the X-point side. In the simulations studied here, we find that the thermal front width varies in both scans as the injection rate is increased and can be comparable to the divertor size.

As was shown earlier in the thesis, the cold end of the thermal front z_c, which corresponds to the detachment front, moves from the target to a point where dB/dz ≈50-90% of the maximum dB/dz in the flux tubes considered (figure 34). Although not specifically shown in this thesis, we also tracked z_h and found that it is already far into the region of $dB/dz \geq 50$ % of the peak value at detachment onset and does not move much throughout both scans - this can roughly be seen in figures 27(d) and (e) (the $dB/dz \geq 50\%$ region corresponds to $0.5 \leq l_{pol} \leq 1.0$). Most of the the changes in the thermal front are in its 'length' in l_{pol} (and z and l) which shortens because of the movement of z_c during the two scans. As a result, it is difficult to develop a consistent SOLPS measure of the actual thermal front location in these simulations. We therefore track the location cold end of the thermal front or the detachment front as it is easier to define and its location

and movement is co-related with that of the thermal front. However, this kind of variation in the thermal front width is likely an important reason for the observed quantitative disagreement.

Why is it that the thermal front becomes narrower as detachment proceeds? As discussed in the DLS model paper [76], the length of the thermal front, between the 'hot' and 'cold' ends, Δ_{z_f}, is inversely proportional to $q_{||}$:

$$\Delta_{z_f} \equiv z_h - z_c \approx \frac{B_\times}{B(z_h)|q_{||}|} \tag{5.16}$$

Thus the significant length of the thermal front in MAST-U, particularly at the start of detachment, is likely due to the relatively low power entering the scrape-off layer. As the front moves upstream, $B(z_h)$ and $q_{||}$ both increase, lowering Δ_{z_f}.

In the case of reactors using seeding of impurities for divertor radiation, Δ_{z_f} is likely to be a lot smaller than for MAST-U and with respect to the divertor size of a reactor. If a reactor uses several radiators from low- to mid-Z which radiate over a wider temperature range, then that is likely to lead to a broader thermal front than for a single low-Z impurity. Further work is required to quantify the dependency of the thermal front width on P_{div} and on the use of different impurities as a 'narrow thermal front' is an important DLS model assumption.

5.4.4 The causes of differences between the DLS model and SOLPS results

At first glance the quantitative mismatch between the DLS model and the SOLPS results is a bit discouraging. However, it at least argues that for the MAST-U Super-X divertor, the detachment location will be more controllable than predictions of the DLS model.

The quantitative mismatch between the DLS model prediction and the SOLPS results could be due to several factors, or some combination: (a) As discussed regarding figure 37, there are several physics processes not being included (mainly cross-field transport) that significantly affect the power balance; (b) the DLS model is a better predictor of the location of some other part of the divertor plasma - e.g. some part of the thermal front or the radiation peak as opposed to the detachment front; or (c) Interaction of the plasma with various surfaces that form the divertor region could have a local effect on the plasma, where recycling is raised or lowered as the detached or attached regions shift; and (d) the region of high dB/dz coincides with the baffle/divertor entrance - in order to maintain plasma-neutral pressure balance, a tightly baffled divertor could potentially prevent the thermal front from moving into the main chamber.

Cross-field transport In terms of case (a), more energy loss mechanisms could be added to the prediction as we have done with the use of f_{eff}. In particular, the cross-field losses, in most cases plotted in figure 37, *drop* during the seeding and fuelling scans, which is equivalent to an

increasing P_{div} or decreasing f_{eff}. The net effect would be to reduce $C_{l,norm}$ for the same z or l_{pol}, shifting the data closer to the DLS model prediction. However, such efforts to add more physics to the DLS model would degrade its clarity and usefulness.

Variation in the thermal front width Case (b) has been addressed obliquely at points in this thesis by assuming that the radiation profile extent is in rough correspondence to the thermal front - the 50% points on the leading and trailing sides of the radiation profile approximating z_h and z_c respectively, with the peak in radiation being somewhere in the middle of the thermal front. We have shown that the peak in the radiation profile is closer to the DLS prediction than the detachment front in either l_{pol} or z space. z_h hardly moves after detachment, staying in the high dB/dz region, past the peak.

Neutral trapping and associated power loss There are already existing studies that address case (c): Experimental and modelling studies of DIII-D [73] and TCV [80] show that neutral recycling and location of baffles can work to either enhance (DIII-D) or reduce (TCV) the effect of total flux expansion. The effect is thought to be due to increasing or decreasing the neutral ionization in the divertor (or more specifically, due to changes in 'neutral trapping' [80]), raising the target density and lowering the target temperature through modification of power losses in the flux tube.

The role of a tight baffle and plasma-neutral pressure balance In the current MAST-U study, the role of the baffle at the entrance to the divertor could be very strong. We find that the detachment front at the highest seeding/fuelling rates is located ∼15-20cm downstream in l_{pol} from the N-seeding location on the 'roof' of the divertor chamber (figures 27(a) and (b)); beyond that the curved section of the baffle forms the entrance to the divertor. In such a tightly baffled divertor as in MAST-U, the baffle strongly limits the capability of neutrals to move along the side of the plasma fan, which itself serves to ionize most, if not all, neutrals trying cross through it. Neutrals trying to penetrate that region are ionized, flow back to the targets and recycle as neutrals again. The detachment front then sits slightly inside the entrance to the divertor, in a region of high neutral gas pressure. If the detachment front were to move past the the divertor entrance towards the X-point, then the narrow entrance to the divertor is no longer as well plugged by the plasma, and the neutral gas pressure behind and in the thermal front could drop. The need to maintain pressure balance between the plasma and the neutrals could cause the front to move back into the divertor, providing a feedback mechanism which would help prevent the detachment front from leaving the closed divertor. This physics associated with plasma-neutral pressure balance, which is not included in the DLS model, would be captured in SOLPS.

5.5 Conclusions

Detachment evolution in the MAST-U Super-X geometry has been studied using the SOLPS-ITER code, with a focus on the sensitivity of the detachment front location to control parameters. Two sets of steady state solutions were obtained by scanning the D_2 and N injections rates at fixed input power (2.5MW), ranging from attached to strongly detached conditions. Movement of the detachment front location is tracked in two characteristic flux tubes as a function of physics control parameters: power passing through the flux tube at the X-point position (P_{div}), upstream density (n_u) and the effective radiating species fraction (f_{eff}). Different measures of the detachment location are developed and compared for tracking its location.

In both seeding and fuelling scans, the detachment front location initially moves quickly off the target along a field line or equivalently in the poloidal direction for equal steps of N seeding or D_2 fuelling. The front movement slows down as it moves through a region of increasing dB/dz. After a factor of up to 10× and 5× increase in the seeding and fuelling rates past the detachment threshold, the detachment front has reached less than halfway to the X-point in l_{pol} where dB/dz ∼50% of its maximum value, close to the baffle or divertor entrance.

The SOLPS results are compared to the predictions of the DLS model which is based only on energy balance and makes a number of simplifying assumptions to ease understanding and predict dependencies on various divertor design characteristics. Both the DLS model and SOLPS predict a reduction in the sensitivity of the detachment front location along a field line, z, to control parameters in the region of high dB/dz for the MAST-U Super-X configuration. Such a drop in sensitivity to controls is equivalent to enhanced detachment control. Both the DLS model and the SOLPS cases studied suggest that the MAST-U Super-X configuration may be able to accommodate larger power transients compared to a conventional divertor while still keeping the divertor plasma detached with the detachment front kept away from the X-point or target. This is because of the relative large change in controls required to move the thermal/detachment front through a region of high parallel gradients in B.

The extent of the high dB/dz region is changed when examined in l_{pol} compared to along a field line (z space). The high dB/dz region in z space is small (∼15-20%) compared to the distance along z from target to X-point position. In comparison, the high dB/dz region in l_{pol} space is a much larger (∼40%) fraction of the distance from the target to the X-point. That translates to a milder reduction in sensitivity in poloidal space for the divertor geometry considered. It appears that there is limited flexibility when it comes to changing or optimising the location of the region of high parallel gradients in B in the poloidal plane. However, there may be scope to further optimise the Super-X geometry used here: the maximum parallel gradient in B in its existing location could

be increased further by increasing the poloidal field.

There is a quantitative mismatch between SOLPS and DLS model predictions of the detachment front location sensitivity to control parameter variation; the DLS model predicts faster upstream movement of the detachment front between the target and the region of high dB/dz (detachment location more 'sensitive' to control parameter variation), compared to SOLPS results for the same control parameter variation. This could be due to a number of reasons. For example, the DLS model does not include cross-field transport of power out of the flux tube and the thermal front width is assumed to be small compared to the divertor size. Such shortcomings may be less important when the model is applied to reactor-level parallel heat fluxes if there is strong reliance on a single low-Z impurity to dissipate most of the power entering the divertor. However, further work is needed to understand the dependence of the thermal front width on the power entering the divertor and the impurity (or impurities) chosen to dissipate that power. Furthermore, the location and effect of surfaces could be important. For example, the region where the detachment front becomes less sensitive to changes in control variables is also close the divertor opening. Thus, the trapping of neutrals in the divertor, which can change as the detachment moves, could also be playing a role in slowing down the detachment front location movement.

Chapter 6

Impact of ion-molecule elastic collisions on strongly detached conditions

As described in section 4.3, the key observation associated with this chapter is that volume recombination plays an important role in bringing down the total particle flux to the target in the D_2 fuelling scan which includes ion-molecule elastic collisions. Volume recombination plays a negligible role in reducing the particle flux to the target in the N seeding scan and the D_2 fuelling scan in which ion-molecule elastic collisions are not included. A strongly detached case was chosen from each scan for further analysis such that the extent of the detached region is similar amongst the cases compared - cases A, B and C, figures 30 and 31.

In this chapter, we take a closer look at cases A, B and C; with a special focus on the role of ion-molecule elastic collisions. We find that in case A, ion-molecule elastic collisions modify the energy, momentum and particle balance such that lower plasma temperatures and higher densities are achieved near the target. In case C, we find that the impact of ion-molecule elastic collisions is weakened due to the presence of a large amount of singly ionised nitrogen in the detached region. The nitrogen modifies the energy, momentum and particle balance such that it generally prevents increases in the density and reductions in the temperature near the target.

We focus our analysis on a single flux tube (SOL ring 5), shown in blue in figure 21(b). This flux tube, which has been chosen for all 'flux tube' analyses presented in this chapter, delivers the peak particle flux to the target when the fuelling rate is 2×10^{21} D_2 s^{-1} (no nitrogen, ion molecule elastic collisions included, blue diamonds in figure 30), i.e. the 'attached' case common to the fuelling scan and the seeding scan. We choose this flux tube for analysis because it does not suffer from radial losses as strongly as, for example, the flux tube which delivers the peak heat flux to

the target (SOL ring 2), but is still not too far from the separatrix. Some basic characteristics of the plasma in this flux tube are summarised for each case in the table below.

	Case A	Case B	Case C
$n_{e,u}$ ($\times 10^{19}\mathrm{m}^{-3}$)	1.6	1.5	0.9
$T_{e,u}$ (eV)	37.4	41.6	50.7
P_{div} (W)	6.7×10^4	7.9×10^4	8.9×10^4

Table 6: Values of the outboard midplane electron density and temperature, $n_{e,u}$ and $T_{e,u}$, and power entering the flux tube at the X-point position, P_{div}, in the cases chosen for analysis.

In the next section, we study the impact of the temperature and density on recombination levels. The consequence of differences in the thermal front characteristics on the impurity and neutral levels in the detached region is described in section 6.2. Section 6.3 provides a description of how neutrals and impurities affect the plasma energy, momentum and particle balance across the detached region and shape the corresponding temperature and density profiles. Conclusions are summarised in section 6.4. This chapter has been adapted from the following paper:

- O. Myatra et al. "Impact of ion-molecule elastic collisions on strongly detached MAST-U Super-X divertor conditions according to SOLPS-ITER" (soon to be submitted)

6.1 Impact of density and temperature on recombination

Given that recombination is a key difference between the various detached cases and that it depends on the plasma density and temperature, we first examine these characteristics of the plasma in each case. We utilise figure 40 for this discussion, where the net volumetric recombination sink, S_{rec}, electron density, n_e, and temperature, T_e, profiles along the flux tube are displayed for each case as a function of the parallel distance from the target. The detached region extends from the divertor target to $\sim$7m where the vertical lines are placed; where the total parallel conducted heat is equal to that transported by convection - the extent of the detached region is similar in each case for this flux tube.

As pointed out in the discussion of figure 30, the S_{rec} is different amongst the three cases. In case C, S_{rec} increases by almost an order of magnitude across the detached region but still is the lowest everywhere in the divertor amongst the three cases. In case B, S_{rec} also increases by less than an order of magnitude but only at the start of the detached region and changes little across most the detached region. In case A, S_{rec} increases by almost three orders of magnitude between the start of the detached region and the target. The majority of the recombination is localized very close to the divertor plate; there is a sharp increase (by more than an order of magnitude) across the region between 0m $-$ 1m parallel distance from the target. These features of S_{rec} are

reflected in the T_e and n_e profiles, shown in figure 40(b). The thin region of strong recombination in figure 40(a) coincides with a similarly thin sub-eV region in figure 40(b). We also observe a qualitative difference between the n_e profile in case A and the ones in cases B and C (as pointed out earlier and discussed in more detail later) - the density at the start of the detached region is roughly $6 - 7 \times 10^{19}$ m^{-3} in both the fuelling cases and about 4×10^{19} m^{-3} in the seeding case. While there is little change in n_e across the detached region going towards the target in cases B and C, it increases significantly to more than 1.5×10^{20} m^{-3} in case A, consistent with the general increase in S_{rec} across the detached region.

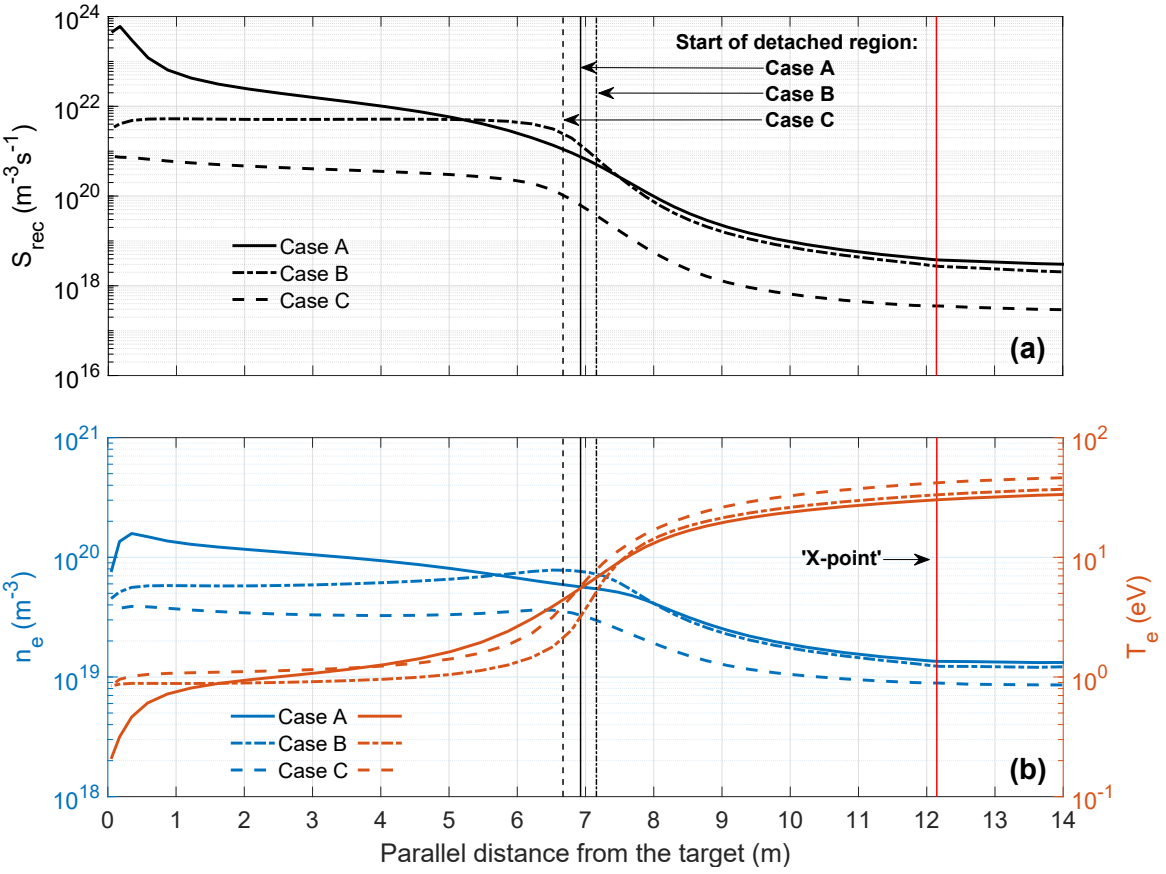

Figure 40: 1D profiles of (a) S_{rec} and (b) n_e and T_e from cases A, B and C for the flux tube highlighted in blue in figure 21(b). The vertical lines at ∼7m represent the start of the detached region. Higher densities and sub-eV temperatures are achieved in case A leading to high recombination levels.

Since the recombination rate depends both on density and temperature, those two plasma characteristics are determining the resultant S_{rec} profiles. The question we address now is which of density and temperature is the dominant determinant of the recombination rate and in which regions. We utilise figure 41 for this discussion where the S_{rec} profiles obtained from the code shown in figure 40(a) are re-plotted (and renamed as $S_{rec,code}$) as a function of the corresponding T_e for each case. The temperatures at the start of the detached region are marked with vertical lines. As mentioned earlier, the region of strong recombination for case A is localised between 0m − 1m

parallel distance from the target for the flux tube considered. The temperature range in this region is highlighted in red for case A and in green for case C (the corresponding T_e range for the case B falls within the green region). To separate the effects of n_e and T_e on the recombination levels, we have used the T_e profiles from figure 40(b) along with rate coefficients obtained from AMJUEL (H.4 2.1.8) to calculate the recombination rate for 4 fixed densities, $S_{rec,post}$ $(= n_e^2 < \sigma v_{rec}(T_e, n_e) >)$, also displayed in figure 41 as a function of T_e to compare to the $S_{rec,code}$ profiles.

For cases B and C, we find that over the detached region with $T_e \geq 1$eV, the temperature is the dominant factor determining the *rise* of $S_{rec,code}$ in each case as there is little change in density for the individual cases over that temperature region. While this is also true for case A, the increase in n_e does appear to make a considerable contribution. On the other hand, it can be seen that the differences between $S_{rec,code}$ amongst the three cases in the $1\text{eV} - 10\text{eV}$ region are driven by differences in density. Note that in the $1\text{eV} - 10\text{eV}$ region, radiative recombination dominates over three-body recombination.

The above picture changes when examining the region of $T_e \leq 1$eV, reached only by case A. It can be seen that $S_{rec,post}$ is not as sensitive to temperature in the range $1\text{eV} \leq T_e \leq 10\text{eV}$ as compared to when $T_e \leq 1$eV. For all four individual densities, $S_{rec,post}$ increases only by roughly an order of magnitude as the temperature drops from 10eV to 1eV, and then by about two orders of magnitude as it drops to 0.2eV. For case A, even though there is a slight drop in density over the low temperature region, $S_{rec,code}$ increases by almost two orders of magnitude indicating that achieving such temperatures is required to reach high levels of recombination.

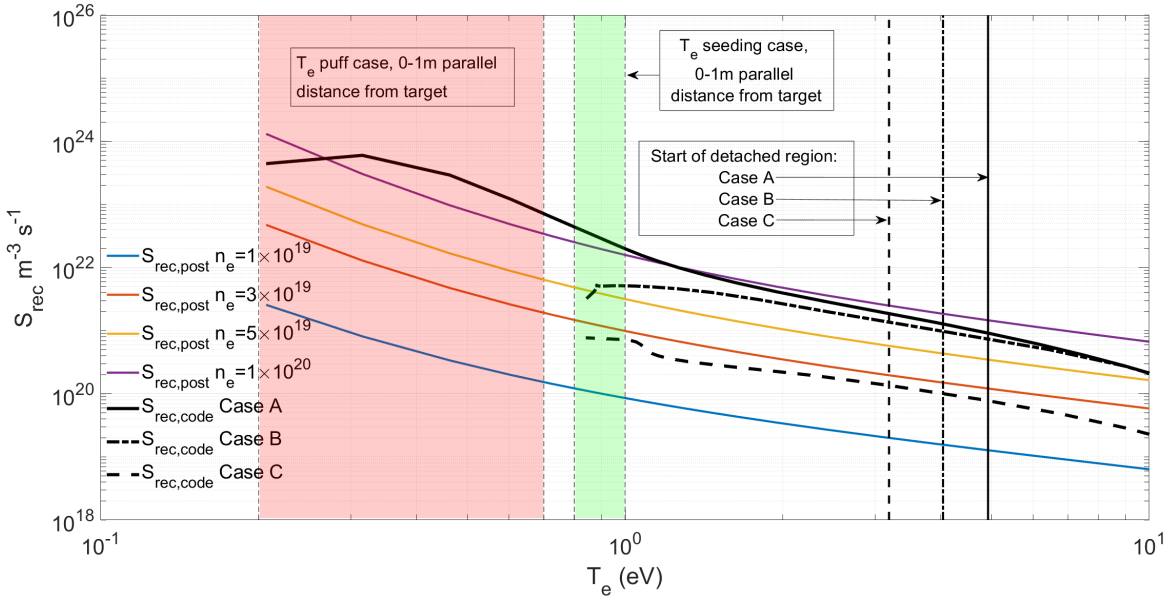

Figure 41: Comparison of the recombination sink post-calculated using AMJUEL at fixed n_e ($S_{rec,post}$) and the recombination sink obtained from the code ($S_{rec,code}$) for each case as a function of T_e. Recombination levels are strongly enhanced at sub-eV temperatures for all densities.

It will be shown in section 6.3 that the differences in the plasma densities and temperatures amongst three cases is due to differences in the impurity and neutral levels and their impact on energy, momentum and particle balance across the detached region. However, this difference in the impurity and neutral levels is actually a consequence of differences in the thermal front power loss composition - fundamentally, it is this power loss composition that is by design different in the strongly detached solutions obtained from the fuelling and seeding scans. So in the next subsection, we will discuss the impact of the thermal front characteristics on the impurity and neutral levels in the divertor.

6.2 Impact of thermal front characteristics on impurity and neutral content

As mentioned earlier, the thermal front is a localised region in the divertor where most of the power coming in from upstream is dissipated through various mechanisms. In this work, for a given SOL ring, we define the thermal front as the region across which the total power dissipated along the field due to all possible mechanisms ranges from 5% to 95% of the power entering the flux tube at the X-point. In this section, we will compare the thermal front characteristics in each of three cases chosen for analysis and describe how the differences in the power loss composition of this region correspond to relatively high neutral levels across the detached region in cases A and B; and relatively high impurity levels across the detached region in case C.

In figures 42(a)-(c), the total cumulative power loss fraction (f_{pow}) is shown for each case along with the contributions from impurity radiation and hydrogenic losses (deuterium excitation and ionisation) as a function of parallel distance from the target for the region between the X-point and the cold end of the thermal front. The vertical red lines represent the hot and cold ends of the thermal front. The fundamental difference between the fuelling cases and the seeded case (by design) is the fact that in the fuelling case, a large fraction of power ($\approx$ 50%) is lost to deuterium excitation and ionisation with a smaller fraction ($\approx$ 20%) lost to impurity (carbon) radiation; whereas in the seeded case, most of the power ($\approx$ 70%) is lost to impurity (nitrogen) radiation with hydrogenic losses only making a small ($\approx$ 10%) contribution. Given that the power entering the flux tubes at the X-point position is similar in each case, for the fuelling cases this leads to much more power available for ionization of recycled and/or recombined deuterium, and therefore a significantly larger particle source in the thermal front. In detached conditions, the dominant divertor plasma source is neutral ionisation. This source cannot be sustained without a sufficient flow of neutrals into the thermal front from an adjacent neutral cloud. Since the divertor neutral content is actually linked to the ionisation source through recycling (and sometimes volume

recombination), a large ionisation source in the thermal front corresponds to a high neutral density in the detached region, as can be seen in figures 42(d)-(f) which displays the deuterium atomic and moleculer densities (left y-axis, note the log scale). Figures 42(d)-(f) also display the parallel electron flux, Γ_e, for each case (right y-axis, *not* a log scale). In case A, a large amount of plasma is created in the thermal front and as a result, the plasma flux exiting the thermal front is twice that in case C. This plasma flows towards the target through a neutral cloud that is about five times as dense as that in case C, leading one to expect significantly higher plasma-neutral interactions across the detached region in case A. This has important consequences for the plasma energy and momentum balance across the detached region, discussed in the next section.

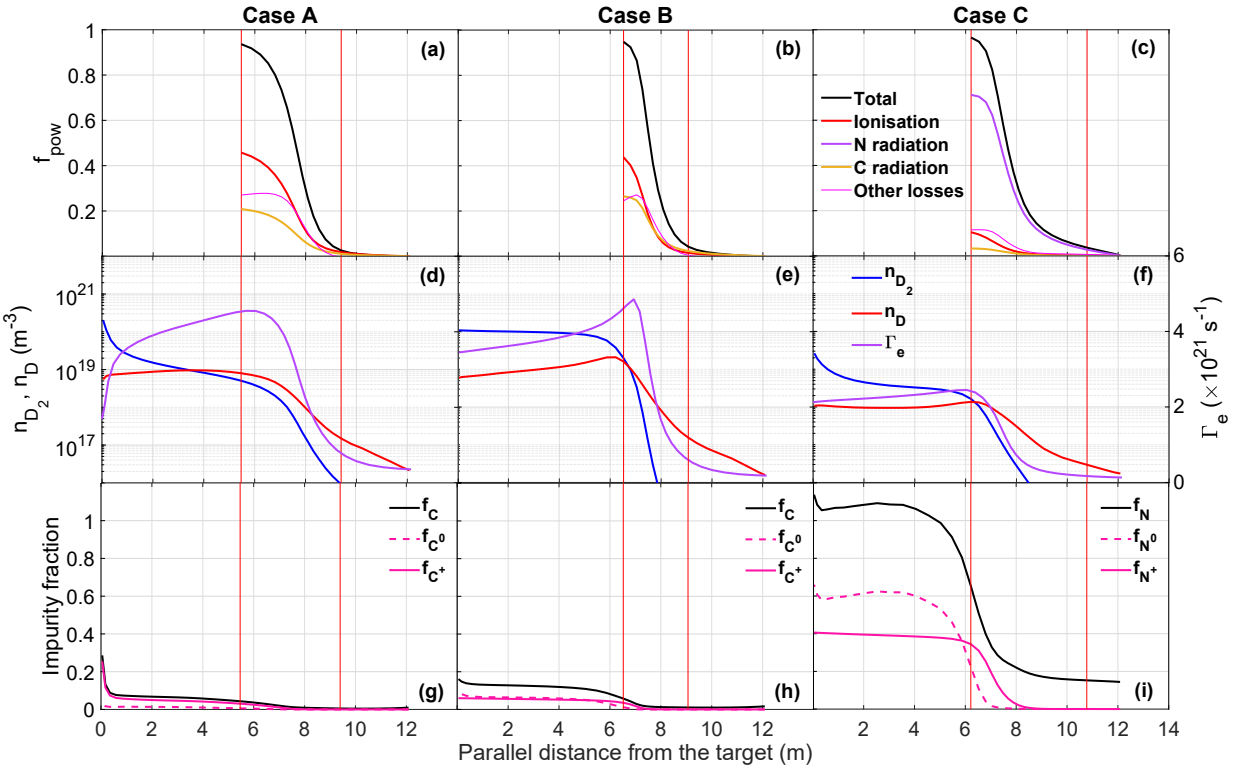

Figure 42: Figures (a)-(c) show the thermal front power loss composition - in case C, impurity (nitrogen) radiation dissipates most of the power entering the divertor while hydrogenic excitation and ionisation only make a small contribution. The opposite is true in the fuelling scans - hydrogenic losses make the dominant contribution to f_{pow}. Since the power entering the divertor in all cases is similar, this means that more plasma is created in the thermal front in cases A and B. This is seen in figures (d)-(f) which shows parallel electron flux Γ_e (right axis) as a function of parallel distance - plasma flux exiting the thermal front in cases A and B is twice that in C. Figures (d)-(f) show the molecular and atomic deuterium densities (left axis, note log scale). Neutral levels in the detached region are linked to the ionisation levels through recycling - therefore in the fuelling scans, the neutral densities in the detached region in cases A and B are also significantly higher. A large amount of impurity radiation across the thermal front would correspond to a higher impurity fraction in the detached reigon. This is seen in figures (g)-(i) which show impurity fraction $f_I = (n_{I^0 + \ldots + I^{z+}})/n_e$, impurity neutral fraction $f_{I^0} = n_{I^0}/n_e$ and singly ionised impurity fraction $f_{I^+} = n_{I^+}/n_e$ where $I = C$ or N

Just like a large ionisation source in the thermal front means a high neutral density in the

detached region, a larger impurity radiation power sink in the thermal front corresponds to higher impurity levels in the detached region. This can be seen in figures 42(g)-(i) which display profiles of the carbon fraction, $f_C = (n_{C^0+...+C^{6+}})/n_e$, from cases A and B and the nitrogen fraction, $f_N = (n_{N^0+...+N^{7+}})/n_e$, from case C as a function of the parallel distance from the target. Across the detached region in cases A and B, it can be seen that $f_C \sim 0.1$ and $f_C \sim 0.15$ respectively. The impurity fraction in case C is significantly higher than that in the non seeded cases. While there is little change in the nitrogen fraction between the divertor entrance ($f_N \sim 0.15$) and about halfway into the thermal front ($f_N \sim 0.2$), it increases significantly across the rest of the thermal front and continues to increase before saturating around 4m, and stays higher than 1 across the rest of the detached region where the nitrogen radiation density is actually less than 5% of the maximum (note that the impurity fraction can go above 1 when impurity neutrals are included in the definition as we have done here). The localised nitrogen radiation region is sustained by a flow of nitrogen into the thermal front from a relatively dense cloud of nitrogen atoms in the detached region. The average nitrogen fraction in this flux tube, $< f_N >_{average} = 0.39$, is strongly weighted by the nitrogen (mainly N^0 and N^+) in this low-radiation cloud across a rather large detached region. The presence of a large amount of N^+, again, has important consequences for the divertor plasma energy and momentum balance, which we will discuss in the next subsection.

As an aside, we note that this impurity fraction may seem high compared to experimentally reported values. However, impurity concentration measurements rely on the radiation intensity so values of f_N reported in experiments typically represent estimates of the concentration in the radiating region or the thermal front. Concentration in the cold regions of low radiation is generally not measured, and it is likely that the concentration in these regions is higher than what is reported in experiments.

It also is interesting to note the differences in the D_2 density profile between the three cases. In both cases A and C, there is a sharp increase in the molecular density near the target, but this is not observed in case B. As seen earlier, the temperature across the detached region is similar and mostly constant in cases B and C, while n_e is higher in case B, this is also mostly constant in both cases (figure 40). It is therefore unlikely that dissociation is playing a significant role in driving the sharp change in the molecular density near the target in cases A and C. Ion-molecule elastic collisions are present in cases A and C but not in case B. This seems to suggest that this interaction essentially keeps the molecules 'squashed' near the target.

To summarise, a thermal front in which hydrogenic losses make the dominant contribution corresponds to a scenario where a relatively large plasma flux exits the thermal front to interact with a relatively high neutral density cloud across the detached region downstream. On the other hand, when the losses are dominated by impurity radiation, this corresponds to a relatively small

plasma flux, but with a high impurity fraction, exiting the thermal front and flowing through a relatively low neutral density cloud across the detached region. In the next subsection, we will discuss the consequences of these differences in the neutral and impurity levels on the energy, momentum and particle balance across the detached region and how this affects the corresponding temperature and density profiles.

6.3 Energy, momentum and particle balance in the detached region

We have seen that the differences in the recombination is a result of differences in the plasma density and temperature profiles. We have also seen that differences in the thermal front characteristics affect the neutral and impurity levels in the detached region. In this section, we will look at how these neutrals and impurities affect the energy, momentum and particle balance across the detached region in each case and shape the corresponding plasma temperature and density profiles. Since the qualitative features of the detached solutions obtained through seeding are recovered in the fuelling scan by turning off $D^+ - D_2$ elastic collisions, we focus our analysis on the impact of this particular interaction on the balances and show how these elastic collisions lead to lower T_e and higher n_e in case A, and discuss how in case C a high f_{N^+} in the detached region may be weakening the impact of the elastic collisions on heat and momentum dissipation, resulting in higher T_e near the target and lower n_e across the detached in this case.

6.3.1 Impact of $D^+ - D_2$ elastic collisions on energy and momentum balance across the detached region

Since the focus of this subsection is to describe the impact of $D^+ - D_2$ interactions, we only consider the ion energy balance which does not directly involve T_e. However, across the detached region, we find that the ion and electron temperatures are roughly equal and therefore strongly coupled - a drop in T_i corresponds to a similar drop in T_e. We also find that ion heat conduction ($q_{i,cond}$, shown in figure 43(a)-(c)) is small compared to convection ($q_{i,conv}$) across the detached region in all cases, and therefore do not include it in our energy balance analysis. The total convected ion energy ($q_{i,conv}$) flowing along a fluxtube of cross-sectional area $A_{||}$ is given by equation 6.1, where $q_{i,kin}$ and $q_{i,int}$ are the directed kinetic energy density and the internal energy density components of $q_{i,conv}$ (also displayed in figures 43(a)-(c)); and m_{is}, n_{is} and $v_{is,||}$ are the mass, density and the velocity component parallel to B of an ion species is.

$$q_{i,conv} = q_{i,kin} + q_{i,int} = A_{||} \sum_{is} \frac{m_{is} n_{is} v_{is,||}^3}{2} + A_{||} \frac{5eT_i}{2} \sum_{is} n_{is} v_{is,||} \tag{6.1}$$

Changes in T_e described earlier are consistent with changes in $q_{i,int}$ rather than $q_{i,kin}$. As can be seen in figure 40(b), T_e in each case starts to saturate as it drops from a few eV at the start of the detached region and approaches ≈1eV. The main difference is that while T_e saturates at ≈1eV in cases B and C, in case A it undergoes another significant reduction between the target and ∼2m from the target, dropping to ∼0.2eV. This is consistent with how $q_{i,int}$ changes as a function of parallel distance in each case, shown in figures 43(a)-(c): in case A, between $0-2$m from the target, $q_{i,int}$ undergoes a second significant reduction, falling to values that are roughly 10 and 15 times smaller than that in cases B and C.

The reduction in $q_{i,int}$ between $0\text{m}-2\text{m}$ in case A is driven by enhanced heat dissipation through $D^+ - D_2$ interactions, which only make a small net contribution to the internal energy balance across the detached region in case C - resulting in lower temperatures near the target in case A compared to case C. Changes in $q_{i,int}$ are a result of the various sources and sinks of internal energy - profiles of the net internal energy exchange through the electron and ion channels, S_e and S_i, and the net internal energy sink, $S_e + S_i$, are shown in figures 43(d)-(f). It should be noted here that (a) since S_e and S_i are internal energy sinks, they directly affect $q_{i,int}$ but not $q_{i,kin}$; and (b), the dominance of heat convection over conduction and the fact that $T_i \approx T_e$ implies that $q_{i,int} \approx q_{e,int}$ and that S_e also results in a drop in $q_{i,int}$. In fact, losses due to S_e are dominant at the start of the detached region in all cases, but weaken significantly going towards the target as the temperatures approaches 1eV. The drop in $q_{i,int}$ near the target in case A is driven by a relatively strong net internal energy sink compared to that in case C. The difference between the net internal energy sink profiles of cases A and C is due to differences in S_i. In case C, S_i weakly heats the plasma across most of the detached region; but in case A, it changes sign at ≈ 3m and becomes an increasingly strong power sink as we move towards the target. In case A, S_i drives the net power loss between $0\text{m}-2\text{m}$ (and therefore the reduction in $q_{i,int}$ and temperature). S_i is mainly composed of contributions from the following interactions: $D^+ - D$, $D^+ - D_2$ and $D_2^+ - e$. The contribution to S_i from $D^+ - D_2$ interactions is also shown in figures 43(d)-(f) for each case. It can be seen that the strong losses between $0\text{m}-2\text{m}$ in case A are driven by $D^+ - D_2$ interactions; whereas in case C, these interactions only make a small contribution to the internal energy balance.

In cases A and C, $D^+ - D_2$ interactions consist of ion-molecule elastic collisions and ion-conversion, but current code diagnostics do not allow us to directly distinguish between these two interactions. As mentioned earlier, ion-molecule elastic collisions are excluded in case B and only ion-conversion is retained. It can be seen that in this case, the $D^+ - D_2$ trace makes a contribution to S_i only at the start of the detached region - across most of the detached region, the $D^+ - D_2$ trace makes a negligible contribution to the power balance. Power loss in general is weak between $0\text{m}-4\text{m}$ from the target and consistent with the relatively constant $T_e \approx 1$eV in this region. This

suggests that ion-conversion is only active at relatively high temperatures ($T_e \geq 1$eV) and likely makes a negligible contribution to S_i between 0m $-$ 2m in case A; and that the drop in $q_{i,int}$ in this region in case A is driven mainly by ion-molecule elastic collisions. We thus conclude that increased losses to ion-molecule elastic collisions lead to the significant power loss observed between 0m $-$ 2m in case A, providing access to sub-eV temperatures and recombining conditions; and that ion-molecule elastic collisions only weakly affect $q_{i,int}$ in case C, resulting in a higher T_e.

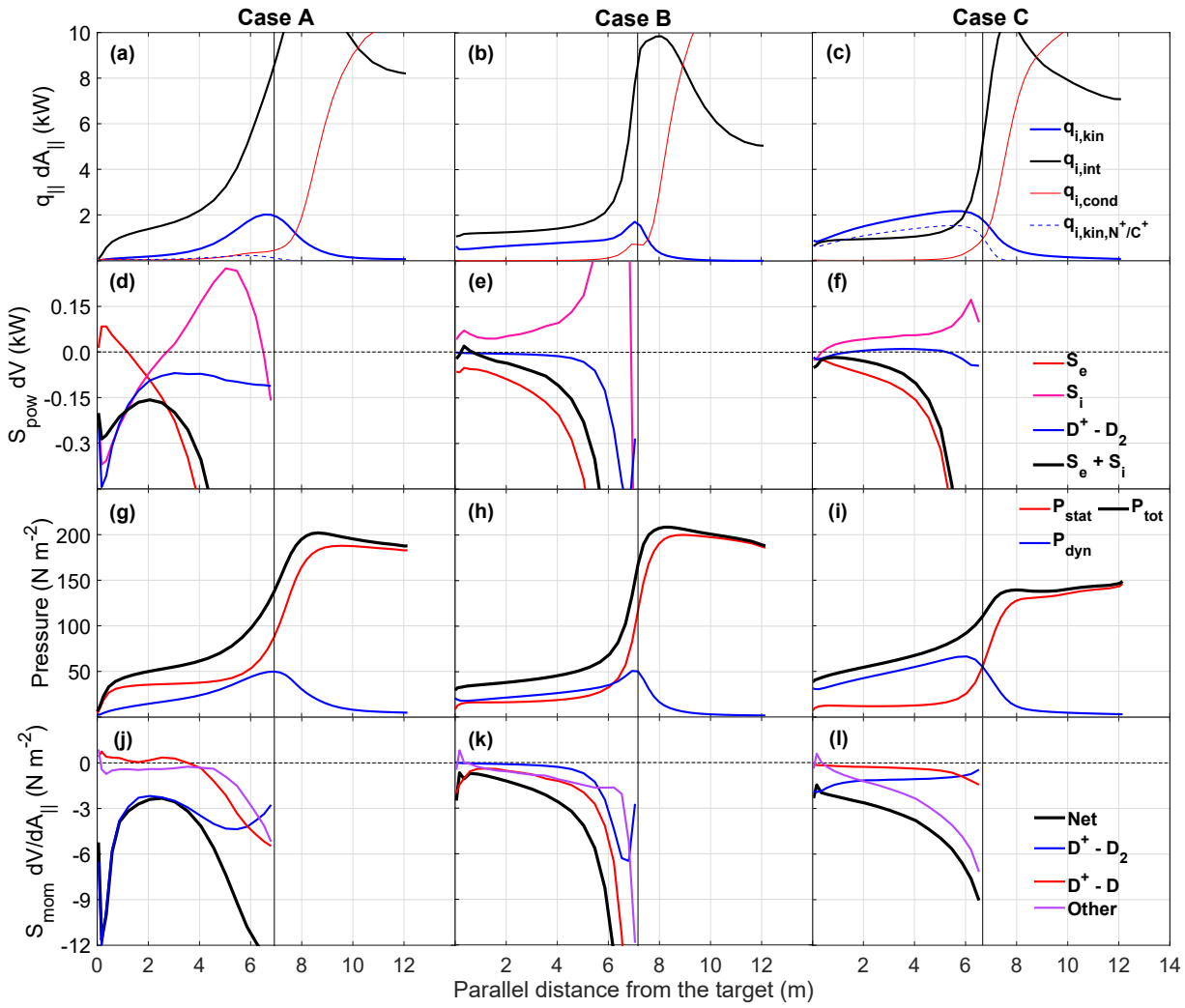

Figure 43: The impact of $D^+ - D_2$ interactions on the RHS terms of equation 6.1, $q_{i,kin}$ and $q_{i,int}$, is summarised through a power and momentum balance analysis. $q_{i,kin}$ and $q_{i,int}$ are shown in (a)-(c). Figures (d)-(f) show the power loss/gain through the ion and electron channels, S_i and S_e, the net power exchange, $S_i + S_e$ and power exchange through $D^+ - D_2$ interactions. The changes in $S_i + S_e$ result in corresponding changes in $q_{i,int}$ (and therefore in temperature). Figures (g)-(i) show profiles of P_{tot}, P_{stat} and P_{dyn}. Figures (j)-(l) provide information on the mechanisms that lead to changes in P_{dyn} and therefore $q_{i,kin}$. The kinetic energy densities associated with C^+ and N^+ (q_{i,kin,C^+} and q_{i,kin,N^+}), the most abundant impurity ion species in the detached region in cases A and C, are shown in figures (a) and (c) - most of $q_{i,kin}$ in case C is composed of q_{i,kin,N^+}.

In case C, $D^+ - D_2$ interactions are a weak power sink at the start of the detached region where the temperature is relatively high - therefore this is likely due to ion-conversion; however

between 2m − 5m, $D^+ - D_2$ interactions weakly *heat* the plasma. Ion-conversion is a D^+ sink, so this interaction should also remove the associated energy - therefore ion-conversion cannot heat the plasma. This means that it is the ion-molecule elastic collisions that are weakly heating the plasma in this region. Between 0m − 2m, $D^+ - D_2$ interactions become a weak heat sink again, this is likely also due to ion-molecule elastic collisions.

The ion internal energy balance analysis has shown that the impact of ion-molecule elastic collisions on $q_{i,conv}$ in case C is different from that in case A in at least two ways: (a) their impact on $q_{i,int}$ is significantly weaker in C as compared to that in case A; and (b) in contrast to what is seen in case A, they (very weakly) heat the plasma across a significant portion of the detached region (between 2m − 5m) in case C. Another difference with regards to how this interaction affects the plasma - which we will discuss shortly - is that (c) their impact on $q_{i,int}$ relative to that on $q_{i,kin}$ is significantly lower in case C, as compared to that in case A.

The natural question following the internal energy balance analysis is why the impact of ion-molecule elastic collisions on $q_{i,int}$ is significantly weaker in case C as compared to that in case A (leading to a higher T_e near the target in case C as compared to that in case A). In general, given the fact that the plasma and molecule densities are lower in case C (and therefore fewer ion-molecule interactions), this is expected. However, while a lower plasma and molecule density in the detached region in case C is likely an important part of the reason why ion-molecule elastic collisions only weakly affect $q_{i,int}$, this does not explain points (b) and (c). This indicates that there could be other reasons why the impact of ion-molecule elastic collisions on $q_{i,int}$ is especially weak in case C - the large f_{N^+} across the detached region in this case could be playing a role. In the following, we will carry on with our energy and momentum balance discussion and talk about the impact of the elastic collisions on $q_{i,kin}$ relative to $q_{i,int}$ in cases A and C, and then discuss how a large f_{N^+} in the detached region affects the plasma solution in case C. We will then return to the question of why the impact of ion-molecule elastic collisions on $q_{i,int}$ is significantly weaker in case C as compared to that in case A.

In cases A and C, different degrees of $q_{i,kin}$ dissipation is observed across the detached region. In case A, most of the $q_{i,kin}$ (>95%) is dissipated across the detached region and in case C, a little over half of the $q_{i,kin}$ is dissipated in the same region. The internal energy balance analysis involving figures 43(a)-(f) only gives us information on how $q_{i,int}$ is dissipated but not $q_{i,kin}$. Since $q_{i,kin}$ is effectively the product of the plasma dynamic pressure and the parallel flow velocity, a pressure balance analysis can provide some clues about how $q_{i,kin}$ is dissipated in both cases. In figures 43(g)-(i), the total, static and dynamic pressure profiles (P_{tot}, P_{stat} and P_{dyn} respectively) are shown for each case as a function of the parallel distance from the target. Note that in all cases, there is little change in P_{stat} through most of the detached region and that the reduction in

P_{tot} is largely due to P_{dyn}. Figures 43(j)-(l) show the net momentum sink, the contributions from $D^+ - D_2$ and $D^+ - D$ interactions, and the net contribution from all other mechanisms (mostly composed of losses associated with total magnetic flux expansion and radial transport). It can be seen that $D^+ - D_2$ interactions are the dominant momentum sink across most of the detached region in case A and between $0\text{m} - 2\text{m}$ in case C. In case A, losses to $D^+ - D$ interactions and other losses (which are the dominant momentum sink at the start of the detached region) weaken significantly across the detached region; and make a negligible contribution between $0\text{m} - 4\text{m}$. The significant reduction in the contribution from $D^+ - D$ interactions (charge-exchange) is likely due to a reduction in the atomic density driven by a reduction in the D_2 dissociation rate. In case C, while total/combined losses associated with total flux expansion and radial transport dominate over $D^+ - D_2$ interactions between $2\text{m} - 6\text{m}$, the contribution from $D^+ - D_2$ interactions is significant nonetheless (and in fact dominant across most of the detached region if compared to radial and total magnetic flux expansion losses individually).

As mentioned earlier, since $q_{i,kin}$ and P_{dyn} are closely related, the momentum loss decomposition (figures 43(j)-(l)) can be used to infer which process dissipates $q_{i,kin}$ - the momentum balance analysis suggests that $D^+ - D_2$ interactions again play a significant role. It should be noted that this is only valid in regions where P_{stat} is mostly constant because the momentum sinks shown do not necessarily always correspond to P_{dyn} dissipation. To calculate exactly how much $q_{i,kin}$ is dissipated by $D^+ - D_2$ interactions, we first identify the region across which there is little change in P_{stat}: this is between $\approx 2\text{m} - 5\text{m}$ in case A and $\approx 0\text{m} - 5\text{m}$ in case C. Since the net momentum loss, momentum loss due to $D^+ - D_2$ interactions and the total change in $q_{i,kin}$ are known, the fraction of momentum lost to this interaction can be used to calculate the contribution of this interaction in $q_{i,kin}$ dissipation. The fraction of the total P_{dyn} dissipated, $\int_a^b S_{P_{dyn,tot}} dV$, by ion-molecule interactions, $\int_a^b S_{P_{dyn,mol}} dV$, between the downstream end of the region where the P_{stat} is roughly constant, point a, and the upstream end of this region, point b, is equal to the fraction of the total $q_{i,kin}$ dissipated across this region, $\int_a^b S_{kin,tot} dV = q_{i,kin,b} - q_{i,kin,a}$, by ion-molecule interactions $\int_a^b S_{kin,mol} dV$:

$$\frac{\int_a^b S_{P_{dyn,mol}} dV}{\int_a^b S_{P_{dyn,tot}} dV} = \frac{\int_a^b S_{kin,mol} dV}{\int_a^b S_{kin,tot} dV} \tag{6.2}$$

In other words, the amount of $q_{i,kin}$ dissipated through ion-molecule interactions is simply:

$$\int_a^b S_{kin,mol} dV = (q_{i,kin,b} - q_{i,kin,a}) \frac{\int_a^b S_{P_{dyn,mol}} dV}{\int_a^b S_{P_{dyn,tot}} dV} \tag{6.3}$$

The $q_{i,kin}$ dissipated by $D^+ - D_2$ interactions in cases A and C integrated across the regions considered is shown in figure 44. This is compared with the corresponding $q_{i,int}$ dissipated through

$D^+ - D_2$ interactions. In case A, the $q_{i,kin}$ dissipated by $D^+ - D_2$ interactions is more than twice that in case C. Fewer ion-molecule interactions due to lower plasma and molecule densities is likely the reason for the relatively weak $q_{i,kin}$ dissipation in case C. Importantly, it can be seen that relative to $q_{i,kin}$ dissipation, $q_{i,int}$ dissipated by ion-molecule interactions is significantly lower in case C - in general this can also be seen in figure 43 but it is quantified in figure 44. The ratio of $q_{i,int}$ dissipated to $q_{i,kin}$ by this interaction across the regions considered is ≈ 0.64 in case A whereas in case C it is ≈ 0.12. This is partly because this interaction heats the plasma between $2\text{m} - 5\text{m}$ in this case; but in general, the impact on $q_{i,int}$ is weak compared to the impact on $q_{i,kin}$ in case C.

Exactly how the split between $q_{i,int}$ and $q_{i,kin}$ dissipated through each ion-molecule interaction is calculated is not clear, however, there appears to be general a preference to dissipate $q_{i,kin}$ as opposed to $q_{i,int}$. Consider case A. Between $2\text{m} - 5\text{m}$, the amount of $q_{i,int}$ available to dissipate is significantly higher than the amount of $q_{i,kin}$ available to dissipate, yet the amount of $q_{i,kin}$ dissipated in this region by $D^+ - D_2$ interactions is significantly higher than the $q_{i,int}$ dissipated. In fact, most of the $q_{i,kin}$ available to dissipate is dissipated between $2\text{m} - 5\text{m}$ in case A, and between $0\text{m} - 2\text{m}$, since there is little $q_{i,kin}$ left to dissipate, ion-molecule elastic collisions mainly dissipate $q_{i,int}$. So in addition to the lower plasma and molecule density across the detached region in case C, it is possible that such a preference to dissipate $q_{i,kin}$ may also be contributing to the observed weak impact of ion-molecule elastic collisions on $q_{i,int}$ since $q_{i,kin} > q_{i,int}$ across most of the detached region in this case.

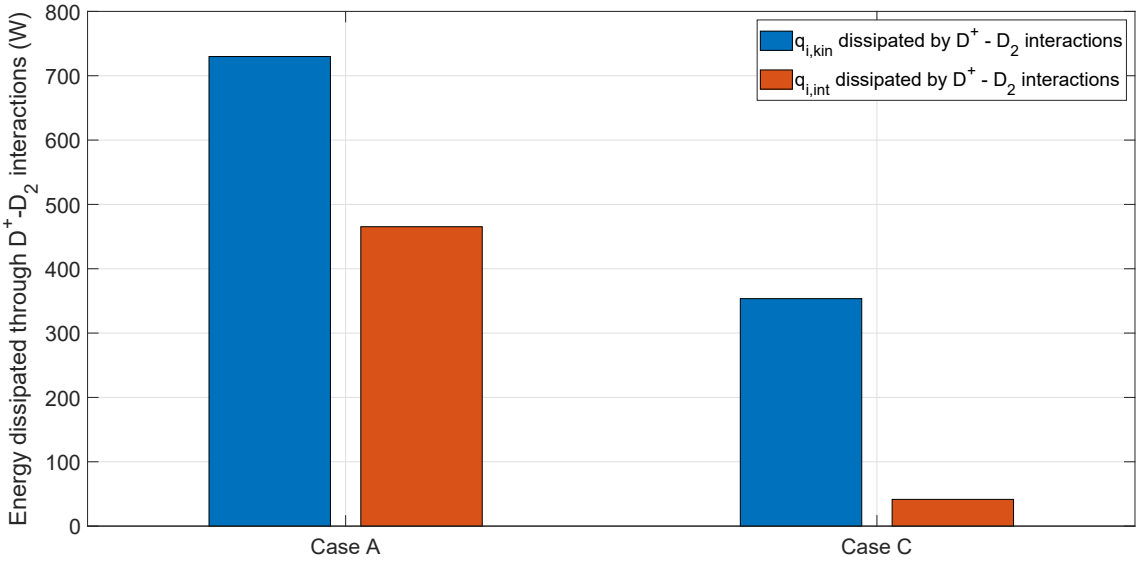

Figure 44: Comparison of $q_{i,kin}$ dissipated by $D^+ - D_2$ interactions (calculated using equation 6.3) and $q_{i,int}$ dissipated by the same between $2\text{m} - 5\text{m}$ for case A and $0\text{m} - 5\text{m}$ for case C. It can be seen that $q_{i,int}$ dissipated by this interaction relative to the $q_{i,kin}$ dissipated by the same is significantly lower in case C as compared to case A.

Note that in case C, a large fraction of the plasma in the detached region is composed of nitrogen ions, $f_{N^+} \approx 0.4$ (figure 42). Since nitrogen is seven times heavier than deuterium, most of the kinetic energy is actually carried by N^+, as can be seen in figure 43(c) in which the $q_{i,int}$ carried by N^+ alone is also displayed. In fact, this is the reason why $q_{i,kin} > q_{i,int}$ across most of the detached region in case C. However, N^+ does not interact with the molecules in our model - in the next part of this discussion, we will show how the N^+ part of the plasma across the detached region in case C loses energy even though it does not directly interact with the molecules; and more generally, discuss the impact of a large f_{N^+} across the detached region on the plasma solution.

6.3.2 Impact of a large f_{N^+} on the energy and momentum balance

As mentioned above, the N^+ part of the plasma fluid does not interact with any neutrals in our model. In this part of the discussion, through an individual momentum balance analysis of D^+ and N^+, we will show that the nitrogen ions lose energy/momentum through friction with the D^+ fluid which does interact with the neutrals. Even though the nitrogen does not directly interact with the neutrals, the plasma fluid in the detached region loses energy/momentum as a whole through a $D_2 - D^+ - N^+$ interaction chain.

The poloidal momentum flux density associated with D^+ and N^+ is shown as a function of the parallel distance from the target in figures 45(a) and (b) respectively and the corresponding momentum source decomposition across the detached region is shown in figures 45(c) and (d). It can be seen that most of the momentum is actually carried by N^+ and not D^+, consistent with the observation in figure 43(c). The N^+ fluid is created in the downstream half of the thermal front where a steep static pressure gradient exists, so it undergoes a strong acceleration towards the target as soon as it is created across the interface between the thermal front and the detached region. In the momentum balance for N^+, the momentum loss is primarily driven by ion friction; other losses (mainly radial transport) weaken significantly as we move towards the target. Since most of the plasma in this region is composed of D^+ and N^+ (figure 42), the momentum exchange associated with ion friction is primarily through $D^+ - N^+$ friction. In the D^+ momentum balance, across most of the detached region, the contributions from $D^+ - D$ interactions, static pressure gradient and the net contribution from all other losses are small. The net momentum sink for D^+ is primarily a balance between losses due to D_2 interactions and momentum gain due to ion friction - while there is a relatively large momentum sink associated with $D^+ - D_2$ interactions, a lot of this 'lost' D^+ momentum is actually regained through friction with N^+. This results in a relatively small net momentum sink and only a small drop in the D^+ poloidal momentum flux is observed. Note that the momentum exchange associated with ion friction in figure 45(d) is roughly equal and opposite in figure 45(c) - roughly the same amount of momentum is gained by

D^+ through ion friction as is lost from N^+. This shows that in case C, while molecules don't act directly on a large fraction of the plasma, the momentum from the whole plasma fluid across the detached region is lost through a $D_2 - D^+ - N^+$ interaction chain.

Just as the strongly accelerated N^+ acts like a reservoir of momentum for the D^+, it is likely that a similar effect is playing a role when it comes to the internal energy. In these simulations, the ion temperature is equal for all ion species. As with the momentum balance, since N^+ does not directly interact with the molecules, it can only lose heat through frictional interaction with D^+. Thus, the N^+ fluid acts like a reservoir of heat or temperature, effectively weakening the impact of ion-molecule elastic collisions on $q_{i,int}$.

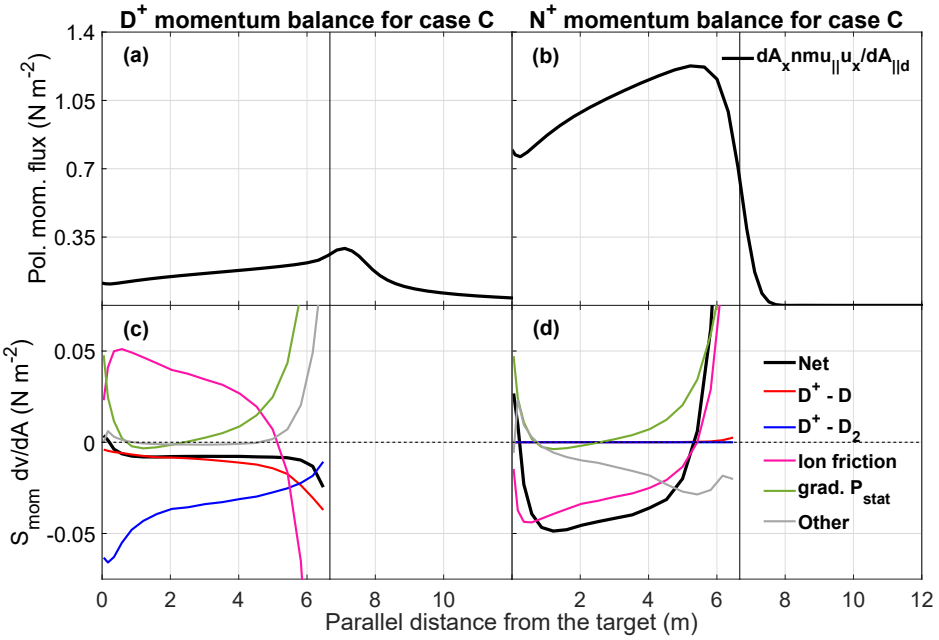

Figure 45: Momentum balance analysis of D^+ and N^+ in case C - (a) and (b) show the poloidal momentum flux density associated with each species, and (c) and (d) show a decomposition of momentum sinks. $D^+ - D_2$ interactions are the dominant D^+ momentum sink but a lot of the lost momentum is regained through ion-friction. Ion friction makes a roughly equal and opposite contribution to the N^+ momentum balance, where it is the dominant momentum sink.

Another important consequence of the fact that a large amount of N^+ is created in the cold end of the thermal front and strongly accelerated by the steep static pressure gradient into the detached region is that at some point, because of the nitrogen mass, we find that $P_{dyn} > P_{stat}$ (figure 43(i)). In other words, the plasma goes supersonic as it enters the detached region in case C. More specifically, the plasma flow velocity as it enters the detached region is higher than the collective sound speed of all species, $c_{s,collective}$, which is defined as:

$$c_{s,collective} = \sqrt{\frac{n_e e T_e + \sum_{is} n_{is} e T_i}{\sum_{is} m_{is} n_{is}}} \tag{6.4}$$

The combined effect of the nitrogen mass and a large f_{N^+} is a significantly lower $c_{s,collective}$. This can be seen in figure 46 in which the sound speed profiles of the different ion species (D^+, C^+ and N^+) are displayed along with the $c_{s,collective}$ profile for each case. It can be seen that even though carbon is a lot heavier than deuterium, $c_{s,collective} \approx c_{s,D^+}$ in cases A and B due to a relatively small f_{C^+}; and due to a large f_{N^+} in case C, it can be seen that $c_{s,collective} \approx c_{s,N^+}$.

The key point here is that the plasma across the detached region that the neutrals in case C interact with, in sharp contrast to case A, is actually more comparable to an 'ion beam'. The potential implications of this on how ion-molecule elastic collisions affect the solution in this case will be described further in section 6.3.3.

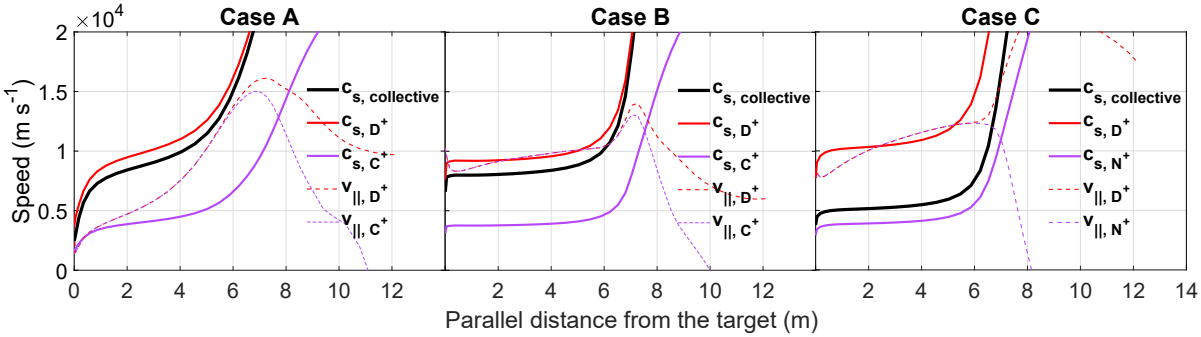

Figure 46: Sound speed profiles of D^+ and the most abundant impurity species in the divertor for each case compared to their corresponding parallel flow velocities. These are also compared to the collective sound speed for all species. In cases B and C, the plasma across the detached region is supersonic.

As an aside, it is useful at this stage to discuss an interesting and important aspect of the solutions presented in this paper: the momentum boundary condition chosen for the sheath is $v_{||,is} \geq c_{s,is}$. Since T_i is the same for all ion species in our simulations, this means that the minimum value of $v_{||,is}$ imposed at the sheath is necessarily different for ion species of different mass. For the solutions in case C, the mass difference between deuterium and nitrogen implies that a significantly different minimum value of $v_{||,is}$ is imposed on almost half the plasma at the sheath since $f_{N^+} \approx 0.4$ here. Figure 46 also shows the parallel flow velocity profiles of D^+ and the most abundant impurity ion species in the detached region in each case. As discussed earlier, while the N^+ fluid does not interact with D_2, it 'feels' their presence as a frictional drag with the D^+ fluid which loses momentum to D_2 through elastic collisions. The majority (but not all) of the momentum lost by the D^+ fluid is regained through friction with the N^+ fluid. The steady solution is consistent with the plasma fluid as a whole losing momentum through the $D_2 - D^+ - N^+$ interaction chain, with ion friction distributing the momentum loss across the plasma fluid such that the $v_{||,is}$ of all ion species is approximately (but not exactly) equal. So as a result, while the chosen boundary condition implies $v_{||,is} \geq c_{s,is}$ at the sheath, the ion friction appears to result in all plasma species satisfying the minimum $v_{||,is}$ condition on the lightest component of the fluid

(because this will have the highest sound speed). A boundary condition in which one that sets $v_{||,is} \geq c_{s,collective}$ at the sheath for any given ion species would perhaps be more realistic. However this option is currently not available. The other available option for the momentum boundary condition at the sheath is that $v_{||,is}$ is *equal* to $c_{s,collective}$. Since f_{C^+} across the detached region is relatively small in cases A and B, the chosen boundary conditions are reasonable in these cases. However due to the large f_{N^+} in case C, changing the boundary condition to $v_{||,is} \geq c_{s,collective}$ (if this option was available) could considerably change the solution. More work is needed to identify the correct boundary condition for such a scenario.

6.3.3 Possible reasons for the differences in the impact of $D^+ - D_2$ elastic collisions on $q_{i,int}$ between cases A and C

Having discussed some of the key aspects of how $D^+ - D_2$ elastic collisions and a large f_{N^+} affect the energy and momentum balance, we now return to the question of why the impact of the elastic collisions is significantly weaker in case C. We have seen from the internal energy balance analysis that the impact of ion-molecule elastic collisions on $q_{i,int}$ is weak across the detached region in case C. As mentioned earlier, this is generally expected due to the lower plasma and molecule density across the detached region in this case. However, as demonstrated through the pressure balance analysis, we found that the impact of the elastic collisions on $q_{i,kin}$ is actually not as weak, suggesting that there could be other mechanisms that result in the rather weak impact on $q_{i,int}$ and thus leading to a higher T_e in case C. Further, we also noted that there appears to be a general preference for the elastic collisions to dissipate $q_{i,kin}$ rather than $q_{i,int}$; and since $q_{i,kin} > q_{i,int}$ across the detached region in case C, we identified this preference as a potential reason for the rather weak impact of the elastic collisions on $q_{i,int}$ in this case. Next, we saw that the high $q_{i,kin}$ in case C is a consequence of the large f_{N^+} across the detached region, and that the multifluid plasma as whole loses momentum (and therefore $q_{i,kin}$) through a $D_2 - D^+ - N^+$ interaction chain. We also noted that since the ion temperature is the same for all the species, the N^+ likely acts like a reservoir of heat or temperature, effectively weakening the impact of the elastic collisions on $q_{i,int}$ in yet another way. Lastly, we noted that another consequence of the large f_{N^+} in case C is that the plasma goes supersonic as it enters the detached region, and that the molecules essentially interact with a 'plasma beam' in this case.

Exactly how the energy exchange in an ion-molecule elastic collision is split between $q_{i,int}$ and $q_{i,kin}$ remains unclear - in particular, (a) why there appears to be general preference to dissipate $q_{i,kin}$ rather than $q_{i,int}$ and (b) why the elastic collisions in case C heat the plasma in some places and cool it in other places remain unanswered questions. The energy and momentum exchange associated each ion-molecule elastic collision is calculated as follows: The pre-collision

position and velocity vectors of D_2 are known, and the corresponding velocity vectors of D^+ are obtained by sampling the associated drifting maxwellian distribution at that position. A simple 'billiard ball' collision is then simulated and the post-collision velocities are obtained through energy and momentum balance. For the D^+, the post-collision velocity will have a new parallel-to-B component, $v_{||,D^+}$, that will be used to calculate the change in $q_{i,kin}$; and also a new 'random' thermal component, v_{th,D^+}, associated with temperature (and internal energy) that will used to calculate changes in the maxwellian distribution and therefore $q_{i,int}$.

The basic picture in the detached region in these simulations is as follows: a fast flowing plasma (mostly D^+ in case A and a significant f_{N^+} in case C) interacts with a relatively stationary D_2 cloud through elastic collisions (and also ion friction in case C). In such a scenario, it is plausible that the change in $v_{||,D^+}$ is actually is proportional to $v_{||,D^+}$ itself. In other words, the faster the plasma flows through the D_2 cloud, the larger the drag it experiences. This could potentially explain the apparent preference to dissipate $q_{i,kin}$ as opposed to $q_{i,int}$.

The impact of elastic collisions on internal energy would depend on the difference between the pre-collision and post-collision 'random' velocity component of D^+ - if the post-collision v_{th,D^+} is larger than the corresponding pre-collision value, then this would represent a source of heat because an increase in v_{th,D^+} means an increase in temperature. This could occur in scenarios where $v_{||,D^+} > c_{s,D^+}$ - where the plasma is more like a beam of ions. As mentioned earlier, this is the situation in case C - the relatively stationary D_2 cloud essentially interacts with a beam of plasma with a very narrow maxwellian distribution. In such a scenario, it is plausible that the such an interaction would lead to the 'thermalisation' of the 'beam' - making ion-molecule elastic collisions a source of heat in some regions in case C.

To summarise, figure 43 suggests that as the temperatures approach 1eV, plasma-neutral energy/momentum exchange weakens through all channels except ion-molecule elastic collisions:

- Comparison of case A and B shows that ion-molecule elastic collisions are necessary to observe a significant drop in temperature below 1eV
- In case C, even though ion-molecule elastic collisions are present, their impact is weakened and a significant drop in temperature below 1eV not observed

We believe that the weak impact of ion-molecule elastic collisions in case C is due to the following:

- Fewer ions and molecules - fewer interactions and less energy exchange
- Almost half the plasma across the detached region is nitrogen, this could weaken the impact of ion-molecule interactions in two ways:

1. Nitrogen is seven times heavier than deuterium. The presence of a large amount of nitrogen results in $q_{i,kin} > q_{i,int}$ across the detached region, which we hypothesise weakens the impact of ion-molecule elastic collisions on $q_{i,int}$.
2. Since molecules do not interact with nitrogen which makes up almost half the plasma in these simulations, their impact on heat dissipation and temperature is weakened - the nitrogen acts like a 'temperature reservoir'.

6.3.4 Impact of $D^+ - D_2$ elastic collisions on divertor n_e profiles

We have now seen that the access to sub-eV temperatures through $D^+ - D_2$ elastic collisions near the target in case A is an important factor that results in high recombination levels in this case. However, the higher density near the target in this case also significantly enhances the recombination levels. In fact, an important observation in this comparison is that there is a qualitative difference between the density profile in case A and that in case C. In case A, the density increases significantly across the detached region and peaks close to the target whereas in case C, there is little change in the density across the detached region. While turning off $D^+ - D_2$ elastic collisions leads to higher temperatures near the target, it also results in a density profile that is mostly flat across most of the detached region like in case C and thus lower densities near the target. In this last part of our discussion on $D^+ - D_2$ elastic collisions, we will describe the impact of these elastic collisions on the divertor density profiles.

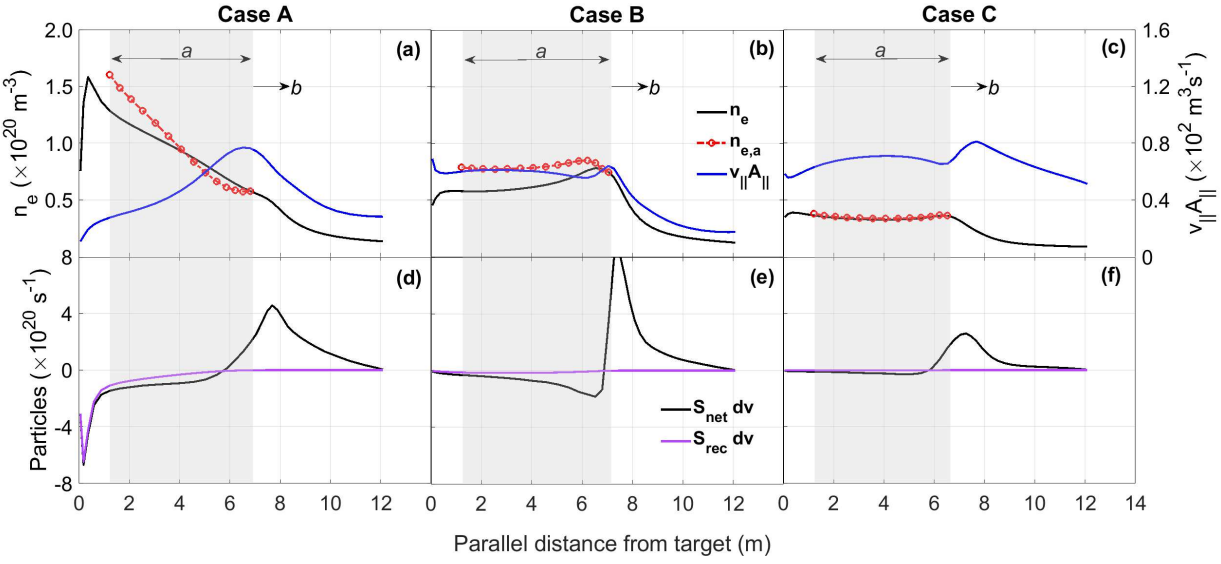

Figure 47: Particle balance analysis across the detached region for each case. Figures (a)-(c) show the electron density profile, and the product of the parallel flow velocity and flux tube cross-section area. The net particle sink and the recombination sink are shown in figures (d)-(f), equation 6.5 is applied in the grey region where the S_{net} is relatively small. It can be seen that the qualitative features of n_e are reproduced by equation 6.5 which shows that the increase in density across the divertor in case A is due to $D^+ - D_2$ interactions driving a strong reduction $v_{||}$.

The n_e profile as a function of the parallel distance from the target is shown for each case in figure 47(a)-(c). As mentioned above, there is a qualitative difference between the density profile in case A and the ones in cases B and C - between the start of the detached region and 1m from the target (shown in grey), there is a slight increase in n_e in case C and a small drop in case B, but the profiles remain mostly flat. But in case A, n_e increases strongly across this region (by $\approx 120\%$).

The reason for the observed difference can be understood as follows: The density profile along a single flux tube is determined by the net particle source and the flow velocity. If we consider point a to be anywhere between 1m from the target and the start of the detached region, and point b to be at the start of the detached region, then according to particle balance, the electron density at a, $n_{e,a}$, is related to that at b, $n_{e,b}$, through $v_{||}$ and the cross-sectional areas ($A_{||}$) at those points, and the net particle source ($S_{n,net}$) integrated between those points:

$$n_{e,a} = \frac{n_{e,b} v_{||,b} A_{||,b} + \int_a^b S_{n,net} dv}{v_{||,a} A_{||,a}} \tag{6.5}$$

In figures 47(d)-(f), the S_{rec} profiles and the net volumetric particle source profiles, $S_{n,net}$ are shown for each case. Firstly, it can be seen that in all cases, $S_{n,net}$ is relatively small across most of the grey region - if $S_{n,net} \approxeq 0$ between a and b, then equation 6.5 becomes

$$n_{e,a} \approxeq \frac{n_{e,b} v_{||,b} A_{||,b}}{v_{||,a} A_{||,a}} \tag{6.6}$$

Equation 6.6 suggests that $n_{e,a} > n_{e,b}$ if the product $v_{||,a} A_{||,a} > v_{||,b} A_{||,b}$ (and vice-versa). Profiles of $v_{||} A_{||}$ as a function of parallel distance from the target are shown in figures 47(a)-(c) - these correspond to $v_{||,a} A_{||,a}$ in the grey region and $v_{||,b} A_{||,b}$ at point b. Across the grey region, $v_{||} A_{||}$ drops dramatically (by over $\approx 60\%$) in case A and changes by less than 10% in the other two cases. These changes are consistent with changes in the density. In fact, the $v_{||}$ and $A_{||}$ profiles are indeed sufficient to reproduce the qualitative features of the density profiles in the grey region, $n_{e,a}$, also shown in 47(a)-(c). Since the simulation geometry is the same in all cases, the $A_{||}$ profile between a and b (or anywhere) is also the same. The differences in the n_e profiles across the grey region must therefore result primarily from differences in the $v_{||}$ profile in that region. Figure 47 demonstrates that the significant increase in n_e observed across the detached region in case A is primarily a result of a corresponding reduction in $v_{||}$, and that ion-molecule elastic collisions are necessary for this strong reduction to occur. A similar reduction in $v_{||}$ is not observed in case C even though ion-molecule elastic collisions are included here is again because of the large impurity fraction. As seen in figure 45, most of the momentum in case C is carried by N^+; because of the plasma across the detached region in case C is a lot heavier than that in case A, even a similar

reduction in the dynamic pressure in both cases will lead to a relative smaller reduction in the flow velocity in the case with the heavier plasma.

In summary, ion-molecule elastic collisions essentially 'plug' the plasma flow across the detached region in case A, leading to a density profile that is strongly peaked near the target. However, this 'plugging' of the plasma flow is not as efficient in case C because the seven times heavier nitrogen makes up a significant portion of the plasma, resulting in a relatively flat density profile.

6.4 Conclusions

The SOLPS-ITER code package was used to perform a deuterium fuelling scan and a nitrogen seeding scan (at a constant fuelling rate) in the MAST-U Super-X geometry and obtain strongly detached solutions. The aim was to carry out a detailed comparison of conditions when the divertor is strongly detached due to a high upstream density to those when it is a result of significantly increased impurity radiation at a relatively low upstream density. The key difference between the two scans was in the role of volume recombination in the reduction of the particle flux to the target. In the seeding scan, the reduction in particle flux was primarily due to a reduction in the divertor ionisation source with volume recombination playing a negligible role. In contrast, volume recombination was found to play a key role in target particle flux reduction in the fuelling scan. This was due to a combination of significantly lower ($\leq$ 1eV) temperatures near the target and significantly higher divertor plasma densities achieved in the fuelling scan compared to the seeding scan. Further, we observed a qualitative difference in the divertor density profiles of the most strongly detached solutions obtained in the two scans. While the density in the fuelling case increased significantly across the divertor, peaking near the target, the divertor density profile in the nitrogen seeded case was mostly flat. Qualitative features of the strongly detached solution from the seeded case (higher temperatures, flat divertor density profile and therefore negligible recombination) were recovered in the fuelling scan by turning off $D^+ - D_2$ elastic collisions and repeating the scan, demonstrating that this interaction is necessary to access strongly recombining conditions in the fuelling scan for the simulated parameter space. In order to better understand the role of $D^+ - D_2$ elastic collisions, a strongly detached case was chosen from each of the three scans and an energy, momentum and particle balance analysis was performed on each case.

Analysis showed that in the fuelling case, energy and momentum loss to $D^+ - D_2$ elastic collisions are enhanced as a result of higher divertor plasma and neutral densities, and therefore more plasma-neutral interactions. In particular, important heat dissipation mechanisms like impurity radiation and hydrogenic excitation/ionisation were found to weaken significantly as the temperatures approach 1eV and $D^+ - D_2$ elastic collisions play the key role in removing heat from the

plasma to access sub-eV temperatures. Further, it was found that in the fuelling case, a relatively large plasma flux flows into the detached region and towards the target while interacting with a relatively dense cloud of deuterium atoms and molecules. Primarily through $D^+ - D_2$ elastic collisions, this cloud 'plugs' the plasma flow across the detached region, i.e. there is a significant reduction in the plasma flow velocity along the field. Due to a relatively small net particle sink across most of the detached region, we observe a steady increase in plasma density across this region. These interactions also appear to keep most of the molecules 'squashed' to the target, as indicated by the sharp increase in molecular density close to the target. Coupled with the already high plasma density, this sharp increase in molecule density close to the target drives strong power losses to $D^+ - D_2$ elastic collisions, leading to sub-eV temperatures and increased volume recombination across this region. Excluding this important loss mechanism from the simulations has a strong impact on the solutions: even though the plasma flux entering the detached region is similar and the density of the neutral cloud across the detached region is actually higher, the plasma flows freely across the detached region, there is no significant change in the plasma flow velocity, the molecules are not 'squashed' near the target and there is no significant power loss to molecules. This coupled with no significant particle source across the detached region, results in a mostly flat density profile and no significant reduction in temperature beyond 1eV, and therefore negligible volume recombination.

The plasma flux entering the detached region in the seeded case is half that in the fuelling case, and it interacts with a neutral cloud of significantly lower density. In addition, singly ionised nitrogen makes up almost half the plasma across the detached region and therefore carries a large fraction of the plasma momentum because of its mass and also does not interact with the neutrals in these simulations. Through friction with nitrogen ions, deuterium ions regain most of the momentum lost to interactions with neutrals. The nitrogen ions essentially 'drag' the divertor plasma through a relatively low density neutral deuterium cloud, without interacting with the nitrogen atoms. The combined result of a heavy plasma flowing through a low density neutral cloud is that the plasma flow is not 'plugged' as effectively as in the fuelling case - the reduction in plasma flow velocity across the divertor is therefore not as strong as compared to that in the fuelling case. Again, the net particle source is small across most of the detached region, and the relatively small changes in the flow velocity across the detached region result in a flat density profile. As in the fuelling case, the molecules are 'squashed' close the target in the seeded case as well - the molecule density increases sharply close to the target. While this increase in molecule density is indeed accompanied by an increase in power losses to $D^+ - D_2$ elastic collisions in the seeded case, this is not as strong and the temperature in this case does not drop significantly below 1eV. The lower plasma and neutral densities correspond to fewer plasma-neutral interactions and

therefore lower heat dissipation. Further, the presence of a large amount nitrogen likely weakens the actual impact of $D^+ - D_2$ elastic collisions on the internal energy in two ways. First, $D^+ - D_2$ elastic collisions appear to preferentially dissipate directed kinetic energy as opposed to internal energy. The large amount of nitrogen results in the plasma having a significantly higher directed kinetic energy, weakening the impact of the elastic collisions on the internal energy. Second, all ion species have the same temperature and the only way nitrogen ions can lose heat is through friction with the main ions. The nitrogen therefore acts like a reservoir of heat which again results in $D^+ - D_2$ elastic collisions having a rather weak impact on the plasma internal energy. Thus, the plasma temperature across the detached region does not drop significantly below 1eV. The combined result of a relatively low plasma density and a high plasma temperature is negligible recombination.

In reality, impurity neutrals would interact with both the main ions and impurity ions. In the case of nitrogen seeding, nitrogen molecules and ammonia would also exist and interact with the plasma ions through charge-exchange and elastic collisions. The strong impact of $D^+ - D_2$ elastic collisions on the fuelling case indicates that including elastic collisions between impurity neutrals and plasma ions could significantly change the solution in the seeding case. Equivalently, another interpretation of this result is that given the qualitative features of the seeding case are recovered in the fuelling case by excluding $D^+ - D_2$ elastic collisions which is a key loss mechanism, the seeding scan is likely missing an important loss mechanism or mechanisms. In particular, this result suggests that in long-legged divertors in which the detachment front can move a significant distance away from the target, or at least in the Super-X configuration studied here, the use of fixed impurity fraction models is not sufficient to model strongly detached conditions - this is because while fixed fraction impurity models may sufficiently capture radiative power loss, the concentration of impurity ions can be significantly higher in the detached region where the corresponding radiation may be negligible; and these impurity ions can be make a significant contribution to the momentum balance which would not be captured in fixed fraction impurity models. Finally, analysis of the local sound speed of the different species at the target suggests that in high impurity concentration scenarios like the one studied here, a boundary condition that imposes a (very) different minimum velocity on different species may not be appropriate. In such scenarios, a boundary condition that imposes the collective sound speed of all species as the minimum parallel velocity may be more appropriate and could change the solution significantly. However, more work is required to address this issue in general.

Chapter 7

Summary and future work

The SOLPS-ITER code package has been used to study impurity radiation driven and upstream density driven detachment in the MAST-U Super-X geometry. The main aims of this study were:

- To study the evolution of the divertor plasma characteristics from detachment onset through to stongly detached conditions and to investigate the role of parallel B field gradients in detachment control, the core characteristic of the Super-X
- To carry out a detailed comparison of conditions when the divertor is detached due to a high upstream density to those when it is a result of significantly increased impurity radiation at a relatively low upstream density

With these aims in mind, two parameter scans were performed at fixed input power to study the steady state divertor plasma characteristics from detachment onset through to strongly detached conditions. In the first scan, the main ion (D_2) fuelling rate was varied to obtain a scan in the outboard midplane density, n_u. In the second scan, the nitrogen impurity fraction in the SOL/divertor, f_N, was scanned by varying the seeding rate of nitrogen atoms (N) at a fixed fuelling rate. Carbon was included as a sputtered impurity in both scans. The role of parallel B field gradients in detachment control is investigated by tracking the movement of different measures of the detachment location in two characteristic flux tubes as a function of the fuelling and seeding rates, and the physics control parameters. The strongly detached solutions are compared by performing a detailed energy, momentum and particle balance analysis in the divertor region of a characteristic flux tube.

Two key observations observations were made, described in chapter 4. Movement of the various detachment location markers in both scans was observed to be qualitatively similar. In both scans, following detachment onset, the detachment front location quickly moves upstream towards the X-point for small changes in the N seeding or D_2 fuelling rate, but slows down as it moves through a region of increasing dB/dz which is also close to the divertor entrance. Even after a $10\times$ and $5\times$

increase in the seeding and fuelling rates past the detachment threshold, the detachment front only reaches less than halfway to the X-point in l_{pol} where dB/dz is ∼50% of its maximum value, in stark contrast to what is normally observed in experiments. On the other hand, important differences in the divertor conditions were observed in the comparison of strongly detached solutions. The fuelling scan achieved higher divertor densities and lower target temperatures compared to the seeding scan. As a result, volume recombination was found to play an important role in the reduction of the particle flux to the target; whereas volume recombination was negligible throughout the seeding scan. A qualitative difference in the divertor density profiles was also observed. Qualitative features of the seeding scan were recovered in the fuelling scan by turning off ion-molecule elastic collisions, demonstrating the strong impact of this interaction on the divertor conditions.

Analysis performed to interpret the first main result, the slowing down of the detachment location markers, was the subject of chapter 5. The SOLPS results were compared to the predictions of the detachment location sensitivity (DLS) model. Using only energy balance and making a number of simplifying assumptions, the DLS model predicts the detachment front location as function of three physics control parameters: the outboard midplane density, the impurity fraction in the scrape-off layer and the power entering the divertor. Both the DLS model and SOLPS simulations predict that the sensitivity of the detachment front location along a field line, z, to control parameters would reduce in a region of high dB/dz for the MAST-U Super-X configuration. The qualitative agreement between the DLS model predictions and the SOLPS results suggests that the strong parallel gradients in the divertor B field should enable the MAST-U Super-X configuration to provide improved detachment control. This also indicates that larger power transients may be accommodated in the Super-X divertor compared to a conventional divertor while still keeping the divertor plasma detached with the detachment front kept away from the X-point or target. However, the temporal response of the thermal front to control parameter fluctuations as not been studied in this work - the results described here motivate further studies to explore this aspect using simpler models like SD1D [148].

The extent of the high dB/dz region changes significantly when examined in l_{pol} space compared to that in z space. In z space, the high dB/dz region only occupies ∼15-20% of the distance along z from target to X-point position. On the other hand, in l_{pol} space, the high dB/dz region takes up ∼40% fraction of the distance between the target and the X-point, which translates to a milder reduction in front location sensitivity in poloidal space for the Super-X geometry considered. If the DLS model does properly reflect the underlying physics of front sensitivity, then we could expect a stronger reduction in sensitivity in poloidal space if the parallel gradients were stronger. It is therefore of interest to repeat this study in divertor geometries where such regions exist. There may be scope to significantly increase or steepen the parallel gradient in B in the existing location

by increasing the magnitude of the poloidal field in region of high parallel gradients. Future work could focus on studying the extent to which to the Super-X geometry studied here could be optimised in this way. There appears to be limited flexibility when it comes to optimising the poloidal location or extent of the region of high parallel gradients in this geometry. It is therefore of interest to fully explore this aspect to understand what is practically possible in realistic divertor geometries.

The main quantitative mismatch between SOLPS and DLS model predictions of the detachment front location sensitivity to control parameter variation is that the DLS model, for the same control parameter variation, predicts a faster upstream movement of the detachment front in the region of low dB/dz near the target after detachment onset compared to SOLPS results. A number of possible reasons for this lack of quantitative agreement were identified. The fact that DLS model assumes the thermal front width to be small compared to the divertor size and that plasma-neutral pressure balance is not considered are likely to be the important sources of disagreement. It is possible that the assumption of a thin thermal front may be maybe satisfied when the model is applied to reactor-level parallel heat fluxes, but further work is needed to understand the dependence of the thermal front width on the power entering the divertor and on the impurity (or impurities) chosen to dissipate that power. However, the effect of incorporating plasma-neutral pressure balance into the model on the predictions is very likely to be relevant in reactor like scenarios as well as in low power scenarios like the one considered in this work - this could provide some clues about the impact of neutral compression on the front movement in a tightly baffled divertor like the one studied here. These differences also motivate further work using models like SD1D to study at the impact of the power entering the divertor and plasma-neutral pressure balance on the thermal front width and movement.

It has already been shown that the baffle has a significant impact on the access to detachment [75]. It is possible that maintaining plasma-neutral pressure balance in a tightly baffled divertor could also be contributing to the reduction in the front location sensitivity to controls, in addition the parallel gradients in B. This naturally gives rise to the question of which effect is playing the dominant role, which has not been addressed in this study, and strongly motivates future work to focus on disentangling the relative contributions of these two effects. The potential impact of the baffle on the existing solutions can be also be studied by modifying the divertor wall geometry or placing virtual surfaces or removing the baffle altogether and allowing the solutions to evolve to a new steady state. SOLPS studies in simplified geometries could also help disentangle the potential impact of the baffle from that of dB/dz. Indeed, if the baffle happens to be playing the dominant role, it can be argued that just having a tighly baffled divertor is the simpler solution, and that the details of the divertor magnetic geometry are less important in the context of detachment

control. However, in order to properly start addressing this question, the work presented in this thesis needs to be repeated for reactor like scenarios, and in concert with studies which focus on disentangling the impact of a tight baffle from that of dB/dz on detachment location sensitivity.

In general, the SOLPS prediction of the slowing down of the detachment movement before it reaches the X-point is an important result in itself since this has not been observed in other tokamaks. If this reduction in sensitivity is indeed observed in MAST-U experiments, and if it is shown to be primarily due to the high parallel gradients in B, this could potentially provide a way of passively stabilising the detachment front at an optimum location in the divertor. The research presented in this thesis may help guide improvements in the DLS model which could then serve as a useful tool for the future divertor design and optimisation.

Analysis performed to interpret the second main result, the significant differences in the volume recombination levels in strongly detached conditions and the connection with ion-molecule elastic collisions, was the subject of chapter 6. An energy, momentum and particle balance analysis was performed for a strongly detached case chosen from each of the three scans to better understand the role of $D^+ - D_2$ elastic collisions. These cases were chosen such that the detachment location is similar amongst the three cases.

In the fuelling case, the higher divertor plasma and neutral densities achieved in this scan mean more plasma-neutral interactions and therefore enhanced energy and momentum loss to $D^+ - D_2$ elastic collisions. In particular, as the temperatures approach 1eV, $D^+ - D_2$ elastic collisions play the key role in removing heat from the plasma to access sub-eV temperatures. Further, a relatively large plasma flux flows into the detached region and towards the target while interacting with a relatively dense cloud of deuterium atoms and molecules in the fuelling case. This cloud 'plugs' the plasma flow across the detached region, primarily through $D^+ - D_2$ elastic collisions. Since the net particle sink across most of the detached region is rather small, a steady increase in plasma density across this region is observed. The sharp increase in molecular density close to the target indicates that the elastic collisions also appear to keep most of the molecules 'squashed' to the target. Coupled with the already high plasma density, this sharp increase in molecule density close to the target drives strong power losses to $D^+ - D_2$ elastic collisions, leading to sub-eV temperatures and increased volume recombination across this region.

In the nitrogen seeded case, the neutral density is significantly lower across the detached region, and the plasma flux entering the detached region is half that in the fuelling case. In addition, almost half the plasma across the detached region is composed of singly ionised nitrogen which carries a large fraction of the plasma momentum because of its mass, and it also does not interact with the neutrals in these simulations. Deuterium ions regain most of the momentum lost to interactions with neutrals through friction with nitrogen ions. The plasma flow is not 'plugged' as effectively

as in the fuelling case and plasma flow velocity across the divertor does not change significantly. Again, the net particle source is small across most of the detached region so the relatively small changes in the flow velocity across the detached region result in a flat density profile in seeded the case. The lower neutral and plasma densities correspond to fewer plasma-neutral interactions and therefore lower heat dissipation, which is one of the likely reasons why the temperature in this case does not drop significantly below 1eV. Further, the actual impact of $D^+ - D_2$ elastic collisions on the internal energy is likely weakened by the presence of a large amount nitrogen in two ways. First, it is the directed kinetic energy (which does not directly affect the temperature) that appears to be preferentially dissipated by $D^+ - D_2$ elastic collisions (as opposed to the internal energy which is directly correlated with the temperature). The directed kinetic energy is significantly higher in the seeded case due to the large amount of nitrogen, weakening the impact of the elastic collisions on the internal energy. Second, the only way nitrogen ions can lose heat is through friction with the main ions. Since all ion species have the same temperature in the SOLPS model, the nitrogen effectively acts like a reservoir of heat and again results in $D^+ - D_2$ elastic collisions having a rather weak impact on the plasma internal energy. Thus, the plasma temperature across the detached region does not drop significantly below 1eV. The combined result of a relatively low plasma density and a high plasma temperature is negligible recombination.

Broadly, this analysis shows that in strongly detached conditions in the simulated parameter space, elastic collisions between ions and neutrals will introduce a significant drag on the plasma exiting the thermal front and flowing towards the target - this results in a plasma density profile that is strongly peaked near the target. Further, it suggests that volumetric power loss through the electron channel and momentum loss associated with atomic and molecular charge exchange may weaken significantly as the temperature in the divertor falls below 1eV, leaving ion channel power losses resulting from elastic collisions to dominate at these temperatures. Although only $D^+ - D_2$ elastic collisions were studied in this work, this analysis suggests other types of elastic collisions which were not included in this study (which are present in experiments) are likely to affect the plasma solution in a similar way. This indicates that because elastic collisions between the main ions and the impurity neutrals, and between impurity ions and all neutrals, are not included in the nitrogen seeded simulations, the target density and temperature in strongly detached conditions is likely underestimated and overestimated respectively - leading to an underestimation of the resulting recombination levels. It suggests that including elastic collisions between nitrogen ions and molecules may lead to certain features of strongly detached solutions from the fuelling case being recovered in the seeded case. In other words, it possible that such qualitative differences in strongly detached conditions achieved from either method may not actually be observed in experiment because in reality, both main and impurity ions will interact with both corresponding

neutrals. Further, in the case of nitrogen, nitrogen molecules and ammonia would exist which could be important sources of energy and momentum loss and could indeed plug the plasma flow through elastic collisions as effectively as deuterium molecules do in the non-seeded case.

Lastly, it highlights a potentially important aspect of the momentum balance across the detached region of the Super-X divertor - the increase in connection length between the X-point and divertor enables the thermal front to move quite far from the target. The impurity concentration across this rather large detached region can be significantly higher than that in the radiating thermal front region. Since radiating impurities are significantly heavier than dueterium, in strongly detached conditions (i.e. when the thermal front is far from the target), a relatively small impurity fraction could carry a significant fraction of the plasma momentum across the detached region. This indicates that fixed impurity fraction models may not be suitable to model strongly detached long-legged divertors like the Super-X case considered in this work. While fixed impurity fraction models may reasonably capture the radiative power loss, in situations where the detached region is comparable to the divertor size, it is important to model the transport of impurities across this region to capture their contribution to the momentum balance. In addition, analysis of the sound speeds of the various species near the target in the seeded case shows that in scenarios where the impurity fraction across the detached is region is significant, the target boundary condition used in this work may not be appropriate - more work is needed to identify the right boundary condition. In reactor relevant conditions, heavy noble gases will likely be used for power dissipation. Therefore, key energy and momentum exchange channels for these impurity ions and neutrals need to be identified and included in the SOLPS-ITER code package in order to accurately model strongly detached Super-X divertor conditions involving large impurity fractions.

References

[1] G.H. Miley, H. Towner, and N. Ivich. *Fusion cross sections and reactivities*. Tech. rep. U.S. Department of Energy: Technical Information Center, 1974. DOI: 10.2172/4014032. URL: http://www.osti.gov/servlets/purl/4014032/.

[2] S Pfalzner. *An Introduction to Inertial Confinement Fusion, Series in Plasma Physics*. Taylor Francis, 2006.

[3] J Wesson. *Tokamaks*. Oxford University Press, 2011.

[4] J. D. Lawson. *Some Criteria for a Useful Thermonuclear Reactor*. Tech. rep. U.S. Department of Energy: Technical Information Center, 1955. URL: http://www.osti.gov/servlets/purl/4014032/.

[5] J. D. Lawson. "Some criteria for a power producing thermonuclear reactor". In: *Proceedings of the Physical Society. Section B* 70.1 (1957), pp. 6–10. ISSN: 03701301. DOI: 10.1088/0370-1301/70/1/303. URL: https://iopscience.iop.org/article/10.1088/0370-1301/70/1/303https://iopscience.iop.org/article/10.1088/0370-1301/70/1/303/meta.

[6] C Gormezano et al. "Internal Transport Barriers in JET Deuterium-Tritium Plasmas". In: (1998).

[7] Martin Greenwald. "Density limits in toroidal plasmas". In: *Plasma Physics and Controlled Fusion* 44.8 (2002), p. 201. ISSN: 07413335. DOI: 10.1088/0741-3335/44/8/201. URL: http://stacks.iop.org/0741-3335/44/i=8/a=201?key=crossref.10b223c9bfedf85db5ed007f2fdae8a5.

[8] Christophe Szwaj et al. "Achievement of record β in the START spherical tokamak". In: *Physical Review Letters* 80.18 (1998), pp. 3972–3975. ISSN: 10797114. DOI: 10.1103/PhysRevLett.80.3972. URL: https://journals.aps.org/prl/abstract/10.1103/PhysRevLett.80.3972.

[9] A. Sykes. "Spherical tokamak programme at Culham". In: *Nuclear Fusion* 39.Special Issue (1999), pp. 1271–1281. ISSN: 00295515. DOI: 10.1088/0029-5515/39/9y/305. URL: https://iopscience.iop.org/article/10.1088/0029-5515/39/9Y/305https://iopscience.iop.org/article/10.1088/0029-5515/39/9Y/305/meta.

[10] Alan Sykes. *Overview of recent spherical tokamak results*. 2001. DOI: 10.1088/0741-3335/43/12A/309. URL: https://iopscience.iop.org/article/10.1088/0741-3335/43/12A/309https://iopscience.iop.org/article/10.1088/0741-3335/43/12A/309/meta.

[11] B. Lloyd et al. "MAST and the impact of low aspect ratio on tokamak physics". In: *Plasma Physics and Controlled Fusion*. Vol. 46. 12 B. IOP Publishing, 2004, pp. 477–494. DOI: 10.1088/0741-3335/46/12B/040. URL: https://iopscience.iop.org/article/10.1088/0741-3335/46/12B/040https://iopscience.iop.org/article/10.1088/0741-3335/46/12B/040/meta.

[12] S. M. Kaye et al. "Energy confinement scaling in the low aspect ratio National Spherical Torus Experiment (NSTX)". In: *Nuclear Fusion*. Vol. 46. 10. IOP Publishing, 2006, pp. 848–857. DOI: 10.1088/0029-5515/46/10/002. URL: https://iopscience.iop.org/article/10.1088/0029-5515/46/10/002https://iopscience.iop.org/article/10.1088/0029-5515/46/10/002/meta.

[13] G. S. Kurskiev et al. "Scaling of energy confinement time in the Globus-M spherical tokamak". In: *Plasma Physics and Controlled Fusion* 59.4 (2017), p. 045010. ISSN: 13616587. DOI: 10.1088/1361-6587/aa5cd5. URL: https://doi.org/10.1088/1361-6587/aa5cd5.

[14] Y. Takase et al. *Overview of spherical tokamak research in Japan*. 2017. DOI: 10.1088/1741-4326/aa62c1. URL: https://doi.org/10.1088/1741-4326/aa62c1.

[15] Y. K.M. Peng et al. "A component test facility based on the spherical tokamak". In: *Plasma Physics and Controlled Fusion*. Vol. 47. 12 B. IOP Publishing, 2005, pp. 263–283. DOI: 10.1088/0741-3335/47/12B/S20. URL: https://iopscience.iop.org/article/10.1088/0741-3335/47/12B/S20https://iopscience.iop.org/article/10.1088/0741-3335/47/12B/S20/meta.

[16] H. R. Wilson et al. "Integrated plasma physics modelling for the Culham steady state spherical tokamak fusion power plant". In: *Nuclear Fusion* 44.8 (2004), pp. 917–929. ISSN: 00295515. DOI: 10.1088/0029-5515/44/8/010. URL: https://iopscience.iop.org/article/10.1088/0029-5515/44/8/010https://iopscience.iop.org/article/10.1088/0029-5515/44/8/010/meta.

[17] A. Sykes et al. “Compact fusion energy based on the spherical tokamak”. In: *Nuclear Fusion* 58.1 (2018), p. 016039. ISSN: 17414326. DOI: 10.1088/1741-4326/aa8c8d. URL: https://doi.org/10.1088/1741-4326/aa8c8d.

[18] A. E. Costley. “Towards a compact spherical tokamak fusion pilot plant”. In: *Philosophical Transactions of the Royal Society A: Mathematical, Physical and Engineering Sciences*. Vol. 377. 2141. Royal Society Publishing, 2019. DOI: 10.1098/rsta.2017.0439. URL: https://royalsocietypublishing.org/doi/abs/10.1098/rsta.2017.0439.

[19] *EURO-FUSION*. https://www.euro-fusion.org/.

[20] Paulett C. Li Ewer. “Measurements of microturbulence in tokamaks and comparisons with theories of turbulence and anomalous transport”. In: *Nuclear Fusion* 25.5 (1985), pp. 543–621. ISSN: 17414326. DOI: 10.1088/0029-5515/25/5/004. URL: https://iopscience.iop.org/article/10.1088/0029-5515/25/5/004https://iopscience.iop.org/article/10.1088/0029-5515/25/5/004/meta.

[21] D. Gresillon and M. A. (Marc A.) Dubois. *Turbulence and anomalous transport in magnetized plasmas : proceedings of the International Workshop on Small Scale Turbulence and Anomalous Transport in Magnetized Plasmas held July 6-12th, 1986 at Institut detudes scientifiques de Cargese, Corse du S.* [L’Ecole Polytechnique], 1987, p. 335. ISBN: 2730201483. URL: https://inis.iaea.org/search/search.aspx?orig_q=RN:21033229https://inis.iaea.org/search/search.aspx?orig_q=RN:21033314.

[22] A. J. Wootton et al. “Fluctuations and anomalous transport in tokamaks”. In: *Physics of Fluids B* 2.12 (1990), pp. 2879–2903. ISSN: 08998221. DOI: 10.1063/1.859358. URL: http://aip.scitation.org/doi/10.1063/1.859358.

[23] F. Wagner et al. “Regime of improved confinement and high beta in neutral-beam-heated divertor discharges of the ASDEX tokamak”. In: *Physical Review Letters* 49.19 (1982), pp. 1408–1412. ISSN: 00319007. DOI: 10.1103/PhysRevLett.49.1408. URL: https://journals.aps.org/prl/abstract/10.1103/PhysRevLett.49.1408.

[24] F. Wagner et al. “Development of an Edge Transport Barrier at the H-Mode Transition of ASDEX”. In: *Physical Review Letters* 53.15 (1984), pp. 1453–1456. ISSN: 00319007. DOI: 10.1103/PhysRevLett.53.1453. URL: https://journals.aps.org/prl/abstract/10.1103/PhysRevLett.53.1453.

[25] R. J. Groebner. “An emerging understanding of H-mode discharges in tokamaks”. In: *Physics of Fluids B* 5.7 (1993), pp. 2343–2354. ISSN: 08998221. DOI: 10.1063/1.860770. URL: http://aip.scitation.org/doi/10.1063/1.860770.

[26] R. A. Pitts et al. *Physics basis for the first ITER tungsten divertor*. 2019. DOI: 10.1016/j.nme.2019.100696.

[27] T. Hirai et al. "Status of technology RD for the ITER tungsten divertor monoblock". In: *Journal of Nuclear Materials* 463 (2015), pp. 1248–1251. ISSN: 00223115. DOI: 10.1016/j.jnucmat.2014.12.027.

[28] T. Eich et al. "Inter-ELM power decay length for JET and ASDEX Upgrade: Measurement and comparison with heuristic drift-based model". In: *Physical Review Letters* 107.21 (2011), p. 215001. ISSN: 00319007. DOI: 10.1103/PhysRevLett.107.215001. URL: https://journals.aps.org/prl/abstract/10.1103/PhysRevLett.107.215001.

[29] T. Eich et al. "Scaling of the tokamak near the scrape-off layer H-mode power width and implications for ITER". In: *Nuclear Fusion* 53.9 (2013), p. 093031. ISSN: 00295515. DOI: 10.1088/0029-5515/53/9/093031. URL: https://iopscience.iop.org/article/10.1088/0029-5515/53/9/093031https://iopscience.iop.org/article/10.1088/0029-5515/53/9/093031/meta.

[30] R. J. Goldston. "Heuristic drift-based model of the power scrape-off width in low-gas-puff H-mode tokamaks". In: *Nuclear Fusion* 52.1 (2012), p. 013009. ISSN: 00295515. DOI: 10.1088/0029-5515/52/1/013009. URL: https://iopscience.iop.org/article/10.1088/0029-5515/52/1/013009https://iopscience.iop.org/article/10.1088/0029-5515/52/1/013009/meta.

[31] M. Wischmeier. "High density operation for reactor-relevant power exhaust". In: *Journal of Nuclear Materials* 463 (2015), pp. 22–29. ISSN: 00223115. DOI: 10.1016/j.jnucmat.2014.12.078.

[32] R. A. Pitts et al. "Physics conclusions in support of ITER W divertor monoblock shaping". In: *Nuclear Materials and Energy* 12 (2017), pp. 60–74. ISSN: 23521791. DOI: 10.1016/j.nme.2017.03.005.

[33] G. Federici et al. "European DEMO design strategy and consequences for materials". In: *Nuclear Fusion* 57.9 (2017), p. 092002. ISSN: 17414326. DOI: 10.1088/1741-4326/57/9/092002. URL: https://doi.org/10.1088/1741-4326/57/9/092002.

[34] H. Reimerdes et al. "Assessment of alternative divertor configurations as an exhaust solution for DEMO". In: *Nuclear Fusion* 60.6 (2020), p. 066030. ISSN: 17414326. DOI: 10.1088/1741-4326/ab8a6a. URL: https://doi.org/10.1088/1741-4326/ab8a6a.

[35] G. F. Matthews. "Plasma detachment from divertor targets and limiters". In: *Journal of Nuclear Materials* 220-222 (1995), pp. 104–116. ISSN: 00223115. DOI: 10.1016/0022-3115(94)00450-1.

[36] C. S. Pitcher and P. C. Stangeby. *Experimental divertor physics*. 1997. DOI: 10.1088/0741-3335/39/6/001. URL: https://iopscience.iop.org/article/10.1088/0741-3335/39/6/001https://iopscience.iop.org/article/10.1088/0741-3335/39/6/001/meta.

[37] A Loarte et al. "Chapter 4: Power and particle control". In: *Nuclear Fusion* 47.6 (2007), S203. URL: http://stacks.iop.org/0029-5515/47/i=6/a=S04.

[38] A Kallenbach et al. "Impurity seeding for tokamak power exhaust : from present devices via ITER to DEMO". In: *Plasma Phys. Control. Fusion* 55 (2013), p. 124041. DOI: 10.1088/0741-3335/55/12/124041.

[39] S. I. Krasheninnikov and A. S. Kukushkin. "Physics of ultimate detachment of a tokamak divertor plasma". In: *Journal of Plasma Physics* 83.5 (2017), p. 155830501. ISSN: 14697807. DOI: 10.1017/S0022377817000654. URL: https://www.cambridge.org/core/product/identifier/S0022377817000654/type/journal_article.

[40] V A Soukhanovskii. "A review of radiative detachment studies in tokamak advanced magnetic divertor con fi gurations". In: *Plasma Physics and Controlled Fusion* 59.6 (2017), p. 64005. ISSN: 13616587. DOI: 10.1088/1361-6587/aa6959. URL: http://dx.doi.org/10.1088/1361-6587/aa6959.

[41] A. Loarte and R. Neu. "Power exhaust in tokamaks and scenario integration issues". In: *Fusion Engineering and Design* 122 (2017), pp. 256–273. ISSN: 09203796. DOI: 10.1016/j.fusengdes.2017.06.024.

[42] A. W. Leonard. "Plasma detachment in divertor tokamaks". In: *Plasma Physics and Controlled Fusion* 60.4 (2018), p. 44001. ISSN: 13616587. DOI: 10.1088/1361-6587/aaa7a9. URL: https://doi.org/10.1088/1361-6587/aaa7a9.

[43] P. C. Stangeby. "Basic physical processes and reduced models for plasma detachment". In: *Plasma Physics and Controlled Fusion* 60.4 (2018), p. 044022. ISSN: 13616587. DOI: 10.1088/1361-6587/aaacf6. URL: https://doi.org/10.1088/1361-6587/aaacf6.

[44] B Lipschultz et al. "Divertor physics research on alcator C-Mod". In: *Fusion Science and Technology* 51.3 (2007), pp. 369–389. ISSN: 15361055. DOI: 10.13182/FST07-A1428. URL: https://www.tandfonline.com/action/journalInformation?journalCode=ufst20.

[45] Peter Stangeby. "The roles of power loss and momentum-pressure loss in causing particle-detachment in tokamak divertors: I. A heuristic model analysis". In: *Plasma Physics and Controlled Fusion* 62.2 (2020), p. 025012. ISSN: 13616587. DOI: 10.1088/1361-6587/ab51a9. URL: https://doi.org/10.1088/1361-6587/ab51a9.

[46] R Schneider et al. "Plasma Edge Physics with B2-Eirene". In: *Contributions to Plasma Physics* 46.1-2 (2006), pp. 3–191. URL: http://dx.doi.org/10.1002/ctpp.200610001.

[47] B Lipschultz et al. "The role of particle sinks and sources in Alcator C-Mod detached divertor discharges". In: *Physics of Plasmas* 6 (1999), p. 1907. DOI: 10.1063/1.873448. URL: https://doi.org/10.1063/1.873448.

[48] K. Verhaegh et al. "An improved understanding of the roles of atomic processes and power balance in divertor target ion current loss during detachment". In: *Nuclear Fusion* 59.12 (2019), p. 126038. ISSN: 17414326. DOI: 10.1088/1741-4326/ab4251. arXiv: 1810.04969. URL: https://iopscience.iop.org/article/10.1088/1741-4326/ab4251.

[49] A Smolders et al. "Comparison of high density and nitrogen seeded detachment using SOLPS-ITER simulations of the tokamak á configuration variable". In: *Plasma Physics and Controlled Fusion* 62.12 (2020), p. 125006. ISSN: 0741-3335. DOI: 10.1088/1361-6587/abbcc5. URL: https://doi.org/10.1088/1361-6587/abbcc5.

[50] P. C. Stangeby. *The Plasma Boundary of Magnetic Fusion Devices*. IOP Publishing, 2000. ISBN: 0750305592. DOI: 10.1088/0741-3335/43/2/702. URL: http://stacks.iop.org/0741-3335/43/i=2/a=702?key=crossref.697b1e31667aa5230930cad92b5e0e4f.

[51] J. Roth. "Review and status of physical sputtering and chemical erosion of plasma facing materials". In: *Springer Series in Chemical Physics* 78 (2005), pp. 203–224. ISSN: 01726218. DOI: 10.1007/3-540-27362-x_9. URL: https://link.springer.com/chapter/10.1007/3-540-27362-X_9.

[52] J A Goetz et al. "High confinement dissipative divertor operation on Alcator C-Mod". In: *Physics of Plasmas* 6 (1999), p. 1899. DOI: 10.1063/1.873447. URL: https://doi.org/10.1063/1.873447.

[53] A R Field et al. "Dynamics and stability of divertor detachment in H-mode plasmas on JET". In: *Plasma Phys. Control. Fusion* 59.9 (2017), p. 37.

[54] M. Bernert et al. "The H-mode density limit in the full tungsten ASDEX Upgrade tokamak". In: *Plasma Physics and Controlled Fusion* 57.1 (2015), p. 014038. ISSN: 13616587. DOI: 10.1088/0741-3335/57/1/014038. URL: https://iopscience.iop.org/article/10.

1088/0741-3335/57/1/014038https://iopscience.iop.org/article/10.1088/0741-3335/57/1/014038/meta.

[55] M. G. Dunne et al. "The role of the density profile in the ASDEX-Upgrade pedestal structure". In: *Plasma Physics and Controlled Fusion* 59.1 (2017), p. 014017. ISSN: 13616587. DOI: 10.1088/0741-3335/59/1/014017. URL: http://euro-fusionscipub.org/mst1.

[56] J A Goetz et al. "Impurity compression and enrichment studies on Alcator C-Mod". In: *Journal of Nuclear Materials* 266 (1999), pp. 354–359. ISSN: 00223115. DOI: 10.1016/S0022-3115(98)00582-0.

[57] K. Shimizu, T. Takizuka, and A. Sakasai. "A review on impurity transport in divertors". In: *Journal of Nuclear Materials* 241-243 (1997), pp. 167–181. ISSN: 00223115. DOI: 10.1016/s0022-3115(97)80038-4.

[58] I. Yu Senichenkov et al. "On mechanisms of impurity leakage and retention in the tokamak divertor". In: *Plasma Physics and Controlled Fusion* 61.4 (2019), p. 24. ISSN: 13616587. DOI: 10.1088/1361-6587/ab04d0. URL: https://doi.org/10.1088/1361-6587/ab04d0.

[59] P. C. Stangeby and D. Moulton. "A simple analytic model of impurity leakage from the divertor and accumulation in the main scrape-off layer". In: *Nuclear Fusion* 60.10 (2020), p. 106005. ISSN: 17414326. DOI: 10.1088/1741-4326/ab9e16. URL: https://doi.org/10.1088/1741-4326/ab9e16.

[60] J Neuhauser et al. "The compatibility of high confinement times and complete divertor detachment in ASDEX-Upgrade". In: *Plasma Physics and Controlled Fusion* 37.11A (1995), A37–A51. ISSN: 0741-3335. DOI: 10.1088/0741-3335/37/11A/003. URL: http://stacks.iop.org/0741-3335/37/i=11A/a=003?key=crossref.7ee635253de5909670d879b96cf0e07f.

[61] N. Asakura et al. "Investigations of impurity seeding and radiation control for long-pulse and high-density H-mode plasmas in JT-60U". In: *Nuclear Fusion* 49.11 (2009), p. 115010. ISSN: 00295515. DOI: 10.1088/0029-5515/49/11/115010. URL: https://iopscience.iop.org/article/10.1088/0029-5515/49/11/115010https://iopscience.iop.org/article/10.1088/0029-5515/49/11/115010/meta.

[62] G. P. Maddison et al. "Moderation of divertor heat loads by fuelling and impurity seeding in well-confined ELMy H-mode plasmas on JET". In: *Nuclear Fusion* 51.4 (2011), p. 042001. ISSN: 00295515. DOI: 10.1088/0029-5515/51/4/042001. URL: http://www-pub.iaea.org/MTCD/.

[63] M. L. Reinke et al. “Effect of N2, Ne and Ar seeding on Alcator C-Mod H-mode confinement”. In: *Journal of Nuclear Materials*. Vol. 415. 1 SUPPL. Elsevier B.V., 2011, S340–S344. DOI: 10.1016/j.jnucmat.2010.10.055.

[64] A. Kallenbach et al. “Partial detachment of high power discharges in ASDEX Upgrade”. In: *Nuclear Fusion* 55.5 (2015), p. 053026. ISSN: 17414326. DOI: 10.1088/0029-5515/55/5/053026. URL: https://iopscience.iop.org/article/10.1088/0029-5515/55/5/053026https://iopscience.iop.org/article/10.1088/0029-5515/55/5/053026/meta.

[65] F. Reimold et al. “Experimental studies and modeling of complete H-mode divertor detachment in ASDEX Upgrade”. In: *Journal of Nuclear Materials* 463 (2015), pp. 128–134. ISSN: 00223115. DOI: 10.1016/j.jnucmat.2014.12.019.

[66] H. Q. Wang et al. “Effects of low-Z and high-Z impurities on divertor detachment and plasma confinement”. In: *Nuclear Materials and Energy* 0 (2017), pp. 1–6. ISSN: 23521791. DOI: 10.1016/j.nme.2017.01.027.

[67] A. Huber et al. “Peculiarity of highly radiating multi-impurity seeded H-mode plasmas on JET with ITER-like wall”. In: *Physica Scripta*. Vol. 2020. T171. Institute of Physics Publishing, 2020, p. 014055. DOI: 10.1088/1402-4896/ab5753. URL: https://doi.org/10.1088/1402-4896/ab5753.

[68] M. Bernert et al. “X-point radiation, its control and an ELM suppressed radiating regime at the ASDEX Upgrade tokamak”. In: *Nuclear Fusion* 61.2 (2021), p. 024001. ISSN: 17414326. DOI: 10.1088/1741-4326/abc936. URL: https://doi.org/10.1088/1741-4326/ab2211https://doi.org/10.1088/1741-4326/ab18b8.

[69] D. Eldon et al. “An analysis of controlled detachment by seeding various impurity species in high performance scenarios on DIII-D and EAST”. In: *Nuclear Materials and Energy* 27 (2021), p. 100963. ISSN: 23521791. DOI: 10.1016/j.nme.2021.100963.

[70] M. Siccinio et al. “Impact of an integrated core/SOL description on the R and B T optimization of tokamak fusion reactors”. In: *Nuclear Fusion* 58.1 (2018), p. 016032. ISSN: 17414326. DOI: 10.1088/1741-4326/aa9583. URL: https://doi.org/10.1088/1741-4326/aa9583.

[71] P. M. Valanju et al. “Super-X divertors and high power density fusion devices”. In: *Physics of Plasmas* 16.5 (2009), p. 056110. ISSN: 1070-664X. DOI: 10.1063/1.3110984. URL: http://aip.scitation.org/doi/10.1063/1.3110984.

[72] M Kotschenreuther et al. “The super X divertor (SXD) and a compact fusion neutron source (CFNS)”. In: *Nuclear Fusion* 50.3 (2010), p. 35003. URL: http://stacks.iop.org/0029-5515/50/i=3/a=035003.

[73] T. W. Petrie et al. “Effect of separatrix magnetic geometry on divertor behavior in DIII-D”. In: *Journal of Nuclear Materials* 438.SUPPL (2013). ISSN: 00223115. DOI: 10.1016/j.jnucmat.2013.01.051.

[74] E Havlíčková et al. “The effect of the Super-X divertor of MAST Upgrade on impurity radiation as modelled by SOLPS”. In: *Journal of Nuclear Materials* 463 (2015), pp. 1209–1213. DOI: 10.1016/j.jnucmat.2014.10.073.

[75] E Havlíčková et al. “SOLPS analysis of the MAST-U divertor with the effect of heating power and pumping on the access to detachment in the Super-x configuration”. In: *Plasma Physics and Controlled Fusion* 57.11 (2015), p. 115001. ISSN: 0741-3335. DOI: 10.1088/0741-3335/57/11/115001. URL: http://stacks.iop.org/0741-3335/57/i=11/a=115001?key=crossref.1189ca7b2936d4104038cb5efefc0dfb.

[76] Bruce Lipschultz, Felix I. Parra, and Ian H. Hutchinson. “Sensitivity of detachment extent to magnetic configuration and external parameters”. In: *Nuclear Fusion* 56.5 (2016), p. 056007. ISSN: 0029-5515. DOI: 10.1088/0029-5515/56/5/056007. URL: http://stacks.iop.org/0029-5515/56/i=5/a=056007?key=crossref.a45c46af3713ecdd5358a4851aa5f61d.

[77] D Moulton et al. “Using SOLPS to con fi rm the importance of total fl ux expansion in Super-X divertors”. In: *Plasma Phys. Control. Fusion* 59 (2017). ISSN: 0741-3335. DOI: 10.1088/1361-6587/aa6b13. URL: http://iopscience.iop.org/0741-3335/59/6/065011.

[78] D Moulton, B Lipschultz, and J Harrison. “Detachment onset in MAST-U according to SOLPS-ITER”. In: *44th EPS Conference on Plasma Physics, EPS 2017*. June. 2017, pp. 1–45. ISBN: 9781510849303.

[79] C. Theiler et al. “Results from recent detachment experiments in alternative divertor configurations on TCV”. In: *Nuclear Fusion* 57.7 (2017), p. 072008. ISSN: 0029-5515. DOI: 10.1088/1741-4326/aa5fb7. URL: http://stacks.iop.org/0029-5515/57/i=7/a=072008?key=crossref.e0ba8c2b73c98effa804e1a3ad432e8c.

[80] A Fil et al. “Separating the roles of magnetic topology and neutral trapping in modifying the detachment threshold for TCV”. In: *Plasma Physics and Controlled Fusion* 62.3 (2020). ISSN: 13616587. DOI: 10.1088/1361-6587/ab69bb. URL: https://doi.org/10.1088/1361-6587/ab69bb.

[81] D. Stork et al. "The upgrade to the Mega Amp Spherical Tokamak". In: *International Atomic Energy Agency (IAEA) Fusion Energy Conference*. 2010. URL: https://inis.iaea.org/search/search.aspx?orig_q=RN:43043465.

[82] A. W. Morris. "MAST: Results and upgrade activities". In: *IEEE Transactions on Plasma Science*. Vol. 40. 3 PART 1. 2012, pp. 682–691. DOI: 10.1109/TPS.2011.2181540.

[83] William Morris et al. "MAST Upgrade Divertor Facility: A Test Bed for Novel Divertor Solutions". In: *IEEE Transactions on Plasma Science* 46.5 (2018), pp. 1217–1226. ISSN: 00933813. DOI: 10.1109/TPS.2018.2815283.

[84] S. Wiesen et al. "The new SOLPS-ITER code package". In: *Journal of Nuclear Materials* 463 (2015), pp. 480–484. ISSN: 0022-3115. DOI: 10.1016/J.JNUCMAT.2014.10.012.

[85] Xavier Bonnin et al. "Presentation of the New SOLPS-ITER Code Package for Tokamak Plasma Edge Modelling *)". In: *Plasma and Fusion Research* 11 (2016). DOI: 10.1585/pfr.11.1403102. URL: https://portal.iter.org/departments/POP/CM/IMAS/SOLPS-ITER/SOLPS-ITERPapers/PFR2016_11-1403102.pdf.

[86] E.W. Thomas. "Particle induced electron emission". In: *Suppl. Nucl. Fusion* 1 (1991), pp. 79–91. URL: https://inis.iaea.org/search/search.aspx?orig_q=RN:23010276.

[87] Wolfhard Möller. "Hydrogen trapping and transport in carbon". In: *Journal of Nuclear Materials* 162-164.C (1989), pp. 138–150. ISSN: 00223115. DOI: 10.1016/0022-3115(89)90264-X.

[88] K.L. Wilson et al. "Trapping, Detrapping and Release of Implanted Hydrogen Isotopes. Atomic and Plasma-Material Interaction Data for Fusion". In: *Nuclear Fusion, Special Supplement 1* (1991), pp. 31–38.

[89] D Bohm. *The characteristics of electrical discharges in magnetic fields*. Ed. by A Guthrie and R K Wakerling. New York: McGraw-Hill, 1949, Ch 3. URL: https://www.worldcat.org/title/characteristics-of-electrical-discharges-in-magnetic-fields/oclc/552825.

[90] Roland Chodura. "Plasma Flow in the Sheath and the Presheath of a Scrape-Off Layer". In: *Physics of Plasma-Wall Interactions in Controlled Fusion*. Springer US, 1986, pp. 99–134. DOI: 10.1007/978-1-4757-0067-1_4. URL: https://link.springer.com/chapter/10.1007/978-1-4757-0067-1_4.

[91] J. Roth. "Physical Sputtering of Solids at Ion Bombardment". In: *Physics of Plasma-Wall Interactions in Controlled Fusion*. Springer US, 1986, pp. 351–388. DOI: 10.1007/978-1-

4757-0067-1_8. URL: https://link.springer.com/chapter/10.1007/978-1-4757-0067-1_8.

[92] J. Bohdansky, J. Roth, and H. L. Bay. "An analytical formula and important parameters for low-energy ion sputtering". In: *Journal of Applied Physics* 51.5 (1980), pp. 2861–2865. ISSN: 00218979. DOI: 10.1063/1.327954. URL: http://scitation.aip.org/content/aip/journal/jap/51/5/10.1063/1.327954.

[93] J. Roth, E. Vietzke, and A.A. Haasz. "Erosion of graphite due to particle impact". In: *Suppl. Nucl. Fusion* 1 (1991), pp. 63–78. URL: https://inis.iaea.org/search/search.aspx?orig_q=RN:23010275.

[94] J Roth and C Garcia-Rosales. "Analytic description of the chemical erosion of graphite by hydrogen ions". In: *Nuclear Fusion* 36.12 (1996), p. 1647. URL: http://stacks.iop.org/0029-5515/36/i=12/a=I05.

[95] S. I. Krasheninnikov, A. S. Kukushkin, and A. A. Pshenov. "Divertor plasma detachment". In: *Physics of Plasmas* 23.5 (2016). ISSN: 10897674. DOI: 10.1063/1.4948273.

[96] C. S. Pitcher and P. C. Stangeby. *Experimental divertor physics*. 1997. DOI: 10.1088/0741-3335/39/6/001. URL: https://iopscience.iop.org/article/10.1088/0741-3335/39/6/001https://iopscience.iop.org/article/10.1088/0741-3335/39/6/001/meta.

[97] S. I. Braginskii. "Transport Processes in a Plasma". In: *Reviews of Plasma Physics* 1 (1965), p. 205.

[98] Y Shimomura et al. "Characteristics of the divertor plasma in neutral-beam-heated ASDEX discharges". In: *Nuclear Fusion* 23.7 (1983), p. 869. URL: http://stacks.iop.org/0029-5515/23/i=7/a=002.

[99] B. LaBombard et al. "Scaling and transport analysis of divertor conditions on the Alcator C-Mod tokamak". In: *Physics of Plasmas* 2.6 (1995), pp. 2242–2248. ISSN: 1070-664X. DOI: 10.1063/1.871248. URL: http://aip.scitation.org/doi/10.1063/1.871248.

[100] S. I. Krasheninnikov et al. "Stability of divertor detachment". In: *Nuclear Materials and Energy* 0 (2016), pp. 1–6. ISSN: 23521791. DOI: 10.1016/j.nme.2017.01.022. URL: http://dx.doi.org/10.1016/j.nme.2017.01.022.

[101] M. V. Umansky et al. "Attainment of a stable, fully detached plasma state in innovative divertor configurations". In: *Physics of Plasmas* 24.5 (2017). ISSN: 10897674. DOI: 10.1063/1.4979193.

[102] M. R. Wade et al. “Impurity enrichment studies with induced scrape-off layer flow on DIII-D”. In: *Nuclear Fusion* 38.12 (1998), pp. 1839–1859. ISSN: 00295515. DOI: 10.1088/0029-5515/38/12/309. URL: https://iopscience.iop.org/article/10.1088/0029-5515/38/12/309https://iopscience.iop.org/article/10.1088/0029-5515/38/12/309/meta.

[103] Alberto Loarte. “Effects of divertor geometry on tokamak plasmas”. In: *Plasma Phys. Control. Fusion* 43.01 (2001). URL: http://efdasql.ipp.mpg.de/loarte/Divertor_Geometry_Review.pdf.

[104] A. A. Mavrin. “Radiative Cooling Rates for Low-Z Impurities in Non-coronal Equilibrium State”. In: *Journal of Fusion Energy* 36.4-5 (2017), pp. 161–172. ISSN: 01640313. DOI: 10.1007/s10894-017-0136-z. URL: https://link.springer.com/article/10.1007/s10894-017-0136-z.

[105] H. P. Summers et al. “Ionization state, excited populations and emission of impurities in dynamic finite density plasmas: I. The generalized collisional-radiative model for light elements”. In: *Plasma Physics and Controlled Fusion* 48.2 (2006), pp. 263–293. ISSN: 07413335. DOI: 10.1088/0741-3335/48/2/007. arXiv: 0511561 [astro-ph]. URL: https://iopscience.iop.org/article/10.1088/0741-3335/48/2/007https://iopscience.iop.org/article/10.1088/0741-3335/48/2/007/meta.

[106] *Atomic Data and Analysis Structure*. http://www.adas.ac.uk.

[107] X. J. Liu et al. “Modeling study of radiation characteristics with different impurity species seeding in EAST”. In: *Physics of Plasmas* 24.12 (2017), p. 122509. ISSN: 10897674. DOI: 10.1063/1.4997101. URL: http://aip.scitation.org/doi/10.1063/1.4997101.

[108] F Reimold. “Experimental Studies and Modeling of Divertor Plasma Detachment in H-Mode Discharges in the ASDEX Upgrade Tokamak ”. PhD thesis. 2015.

[109] J. A. Goetz et al. “Comparison of detached and radiative divertor operation in Alcator C-Mod”. In: *Physics of Plasmas* 3.5 (1996), pp. 1908–1915. ISSN: 10897674. DOI: 10.1063/1.871986. URL: http://aip.scitation.org/doi/10.1063/1.871986.

[110] J. R. Harrison et al. “Detachment evolution on the TCV tokamak”. In: *Nuclear Materials and Energy* 12 (2017), pp. 1071–1076. ISSN: 23521791. DOI: 10.1016/j.nme.2016.10.020.

[111] F. Reimold et al. “Divertor studies in nitrogen induced completely detached H-modes in full tungsten ASDEX Upgrade”. In: *Nuclear Fusion* 55.3 (2015), p. 033004. ISSN: 0029-5515. DOI: 10.1088/0029-5515/55/3/033004. URL: http://stacks.iop.org/0029-5515/55/i=3/a=033004?key=crossref.0962b244139c8cf6773a6a7fc176e9f5.

[112] H.-S. Bosch et al. “Helium transport and exhaust with an ITER-like divertor in ASDEX Upgrade”. In: *Journal of Nuclear Materials* 290-293 (2001), pp. 836–839. ISSN: 00223115. DOI: 10.1016/S0022-3115(00)00539-0. URL: http://linkinghub.elsevier.com/retrieve/pii/S0022311500005390.

[113] A Kallenbach et al. “Divertor power load feedback with nitrogen seeding in ASDEX Upgrade”. In: *Plasma Physics and Controlled Fusion* 52.5 (2010), p. 055002. ISSN: 0741-3335. DOI: 10.1088/0741-3335/52/5/055002. URL: http://stacks.iop.org/0741-3335/52/i=5/a=055002?key=crossref.cc7cc88ca20e822dd0724980a12286fb.

[114] A. Kallenbach et al. “Optimized tokamak power exhaust with double radiative feedback in ASDEX Upgrade”. In: *Nuclear Fusion* 52.12 (2012), p. 122003. ISSN: 0029-5515. DOI: 10.1088/0029-5515/52/12/122003. URL: http://stacks.iop.org/0029-5515/52/i=12/a=122003?key=crossref.b045ee086872468dbaa0a5312962ca08.

[115] B. Lipschultz et al. “Modification and control of divertor detachment in alcator C-Mod”. In: *Journal of Nuclear Materials* 241-243 (1997), pp. 771–776. ISSN: 00223115. DOI: 10.1016/s0022-3115(97)80138-9.

[116] C. S. Pitcher et al. “Routes to divertor detachment in ASDEX Upgrade”. In: *Journal of Nuclear Materials* 241-243 (1997), pp. 696–700. ISSN: 00223115. DOI: 10.1016/s0022-3115(97)80124-9.

[117] E Havlíčková et al. “Numerical studies of effects associated with the Super-X divertor on target parameters in MAST-U”. In: *Journal of Nuclear Materials* 438 (2013), pp. 545–549. DOI: 10.1016/j.jnucmat.2013.01.113.

[118] E Havlíčková, M Wischmeier, and G Fishpool. “Modelling the Effect of the Super-X Divertor in MAST Upgrade on Transition to Detachment and Distribution of Volumetric Power Losses”. In: *Contrib. Plasma Phys* 54 (2014), pp. 448–453. DOI: 10.1002/ctpp.201410025.

[119] E Havlíčková et al. “Investigation of conventional and Super-X divertor configurations of MAST Upgrade using scrape-off layer plasma simulation ˇ”. In: *Plasma Phys. Control. Fusion* 56 (2014), p. 075008. DOI: 10.1088/0741-3335/56/7/075008.

[120] M. V. Umansky et al. “Assessment of X-point target divertor configuration for power handling and detachment front control”. In: *Nuclear Materials and Energy* 0 (2016), pp. 1–6. ISSN: 23521791. DOI: 10.1016/j.nme.2017.03.015. URL: http://dx.doi.org/10.1016/j.nme.2017.03.015.

[121] B. J. Braams. “Radiative Divertor Modelling for ITER and TPX”. In: *Contributions to Plasma Physics* 36.2-3 (1996), pp. 276–281. ISSN: 08631042. DOI: 10.1002/ctpp.2150360233.

[122] V. Rozhansky et al. "New B2SOLPS5.2 transport code for H-mode regimes in tokamaks". In: *Nuclear Fusion* 49.2 (2009), pp. 25007–25018. ISSN: 00295515. DOI: 10.1088/0029-5515/49/2/025007. URL: https://iopscience.iop.org/article/10.1088/0029-5515/49/2/025007https://iopscience.iop.org/article/10.1088/0029-5515/49/2/025007/meta.

[123] D. Reiter, M. Baelmans, and P. Börner. "The eirene and B2-eirene codes". In: *Fusion Science and Technology* 47.2 (2005), pp. 172–186. ISSN: 15361055. DOI: 10.13182/FST47-172. URL: https://www.tandfonline.com/action/journalInformation?journalCode=ufst20.

[124] *EIRENE website*. http://www.eirene.de/.

[125] Radu. Balescu. *Transport processes in plasmas*. North-Holland, 1988, p. 803. ISBN: 044487092X. URL: https://inis.iaea.org/search/search.aspx?orig_q=RN:20043249.

[126] V M Zhdanov. "Transport Processes in Multicomponent Plasma". In: *Plasma Physics and Controlled Fusion* 44.10 (2002), pp. 2283–2283. ISSN: 0741-3335. DOI: 10.1088/0741-3335/44/10/701. URL: https://iopscience.iop.org/article/10.1088/0741-3335/44/10/701https://iopscience.iop.org/article/10.1088/0741-3335/44/10/701/meta.

[127] M Baelmans. "Code improvements and applications of a two-dimensional edge plasma model for toroidal fusion devices". PhD thesis. 1993.

[128] E. Sytova et al. "Impact of a new general form of friction and thermal forces on SOLPS-ITER modelling results". In: *Contributions to Plasma Physics* 58.6-8 (2018), pp. 622–628. ISSN: 08631042. DOI: 10.1002/ctpp.201700135. URL: http://doi.wiley.com/10.1002/ctpp.201700135.

[129] A. S. Kukushkin et al. "Role of molecular effects in divertor plasma recombination". In: *Nuclear Materials and Energy* 12 (2017), pp. 984–988. ISSN: 23521791. DOI: 10.1016/j.nme.2016.12.030.

[130] Kevin Verhaegh et al. "A study of the influence of plasma–molecule interactions on particle balance during detachment". In: *Nuclear Materials and Energy* 26 (2021), p. 100922. ISSN: 23521791. DOI: 10.1016/j.nme.2021.100922. arXiv: 2008.00272.

[131] V Kotov. "Numerical study of the ITER divertor plasma with the B2-EIRENE code package". PhD thesis. 2007.

[132] A Kirk et al. "A comparison of mid-plane scrape-off-layer measurements with model predictions in MAST and the calculation of cross-field transport coefficients". In: *Plasma Physics and Controlled Fusion* 46.10 (2004), pp. 1591–1603. ISSN: 07413335. DOI: 10.1088/0741-3335/46/10/005.

[133] J. R. Harrison, G M Fishpool, and A Kirk. "L-mode and inter-ELM divertor particle and heat flux width scaling on MAST". In: *Journal of Nuclear Materials* 438.SUPPL (2013). ISSN: 00223115. DOI: 10.1016/j.jnucmat.2013.01.074. URL: http://dx.doi.org/10.1016/j.jnucmat.2013.01.074.

[134] A J Thornton and A. Kirk. "Scaling of the scrape-off layer width during inter-ELM H modes on MAST as measured by infrared thermography". In: *Plasma Physics and Controlled Fusion* 56.5 (2014). ISSN: 13616587. DOI: 10.1088/0741-3335/56/5/055008.

[135] P. C. Stangeby. "Can detached divertor plasmas be explained as self-sustained gas targets?" In: *Nuclear Fusion* 33.11 (1993), pp. 1695–1705. ISSN: 00295515. DOI: 10.1088/0029-5515/33/11/I10. URL: https://iopscience.iop.org/article/10.1088/0029-5515/33/11/I10https://iopscience.iop.org/article/10.1088/0029-5515/33/11/I10/meta.

[136] T Ravensbergen et al. "Development of a real-time algorithm for detection of the divertor detachment radiation front using multi-spectral imaging". In: *Nuclear Fusion* 60.6 (2020). ISSN: 17414326. DOI: 10.1088/1741-4326/ab8183. URL: https://doi.org/10.1088/1741-4326/ab8183.

[137] A. W. Leonard et al. "Scaling radiative divertor solutions to high power in DIII-D". In: *Nuclear Fusion* 52.6 (2012), p. 063015. ISSN: 00295515. DOI: 10.1088/0029-5515/52/6/063015. URL: https://iopscience.iop.org/article/10.1088/0029-5515/52/6/063015https://iopscience.iop.org/article/10.1088/0029-5515/52/6/063015/meta.

[138] I.H Hutchinson. "Thermal front analysis of detached divertors and MARFEs". In: *Nuclear Fusion* 34 (1994), pp. 1337–1348. ISSN: 0029-5515. DOI: 10.1088/0029-5515/34/10/I04.

[139] L.L. Lengyel. *Analysis of radiating plasma boundary layers*. 1981. URL: https://inis.iaea.org/search/search.aspx?orig_q=RN:13657893.

[140] K. Lackner and R. Schneider. "The role of edge physics and confinement issues in the fusion reactor". In: *Fusion Engineering and Design* 22.1-2 (1993), pp. 107–116. ISSN: 09203796. DOI: 10.1016/S0920-3796(05)80012-2.

[141] D. Post et al. "Analytic criteria for power exhaust in divertors due to impurity radiation". In: *Journal of Nuclear Materials* 220-222 (1995), pp. 1014–1018. ISSN: 00223115. DOI: 10.1016/0022-3115(94)00464-1.

[142] M.L. Reinke. "Heat flux mitigation by impurity seeding in high-field tokamaks". In: *Nuclear Fusion* 57.3 (2017), p. 034004. ISSN: 0029-5515. DOI: 10.1088/1741-4326/aa5145. URL: https://mail-attachment.googleusercontent.com/attachment/u/1/?ui=2&

ik=21a249e14b&view=att&th=15bf7b74e219c8bf&attid=0.1&disp=inline&safe=1&zw&saddbat=ANGjdJ-sAAkkBC1zEuIUJwdVk6nAioIMuijg5RUo9kzoow1-XJ3J8dq95N_uYVGUffP9ULpViOXaXfq0JFJZqLqUZQWKSLjESaejkWlU0.

[143] R J Goldston, M L Reinke, and J A Schwartz. "A new scaling for divertor detachment". In: *Plasma Physics and Controlled Fusion* 59.5 (2017), p. 055015. ISSN: 0741-3335. DOI: 10.1088/1361-6587/aa5e6e. URL: http://stacks.iop.org/0741-3335/59/i=5/a=055015?key=crossref.40d0474e37d48d379c6f3d07665be5b6.

[144] D. E. Post et al. *Steady-state radiative cooling rates for low-density, high-temperature plasmas*. 1977. DOI: 10.1016/0092-640X(77)90026-2.

[145] David Moulton et al. "Comparison between SOLPS-4.3 and the Lengyel Model for ITER baseline neon-seeded plasmas". In: *Nuclear Fusion* (2021). ISSN: 0029-5515. DOI: 10.1088/1741-4326/abe4b2. URL: https://iopscience.iop.org/article/10.1088/1741-4326/abe4b2.

[146] A. E. Jaervinen et al. "Role of poloidal E × B drift in divertor heat transport in DIII-D". In: *Contributions to Plasma Physics* 60.5-6 (2020), e201900111. ISSN: 15213986. DOI: 10.1002/ctpp.201900111. URL: http://doi.wiley.com/10.1002/ctpp.201900111.

[147] Mike Kotschenreuther et al. "Magnetic geometry and physics of advanced divertors: The X-divertor and the snowflake". In: *Physics of Plasmas* 20.10 (2013), p. 102507. ISSN: 1070664X. DOI: 10.1063/1.4824735. URL: http://aip.scitation.org/doi/10.1063/1.4824735.

[148] B. D. Dudson et al. "The role of particle, energy and momentum losses in 1D simulations of divertor detachment". In: *Plasma Physics and Controlled Fusion* 61.6 (2019). ISSN: 13616587. DOI: 10.1088/1361-6587/ab1321. arXiv: 1812.09402. URL: https://doi.org/10.1088/1361-6587/ab1321.